

**SEARCH FOR TOPOLOGICAL SUPERCONDUCTIVITY IN
SUPERCONDUCTOR-SEMICONDUCTOR
HETEROSTRUCTURES**

by

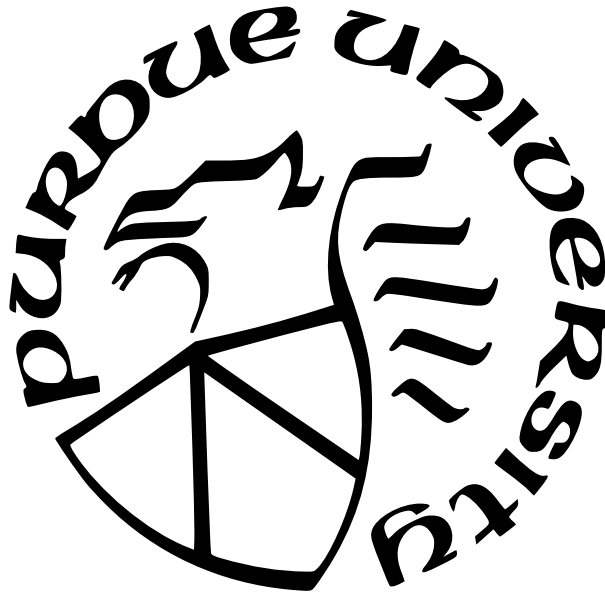
Ananthesh Sundaresh

A Dissertation

Submitted to the Faculty of Purdue University

In Partial Fulfillment of the Requirements for the degree of

Doctor of Philosophy



Department of Physics and Astronomy

West Lafayette, Indiana

August 2023

**THE PURDUE UNIVERSITY GRADUATE SCHOOL
STATEMENT OF COMMITTEE APPROVAL**

Dr. Leonid P Rokhinson, Chair
Department of Physics and Astronomy

Dr. Jukka Ilmari Vayrynen
Department of Physics and Astronomy

Dr. Sergei Savikhin
Department of Physics and Astronomy

Dr. Gabor Csathy
Department of Physics and Astronomy

Approved by:
Dr. Gabor Csathy

ACKNOWLEDGMENTS

First and foremost, I would like to extend my sincere thanks to my advisor, Professor Rokhinson. Your guidance, expertise, and unwavering support have been invaluable throughout this research journey. Your dedication to mentoring and your commitment to excellence have shaped me into the researcher I am today.

To my dedicated labmates, Zhong Wan, Ying Wang, Hao Li, and Mingi Kim, I am grateful for the collaborative environment we shared. Your unwavering support, intellectual discussions, and willingness to lend a helping hand have significantly enriched my research experience. I am indebted to the valuable insights, constructive feedback, and camaraderie we developed over the years.

I would like to acknowledge the contributions of the post-doctoral researchers in our lab, Tai Lung and Maxim. Your expertise, technical assistance, and insightful discussions have been crucial to the progress of my research. Your mentorship and willingness to share your knowledge have been immensely valuable.

My heartfelt thanks go to the members of my thesis committee for their invaluable feedback and guidance. Your expertise and constructive criticism have significantly improved the quality of this work.

I am grateful to our theoretical collaborators, Prof. Jukka and Prof Yuli Lyanda-Geller, for their invaluable insights and discussions. Your theoretical expertise and collaboration have enriched the depth and breadth of this research.

A special mention goes to Keith, the diligent building engineer, for his technical assistance and prompt resolution of various infrastructure-related matters. His tireless efforts ensured a conducive environment for conducting experiments and provided me with peace of mind during crucial moments.

I extend my heartfelt appreciation to the entire BNC and Cleanroom staff for their unwavering support and assistance throughout my research. Their commitment to maintaining state-of-the-art facilities has been indispensable in achieving the outcomes of my thesis.

No words can adequately express my gratitude to my parents and sister. Their unwavering love, endless encouragement, and belief in my abilities have been the foundation upon

which my academic pursuits were built. I am eternally grateful for their sacrifices, patience, and unwavering support during the challenging moments of this journey.

To all those mentioned above and anyone else who has contributed in any way, however small, I offer my heartfelt appreciation. Your support, guidance, and collaboration have played a significant role in the successful completion of this thesis. Thank you for being an integral part of this journey.

TABLE OF CONTENTS

LIST OF TABLES	7
LIST OF FIGURES	8
ABSTRACT	14
1 SEARCH FOR TOPOLOGICAL SUPERCONDUCTIVITY	16
1.1 Introduction to Topological Superconductivity	16
1.2 Detection scheme to search for topological boundaries	21
1.3 Planar Josephson Junctions	25
1.3.1 Current phase relation of the SQUID	27
1.3.2 Current distribution and Fraunhofer Pattern	28
1.3.3 Evolution of the Fraunhofer pattern under in-plane magnetic field	35
1.4 A note about Josephson penetration depth	42
1.5 Conclusion	43
2 STATISTICS OF SWITCHING CURRENT IN A RING	45
2.1 Introduction	45
2.2 Critical current oscillations in a superconducting ring	46
2.3 Switching current statistics in superconducting rings	50
2.4 Effect of in-plane magnetic field	51
2.4.1 Effect of gating	56
2.4.2 Effect of temperature	57
2.5 Conclusion	58
3 NON-RECIPROCAL CRITICAL CURRENT IN A NANOWIRE	60
3.1 Introduction	60
3.2 Observation of non-reciprocal critical current in a nanowire	60
3.3 Diamagnetic source of non-reciprocity	63
3.4 Dependence of non-reciprocity on various parameters	69

3.5	Geometric effects and critical current non-reciprocity in coupled superconducting wires	75
3.6	Determining total critical current in a 2 wire model	82
4	DEVICE FABRICATION AND MEASUREMENT	84
4.1	Fabrication	84
4.2	Measurement Techniques	88
4.2.1	Dilution refrigerator	88
4.2.2	Transport and Fast critical current measurements	89
4.2.3	Optimizing Noise Filtering for critical current measurements	90
4.2.4	Experimental artifacts in critical current statistics	90
5	SUMMARY AND PERSPECTIVES	93
	REFERENCES	94

LIST OF TABLES

LIST OF FIGURES

1.1	a)The spin degeneracy of the parabolic energy band is lifted by Rashbha field. b) The Zeeman field opens a gap at $k = 0$. When μ is within the gap the condition 1.19 is satisfied.	20
1.2	a) Scheme to realize a topological boundary. The condition to realize TSC is satisfied in the brown shaded region. The length and position of this region is controlled by the magnitude and direction of B . b)and c) Scheme to realize braiding of MZMs. The TSC regions controlled by B is rotated by rotating the direction of B causing an artificial brading of the MZMs at its ends.	22
1.3	A double quantum dot device is fabricated consisting of the two Al/InAs nanowires (bright yellowish region) isolated from each other by a gate. Additional side gates form a pinch off region resulting in a superconducting quantum dot(QD). One of the QDs is used to simulate an electronic charge and the other QD is used as a single electron transistor to detect the charge.	23
1.4	An eight shaped Josephson junction could be a platform to realize our braiding scheme discussed in fig1.2 The central bright regions are TiAu deposited over the Al/InAs to form central contacts. In the narrow black regions Al is selectively etched away to form Josephson junctions.	24
1.5	A SQUID device is fabricated employing two extended Josephson junction connected together to form a loop. The darker yellow regions are Al/InAs, in the dark brown region both Al and InAs is etched away resulting in an insulating layer. Two wide Josephson junctions JJS (straight) and JJC (curved) are fabricated by selectively etching only Al from two narrow regions. A layer of AlOx is deposited everywhere and a layer of TiAu is deposited on top of the two junctions forming two independent gates.	25
1.6	a)Critical current modulation of the straight junction with gate b) Critical current modulation of the curved junction with gate	26
1.7	a) Fraunhofer pattern in the straight junction.b) Fraunhofer pattern in the curved junction. c) SQUID interference pattern with a Fraunhofer envelope.	27
1.8	a) I_c measured as a function of B_z shows the squid pattern on top of a Fraunhofer pattern dominated by JJS. A $\sin x/x$ fit(red) is subtracted from the dependence and the B_z is converted to ϕ/ϕ_0 b)The current phase relation of the SQUID. A fit with $t = 0.75$ (magenta) indicates that the device is in ballistic regime.	28
1.9	Schematic of a wide Josephson junction.	28
1.10	a)Fraunhofer pattern for JJC(top) and JJC(bottom) extracted from fig 1.7b and fig 1.7a b) The extracted current distribution from a) using inverse Fourier transform.	30

1.11	Fraunhofer patterns resulting from different current distributions with linearly increasing phase difference along the junction. As the currents are concentrated more on the edges the pattern turns SQUID-like. The motion of a local spot of high current is immediately reflected in the Fraunhofer pattern.	32
1.12	Dynes futon analysis can be used to extract the current distribution in a Josephson Junction from the Fraunhofer pattern. A simulated junction with manually suppressed side lobes are shown on top. The side lobes are suppressed by 1/2 and 1/10 in the second and third plots. The extracted current from the real data is shown on the bottom. As the side lobes are suppressed more the extracted current is more concentrated towards the middle.	33
1.13	Evolution of Fraunhofer pattern with B_{\parallel} in a straight junction	34
1.14	Evolution of Fraunhofer pattern for a) JJS and b) JJC under in plane magnetic field B_{\parallel} . Fraunhofer pattern of JJS becomes asymmetric for $B_{\parallel} > 50mT$. For JJC the Fraunhofer pattern becomes asymmetric and is suppressed sooner than JJS. c)On applying B_{\perp} the entire pattern is symmetrically suppressed for JJS.	35
1.15	Current distribution extracted from fig.1.14 for a) JJS and b) JJC.	36
1.16	Relative heights of the 2^{nd} lobe, as a function of B_{\parallel} for a)JJS and b) JJC	37
1.17	Evolution of Fraunhofer pattern with B_{\perp} in a straight junction	37
1.18	Development of Fraunhofer pattern in curved junction with in-plane magnetic field of magnitude 100mT for a) $\theta = 45^{\circ}$ and b) $\theta = 135^{\circ}$. c) The extracted current distribution from a) and b).	39
1.19	Evolution of Fraunhofer pattern with B_{\parallel} in a curved junction	40
1.20	Effect of gate on critical currents for different in-plane fields for device A	41
1.21	a) Formation of Josephson vortices in a wide Josephson junction. b) Vortices can be formed in the vertical heterostructure too producing additional non-reciprocal effects which could lead to asymmetric Fraunhofer patterns.	42
2.1	AFM images of a) device A and b) device B. The yellow regions are Al/InAs, in the dark regions Al is etched away exposing InAs. A transparent layer of AlOx covers the entire device. A Ti/Au gate layer (not shown in image) is subsequently added on top.	46
2.2	switching current dynamics for a symmetric ring. The kinetic energy curves(bottom) corresponding to the vorticity n cross each other when half fluxes($\phi/\phi_0 = n + 1/2$) are inserted. The energy gap ΔE between two such curves exponentially suppresses the probability of the second meta-stable state which is reflected in the bimodal switching current distribution in fig.2.4a. The persistent currents I_p (middle) switches sign at the crossing points. Correspondingly the critical current of the ring oscillates (top) with a maxima at integer flux quantum and a minima at half fluxes (where I_p is maximum).	47

2.3	In a symmetric ring the external current is distributed equally between the two arms . For $B_z \neq 0$ the persistent current I_p adds and subtracts to the either of the arms depending on the direction of B_z and vorticity n of the ring.	49
2.4	Contour plots of histogram of switching current as function of B_z of a) device A and b)device B. The color scale indicates the counts in a logarithmic scale. Device A shows normal oscillations and bimodal histogram corresponding to the meta-stable states associated with multiple vorticity. The lower peak is exponentially suppressed as is obvious from the exponentially smaller peak value in the line cut shown in the inset. Device B shows an unusual behaviour where the bimodal distribution is not seen near the minima indicating the absence of meta-stable states which is also seen in the line cut in the inset.	50
2.5	a) Contour plot of histograms of switching currents in device A at $B_{ } = 1.9T$.b) Histogram of switching currents as a function of $B_{ }$ shows an anti-crossing at $B_{ } = 1.8T$	51
2.6	switching current distribution as function of in-plane magnetic field $B_{ }$ in a) logarithmic and b) linear scale. The distribution turns bimodal distribution of switching currents is observed for $B_{ } > 400mT$. This is not the same as the meta-stable states as the lower arm of the distribution is not exponentially suppressed.	52
2.7	Histogram of switching currents as a function of in-plane magnetic field $B_{ }$ for a) $\theta = 45^\circ$ and b) $\theta = -45^\circ$. A field misalignment of $\phi = 1.2^\circ$ effects in a small B_z component for $B_{ }$ which provides more information regarding the nature of the bi-stable states. The colors represent the counts in a logarithmic scale. The bottom plots in a) shows the I_{sw} distribution as function of B_z at fixed $B_{ }$ showing the transition between the two bi-stable states.	53
2.8	Complete set of data for the histogram of switching currents as a function of in-plane magnetic fields for different θ	54
2.9	Complete set of data for the histogram of switching currents as a function of in-plane magnetic fields for different θ with slightly misaligned magnetic field producing a B_z component.	55
2.10	Plot of extracted parameters as a function of θ for device B. The slope $\alpha = \frac{dI_{\max}}{dB_{ }}$ varies sinusoidally with angle θ with a maxima and minima at $\theta = 90^\circ$ and $\theta = 270^\circ$ where the perpendicular component B_{\perp} has the maximum magnitude. B_1 stays between $200mT$ and $400mT$ while $B_2 \approx 600mT$ only for specific values of θ .The gap between the peaks of the bimodal distribution ΔI_{jump} remains constant in magnitude switching sign around $\theta = 150^\circ$	55
2.11	a) When the direction of current is inverted, the slope of the entire curve is inverted which results from the non-reciprocity due to the diamagnetic currents in the Al-InAs multi-layer structure.	56

2.12	a) A negative gate voltage causes the switching current to increase for $B_{\parallel} < 2.35T$. b) Standard deviation as a function of gate voltage for different B_{\parallel}	57
2.13	a) The switching current follows the Bardeen relation[69] b) Standard deviation decreases and saturates below $T = 800mK$ which is a signature of quantum phase transition from a thermally activated phase slip regime to a quantum phase slip regime.	58
3.1	Non-reciprocal critical current in Al/InAs nanowires. (a) Histograms of switching currents for 10,000 positive I_{sw}^+ and negative I_{sw}^- current sweeps performed at $T = 30$ mK and $B_{\perp} = 100$ mT. Inset shows a typical current-voltage characteristic. (b) Average switching current for positive $\langle I_{sw}^+ \rangle$ and negative $\langle I_{sw}^- \rangle$ sweeps, non-reciprocal difference $\Delta I = \langle I_{sw}^+ \rangle - \langle I_{sw}^- \rangle$ and an average of all sweeps $\langle I_{sw} \rangle$ is plotted as a function of in-plane magnetic field B_{\perp} . In (c) enlarged ΔI data is colored to signify non-monotonic field dependence and multiple sign changes. (d) Dependence of ΔI on in-plane field orientation is measured at a constant $B = 100$ mT. Blue line is a fit with a sine function. Inset shows an AFM image of a $3 \mu\text{m}$ -long wire connected to wide contacts, yellow areas are Al, in darker areas Al is removed and InAs is exposed.	61
3.2	Dependence of NRC on the nanowire length and crystallographic orientation. (a) NRC is plotted for two $2 \mu\text{m}$ -long wires oriented along $[110]$ and $[1\bar{1}0]$ crystallographic axes. Insets define mutual orientataion of wires and fields. (b) NRC for 2, 3, and $5 \mu\text{m}$ wires. The top and bottom curves are shifted vertically by $0.2 \mu\text{A}$. Brackets with arrows indicate a maximum ΔB needed to insert a flux $\phi_0 = h/2e$ in the area defined by the corresponding wire lengths, as indicated by a dashed loop in the inset. An effective length for the period marked by a magenta bracket is $l = 0.5 \mu\text{m}$ for the same loop.	63
3.3	NRC in an asymmetric superconducting loop. (a) An average switching current for positive $\langle I_{sw}^+ \rangle$ and negative $\langle I_{sw}^- \rangle$ sweeps, non-reciprocal difference $\Delta I = \langle I_{sw}^+ \rangle + \langle I_{sw}^- \rangle$ and an average of all sweeps $\langle I_{sw} \rangle$ plotted as a function of out-of-plane magnetic field B_o for a loop shown in the insert in (b). Note that $\langle I_{sw} \rangle$ is maximal while $\Delta I = 0$ when the flux $\phi = n\phi_0$. In (b) ΔI for the nanowire and the loop are plotted together as a function of a reduced flux ϕ/ϕ_0 , where we used $S_{wire} = 0.0052 \mu\text{m}^2$ for the effective area in the wire and $S_{loop} = 2.59 \mu\text{m}^2$ in the loop.	65

3.4	<p>Non-reciprocity of the critical current in the presence of diamagnetic currents. Diamagnetic currents in (a) a uniform superconductor and (b) a heterostructure. (c) A two-layer heterostructure is modeled as two zero thickness wires separated by a distance d with coupling described by the Josephson energy \mathcal{E}_J. (d) Schematic of current distribution between the wires $I_i = I_{0i} - (-1)^i I_{dia}$, $i = 1, 2$, and the phase difference $\Delta\phi$ as a function of an external current $I_{ext} = I_1 + I_2$ for $B = 0$ (solid lines), $B > 0$ (dotted lines) and $B < 0$ (dashed lines). For weakly coupled wires $\mathcal{E}_J \ll \mathcal{E}_k$, the critical current is field-independent $I'_c = I_{c1} + I_{c2}$, see the text; the critical current is reduced and acquires a linear-in-B correction in a strong coupling regime $\mathcal{E}_J \gg \mathcal{E}_k$ due to the phase locking $\Delta\phi = 0$. (e) In the intermediate coupling regime $\mathcal{E}_J \sim \mathcal{E}_k$ Josephson vortices may form generating a 2π phase twist, in this case NRC becomes a non-monotonic function of B. (f) Calculated NRC ΔI is plotted as a function of flux $\Phi = S_v B_y$ for several B_x, Eq. (3.15).</p>	66
3.5	<p>Field dependence of symmetric and asymmetric parts of the switching current. (a,b) Temperature dependence of ΔI and $\langle I_{sw} \rangle$ measured as a function of B_\perp ($\theta = 90$ deg). The curves are offset by $-0.1 \mu\text{A}$ (ΔI) and 0.01 ($\langle I_{sw} \rangle$). (c,d) Angle dependence is measured by rotating magnetic field of constant magnitude $B = 100$ mT at the base temperature.</p>	69
3.6	<p>The effect of temperature on NRC. (a) The amplitude of NRC [$\Delta I(-100\text{mT}) - \Delta I(100\text{mT})$], (b) the standard deviation of the switching currents at $B_\perp = 0$, and (c) the average switching current at $B_\perp = 0$ are plotted as a function of the reduced temperature. NRC amplitude follows the T-dependence of the Cooper pair density $n_s(T)$, consistent with Eq. (3.16). $\langle I_{sw} \rangle(T)$ follows the Bardeen relation[69].</p>	70
3.7	<p>The effect of an in-plane current $B \parallel I$ on the non-reciprocal supercurrent. (a) Evolution of ΔI in the presence of B_\parallel. The plots are vertically shifted for clarity (b) The NRC amplitude falls approximately linearly with B_\parallel (c) Dependence of average switching current $\langle I_{sw} \rangle$ at $B_\perp = 0$ on B_\parallel. All data is taken at the base temperature.</p>	71
3.8	<p>NRC in other devices. (a) NRC in nanowires of different width. The plots are shifted vertically for clarity. (b) Multiple sign reversal of ΔI in another nanowire. (c) one out of ~ 20 nanowires fabricated from similar wafers showed enhanced magnitude of ΔI and reduced ΔB.</p>	72
3.9	<p>The effect of gate voltage on NRC. (a) NRC shows no observable difference on varying the gate voltage. (b) α shows very little variation with gate voltage. (c) When a negative gate voltage is applied the $\langle I_{sw} \rangle$ increases.</p>	73
3.10	<p>No NRC in a control device. A control 150 nm wide and 3 μm long nanowire is fabricated from a 20 nm thick Al film deposited on a semi-insulating Si wafer. This device shows no NRC.</p>	74
3.11	<p>(a) Field dependence of $\langle I_{sw} \rangle$ shows a Meissner state up to $B_z \approx 18$ mT. (b) No NRC is observed in an out-of- plane magnetic field.</p>	75

3.12	(a) Schematic picture of the model to explain non-reciprocity. The dark grey regions depict two superconducting wires labeled 1 and 2 (corresponding to Al and proximitized InAs wires, respectively) with the order parameter phases ϕ_1, ϕ_2 . The region between the wires denotes the insulating barrier of thickness d . In most positions x , the phases are locked to $\phi_1 = \phi_2 \pmod{2\pi}$ due to a strong Josephson coupling. In the region of length l_v spanned by the Josephson vortex the phases are not equal and as a result the phase difference winds by an additional $2\pi n$ over the vortex. The vertical arrows denote the resulting Josephson currents flowing between the two wires in the vortex. (b) Total energy vs magnetic field in the two-wire model. The dashed curves show the spectrum obtained from Eq. (3.10). The three parabolas correspond to Josephson vortices/antivortices with $n = -1, 0, 1$. The solid curves show the energies when coherent vortex tunneling (strength $E_t = 0.4$ in units of $\frac{\eta}{1+\eta} \frac{\hbar^2}{e^2 L_1 l_J}$) is included, leading to avoided crossings of states with different n	76
3.13	<i>Left:</i> The critical current non-reciprocity ΔI , Eq. (3.15), versus the flux $\Phi = B_\perp dl_v$ through the Josephson vortex. The crosses correspond to the approximation, Eq. (3.16). The applied field B_\parallel suppresses the proximity effect and therefore ΔI . In the figure $E_t = 0.4$ in units of $\frac{\eta}{1+\eta} \frac{\hbar^2}{e^2 L_1 l_J}$. <i>Right:</i> ΔI (at $B_\parallel = 0$) for different strengths E_t (in units of $\frac{\eta}{1+\eta} \frac{\hbar^2}{e^2 L_1 l_J}$) of coherent vortex tunneling that controls vortex number fluctuations; weak tunneling leads to a sawtooth-like ΔI	79
3.14	Schematic of current distribution between the wires $I_i = I_{0i} - (-1)^i I_{dia}$, $i = 1, 2$, and the phase difference $\Delta\phi$ as a function of an external current $I_{ext} = I_1 + I_2$ for (a) $\beta \leq \eta - \eta'$, (b) $\eta - \eta' < \beta < \eta + \eta'$ and (c) $\beta \geq \eta + \eta'$	82
4.1	Heterostructure and properties of wafer M and wafer J.	84
4.2	Caption	86
4.3	Arrangement of filters on the dilution refrigerator	91
4.4	Effect of different wirings and filters on the critical current in the dilution refrigerator	92
4.5	Effect of different wirings and filters on the critical current in the He3 refrigerator	92

ABSTRACT

Scientific progress often relies on unexpected discoveries and unique observations. In fact, many of the most groundbreaking scientific advances throughout history have been the result of serendipitous events. For instance, the discovery of penicillin by Alexander Fleming was a result of him noticing a mold growing on a petri dish that was contaminating his bacterial culture. Similarly, the discovery of the cosmic microwave background radiation, which is considered one of the strongest pieces of evidence for the Big Bang theory, was the result of two scientists accidentally stumbling upon it while conducting a completely different experiment. These types of unexpected discoveries can lead to new avenues of research and open up entirely new fields of study. During my PhD, I experienced a similar phenomenon when I stumbled upon an anomaly in my experimental data that led me down a completely new path of investigation. This unexpected discovery not only provided me with new insights into the underlying mechanisms of my research, but also opened new avenues for future research directions. It was a reminder that sometimes the greatest scientific progress can come from the most unexpected places.

My primary focus was initially directed towards topological superconductivity. However, this research direction was modified by unexpected findings while characterizing a SQUID. Specifically, a unique response by a Josephson junction was observed when exposed to an in-plane magnetic field. Chapter 1 details our experimental results on the SQUID. We observed intriguing effects resulting from the in-plane magnetic field in the asymmetric evolution of the Fraunhofer pattern suggesting the existence of additional underlying physics in the heterostructure, which may have been previously overlooked. This serendipitous finding served as the impetus to explore simpler superconducting devices such as nanowires and rings. Remarkably, subsequent investigations into the critical current of a superconducting ring revealed a bi-modal histogram arising from the application of an in-plane magnetic field, which was an unforeseen outcome. This adds to our observations made in chapter 1. Chapter 2 details the unique properties of Al-InAs superconducting rings. Further experiments involving a superconducting nanowire resulted in the observation of non-reciprocal critical current under an in-plane magnetic field perpendicular to the current direction, subsequently referred

to as the superconducting diode effect. Chapter 3 delves into the non-reciprocal properties of an Al-InAs superconducting nanowire. Our findings revealed the diamagnetic source of non-reciprocity generic to multi-layer superconductors. Finally, chapter 4 provides a detailed account of the fabrication processes for the superconducting devices, along with a discussion of the measurement techniques employed to unveil the underlying physics.

1. SEARCH FOR TOPOLOGICAL SUPERCONDUCTIVITY

1.1 Introduction to Topological Superconductivity

Topology is a branch of mathematics that studies the properties of space that are preserved under continuous deformations, such as stretching, bending, twisting, and folding, but not tearing or gluing. It focuses on understanding the fundamental characteristics of spaces and the relationships between their various elements. In the realm of physics, topology manifests itself through the energy spectrum of materials. In quantum mechanics any two wave functions that can be smoothly connected without interruption are considered to be topologically identical. To classify systems based on their topology, a calculation is performed to determine an integer value known as a topological invariant, such as the Chern number[1].

The physics becomes even more intriguing when combining topology with superconductivity to obtain what is known as a topological superconductor (TSC). In the simplest case, consider a 1D p-wave superconductor with broken time reversal symmetry. The Hamiltonian takes the form

$$\mathcal{H} = \sum \Psi_p^\dagger H_{BdG}(p, \Delta) \Psi_p \quad (1.1)$$

with

$$\Psi_p = (c_p, c_{-p}^\dagger) \quad (1.2)$$

and

$$H_{BdG} = \frac{1}{2} \begin{pmatrix} \epsilon(p) & \Delta_p \\ \Delta_p^* & -\epsilon(p) \end{pmatrix} \quad (1.3)$$

The energy is given by,

$$H_{BdG}^2 = \epsilon^2(p) + |\Delta_p|^2 \quad (1.4)$$

$$E_{\pm} = \pm \sqrt{\epsilon^2(p) + |\Delta|^2 p^2}, \quad (1.5)$$

where $\epsilon(p) = \frac{p^2}{2m} - \mu$. When $\mu < 0$ the spectrum is always gapped (E_+ and E_- bands do not cross) even when $\Delta = 0$. Hence it is topologically equivalent to a band insulator.

However, when μ is positive the gap is non-zero for $\Delta > 0$ and becomes zero when $\Delta = 0$. The superconducting state is topologically distinct from the the trivial bulk insulator. A topological phase transition is associated here with a change of μ across zero. The same dispersion relation can be defined for a 1D Kitaev chain[2] described by the Hamiltonian,

$$\mathcal{H} = \sum_j -t(c_j^\dagger c_{j+1} + c_{j+1}^\dagger c_j) - \mu c_j^\dagger c_j + |\Delta| (c_{j+1}^\dagger c_j^\dagger + c_j c_{j+1}) \quad (1.6)$$

where j represents the lattice sites and t represents the hopping energy. The resulting dispersion relation has the form,

$$E_\pm = \pm \sqrt{(2t \cos p + \mu)^2 + 4 |\Delta|^2 \sin^2 p} \quad (1.7)$$

Now, define

$$\gamma_{2j-1} = c_j^\dagger + c_j, \quad (1.8)$$

$$\gamma_{2j} = i(c_j^\dagger - c_j) \quad (1.9)$$

This implies

$$c_j = \frac{1}{2}(\gamma_{2j-1} + i\gamma_{2j}), \quad (1.10)$$

$$\gamma_j = \gamma_j^\dagger \quad (1.11)$$

with $\gamma_i, \gamma_j = 2\delta_{ij}$. The γ is thus a Majorana operator. We can rewrite the Hamiltonian as

$$\mathcal{H} = \frac{i}{2} \sum -\mu \gamma_{2j-1} \gamma_{2j} + (t + |\Delta|) \gamma_{2j} \gamma_{2j+1} + (-t + |\Delta|) \gamma_{2j-1} \gamma_{2j+2} \quad (1.12)$$

Here when $\mu < 0$ and $|\Delta| = t = 0$ the Hamiltonian takes the form,

$$\mathcal{H} = \frac{-i\mu}{2} \sum_j \gamma_{2j-1} \gamma_{2j} \quad (1.13)$$

This represents a chain with no Majoranas left unpaired which is a trivial phase. Now consider a particular case where $\mu = 0$ and $|\Delta| = t > 0$ resulting in a Hamiltonian,

$$\mathcal{H} = it \sum_j \gamma_{2j} \gamma_{2j+1} \quad (1.14)$$

Suddenly, we note that the last and first Majoranas are unpaired resulting in a topologically non-trivial phase. These unpaired Majoranas will remain unpaired unless the gap closes and reopens : they are *topologically protected* from local perturbations. Similar results can be extended to 2D case[3] where the edge modes of the 2D p-wave superconductors can support chiral Majoranas.

The hot pursuit for Majorana zero modes (MZM) are due to its huge potential to be used in fault tolerant quantum computation[4]–[6]. The presence of well-separated MZMs exhibit non-Abelian braiding statistics representing a non-commutative operation which makes them suitable for implementing unitary gate operations, which are essential for achieving fault-tolerant quantum computation.

The quest for realizing MZMs has resulted in a wide array of theoretical proposals across various systems. Numerous proposals have been put forward, encompassing a range of physical systems such as fractional quantum Hall states[7]–[10], spinless chiral p-wave superconductors[2], [3], [11]–[13], topological insulator-superconductor hybrids[14]–[16], non-centrosymmetric superconductors[17], helical magnets[18], carbon nanotubes[19], spin-orbit coupled ferromagnetic Josephson junctions[20], and many others. Several comprehensive reviews[21]–[25] delve into the plethora of theoretical proposals exploring MZMs, providing valuable insights and analysis on this subject.

Addressing the challenge of scalability is a crucial aspect of practical adoption for these proposals. Among the various approaches, the realization of a hybrid superconductor-semiconductor heterostructure[26]–[29] has emerged as one of the most promising avenues. The combination of well-studied s-wave superconductivity with the tunability and scalability of semiconductor technologies holds significant potential for large-scale implementations of Majorana zero mode (MZM)-based quantum computing. A $p + ip$ superconductor is engi-

neered by combining conventional s-wave superconductivity, a semiconductor quantum well with high spin-orbit strength and a ferromagnetic[28], [29],

$$H_{eff} = H_{QW} + H_{\Delta} + H_z, \quad (1.15)$$

$$H_{QW} = \int dx \Psi^\dagger \left(-\frac{\partial_x^2}{2m} - \mu - i\alpha\sigma^y\partial_x + h\sigma^z \right) \Psi, \quad (1.16)$$

$$H_{\Delta} = \int d^2\mathbf{r} \Delta (\Psi_\uparrow\Psi_\downarrow + H.c), \quad (1.17)$$

$$H_z = \int d^2\mathbf{r} \Psi^\dagger \sigma^z \Psi \quad (1.18)$$

Here α represents strength of the Rashba spin-orbit interactions[30]. The Zeeman term H_z breaks the time reversal symmetry. Alternatively the Zeeman term which comes from the ferromagnet can be replaced by a term arising from an external magnetic field. This is enabled by growing a (110) quantum well with both Rashbha and Dresselhaus terms[26] and applying an external magnetic field aligned perpendicular to the Rashbha field. The Rashbha coupling lifts the spin-degeneracy of the parabolic energy band and the Zeeman term opens a gap as illustrated in fig1.1. When the chemical potential μ is within this gap the condition for the topological superconductivity is satisfied,

$$E_z > \sqrt{\Delta^2 + \mu^2} \quad (1.19)$$

where $E_z = g\mu_B B$, Δ is the superconducting gap and μ is the chemical potential.

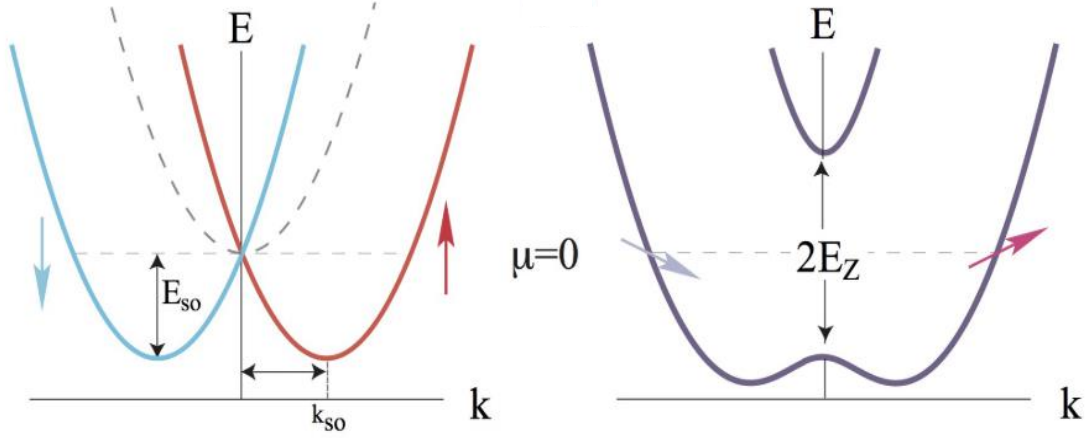


Figure 1.1. a) The spin degeneracy of the parabolic energy band is lifted by Rashba field. b) The Zeeman field opens a gap at $k = 0$. When μ is within the gap the condition 1.19 is satisfied.

Once all the necessary conditions are met for the realization of a TSC, the next obvious step is to verify its existence and distinguish them from mundane subgap excitations like trivial Andreev levels. One of the most fundamental signatures to look for is the phase signature associated with the presence of MZMs. In a superconductor-normal metal-superconductor (SNS) Josephson junction, the presence of MZM turns the junction into 4π periodic as opposed to 2π periodic in the trivial case. The Josephson current $I_j \propto \sin \phi$ evolves into $I_j \propto \sin \phi/2$ [31]. Also known as fractional AC Josephson effect, this can also be observed as doubling of heights of Shapiro[32] steps under irradiation of radio-frequency waves. Another method is to look for the tunnelling properties of the MZMs. The presence of an MZM should show up as a zero bias peak[33]–[35] quantized to $G = 2e^2/h$ in the tunnelling spectra as the emergence of MZMs gives rise to resonant Andreev reflection. Signatures of TSC can also be seen in Coulomb blockade experiments in quantum dots[36]–[38]. But here the Γ s are closer and overlaps significantly causing a deviation from zero energy. The idea stems from the fact that in a superconducting even-odd Coulomb blockade effect the conductance is $2e$ -periodic. The presence of MZM makes this $1e$ -periodic and hence can be seen in the spacing of the Coulomb blockade peaks although in a quantum dot the MZM pairs are closer and their overlap causes the energy to deviate from zero. These signatures are considered necessary but not sufficient and hence cannot be used as fail-proof way to confirm MZMs

since these can have alternate explanations like disorder induced trivial subgap states, Kondo effect, Yu-Shiba-Rusinov (YSR) states etc. Thus far, no single experiment has successfully marked all the check-boxes required to establish an observation as a truly significant signature of Majorana zero modes (MZMs). In short, although lot of promising signatures of TSC have been seen, we are still far from getting a conclusive evidence of non-Abelian modes.

1.2 Detection scheme to search for topological boundaries

Our efforts in the search for TSC is based on the hybrid Al/InAs heterostructure platform[39]. Narrow band-gap semiconductors like InAs and InSb are suitable options[26] as a material platform to realize TSC due to its large g factors and strong spin orbit coupling. The growth and fabrication of Al-InAs heterostructure has been well established. InAs is very popular because the Fermi level at the InAs surface is pinned inside the conduction band. This leads to the absence of Schottky barriers which helps in making high quality ohmic and superconducting contacts to InAs relatively easy. Proximity effect in InAs was demonstrated as early as 1985 in a Nb-InAs-Nb Josephson junction[40]. The demonstration of a hard superconducting gap[39], [41], the observation of zero bias peaks in the conductance spectrum of Al-InAs nanowire in tunnelling regime[42], [43] and observation of other signatures of a topological phase[44]–[48] has proved the system to be very promising.

A boundary between a topologically trivial and non-trivial region can be created exploiting the condition 1.19 in primarily 2 ways : varying μ or varying E_z . The former is usually achieved by using gating or by varying material parameters at the boundary. The latter can be achieved by varying the magnetic field locally. Specifically, $E_z = g\mu_B B |\sin \phi - \theta|$ where ϕ and θ are polar angles of the momentum k and magnetic field B respectively. Thus Zeeman term can be varied by modulating $\phi - \theta$. This can be achieved as shown in fig. 1.2. A curved p-wave superconducting nanowire is subjected to an in-plane magnetic field. The magnitude of $\phi - \theta$ varies along the wire and the condition for topological superconductivity is satisfied only in a section of the wire creating two boundaries between a topologically trivial and non-trivial regions. The position of the boundary is controlled by the magnitude and direction of B .

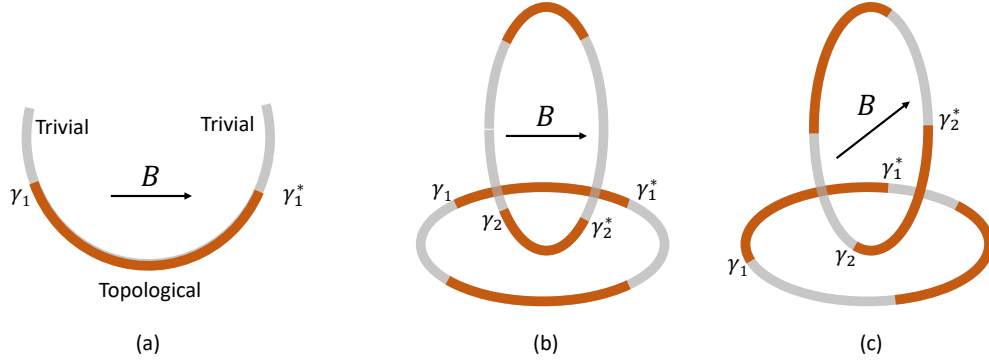


Figure 1.2. a) Scheme to realize a topological boundary. The condition to realize TSC is satisfied in the brown shaded region. The length and position of this region is controlled by the magnitude and direction of B . b) and c) Scheme to realize braiding of MZMs. The TSC regions controlled by B is rotated by rotating the direction of B causing an artificial braiding of the MZMs at its ends.

One of the ways to detect such a boundary is a charge sensor. A pair of Majoranas is characterized by a charge which can be measured using a charge sensor conveniently placed close to the boundary. The charge detector should reflect a change of its state when it detects a charge associated with the formation topological non-trivial region or its motion near it. Fig 1.3 illustrates such a quantum dot charge sensor fabricated from an Al/InAs heterostructure. The bottom Al/InAs nanowire is separated from the top gates by a 25 nm thick AlOx dielectric. The set of two quantum dots next to each other is intended to be used as a single electron transistor-charge sensor pair to simulate the formation and test the detection of charge. But the device performance did not meet the required sensitivity for such a measurement as gaps of the pinch off gates were larger than required for the operation of the device under the depletion regime. Further experimentation is required to develop the device and is reserved for later.

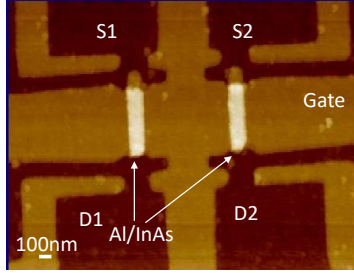


Figure 1.3. A double quantum dot device is fabricated consisting of the two Al/InAs nanowires (bright yellowish region) isolated from each other by a gate. Additional side gates form a pinch off region resulting in a superconducting quantum dot(QD). One of the QDs is used to simulate an electronic charge and the other QD is used as a single electron transistor to detect the charge.

One of the unique properties of Majoranas are their braiding statistics which serves as the ultimate proof of their existence. Braiding a pair of particles in simple terms entails swapping their positions. Swapping the positions of two indistinguishable particles produces no measurable change. But braiding of non-Abelian particles transforms system into a new quantum state. In the time axis the braiding leaves a unique traceable 'strand' distinguishing non-Abelian particles from Abelian particles. Fig. 1.2b and c illustrates the scheme to braid MZMs. As indicated before the direction of B can be used to control the position of MZMs along a curved nanowire. Extending this idea into intertwined loops of nanowires may enable the exchange of MZMs around each other by rotating B .

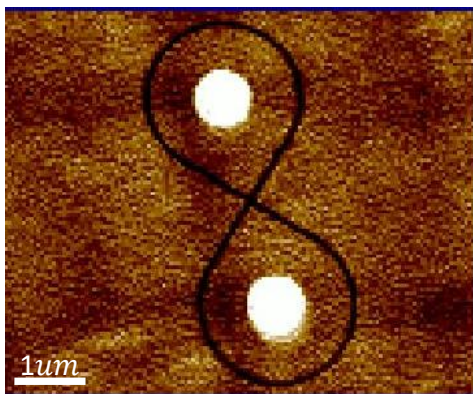


Figure 1.4. An eight shaped Josephson junction could be a platform to realize our braiding scheme discussed in fig1.2 The central bright regions are TiAu deposited over the Al/InAs to form central contacts. In the narrow black regions Al is selectively etched away to form Josephson junctions.

Practically, such an idea could be implemented using either nanowires or Josephson junctions shaped as figure-8. A preliminary attempt to test the feasibility of such a device by fabricating a figure-8-shaped Josephson Junction device as shown in fig 1.4. But we realized that it was substantially challenging to make the central contact with sizes of the order of 100nm without shorting the contacts and the gates. In this device the Al etching to define the Josephson junctions were made first. Then a 20nm HfOx dielectric was grown to be used as a gate dielectric. After depositing the gate electrodes another 15nm layer of HfOx was grown. A small hole of 100-200nm diameter was defined using e-beam lithography and was attempted to etch using ion-milling. We realized that on test devices with progressively smaller hole diameters, no contact to the center contact could be made for holes smaller than 500nm. This is due to re-deposition of etched oxide and PMMA into the holes. Considering the fabrication challenges we decided to focus on the study of curved Josephson junction in order to understand whether we can detect and manipulate a boundary between topologically trivial and non-trivial regions using electron transport measurements.

1.3 Planar Josephson Junctions

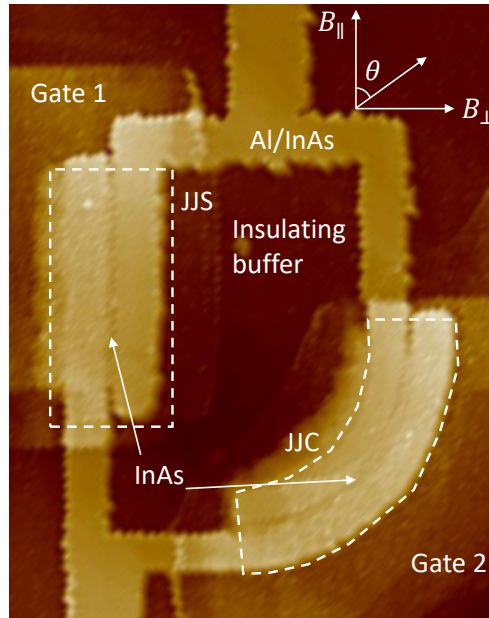


Figure 1.5. A SQUID device is fabricated employing two extended Josephson junction connected together to form a loop. The darker yellow regions are Al/InAs, in the dark brown region both Al and InAs is etched away resulting in an insulating layer. Two wide Josephson junctions JJS (straight) and JJC (curved) are fabricated by selectively etching only Al from two narrow regions. A layer of AlOx is deposited everywhere and a layer of TiAu is deposited on top of the two junctions forming two independent gates.

Wide planar Josephson junctions fabricated from super-semiconductor heterostructures have emerged as highly promising platforms for the realization of topological superconductivity [49], [50]. By subjecting these junctions to an in-plane magnetic field, the quasi-one-dimensional region defining the junction exhibits the potential to host Majorana zero modes (MZMs) at its ends. The system is predicted to undergo a topological phase transition by varying the magnetic field or chemical potential, resulting in the formation of a topological boundary at the extremities of the extended junction. Encouraging experimental signatures of such phase transitions have been reported [44]–[46], [48]. In our experimental study, we investigate the feasibility of inwardly shifting the boundary by introducing a bend to the Josephson junction, as depicted in Figure 1.2. We anticipate that the presence of MZMs

will manifest through distinct variations in the critical current profile (Fraunhofer pattern) of the junction under in-plane magnetic fields [51].

A Superconducting Quantum Interference Device (SQUID) is fabricated with two Josephson junctions: a straight planar Josephson junction (JJS) and a curved planar Josephson junction (JJC). The junctions' conductance can be individually controlled by two electrostatic gates fabricated on top of each junction. Application of an out-of-plane magnetic field enables phase control across the junctions. Figure 1.5 depicts an atomic force microscopy (AFM) image of the device along with the orientations of the magnetic field.

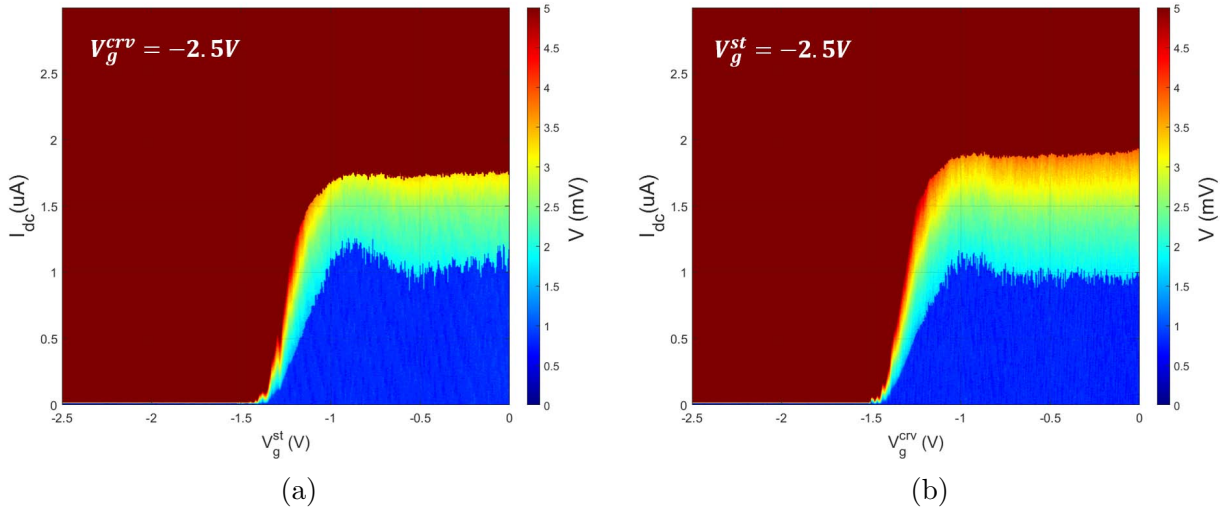


Figure 1.6. a) Critical current modulation of the straight junction with gate
b) Critical current modulation of the curved junction with gate

The individual gate dependence of the junctions at zero magnetic field are shown in fig 1.6. The DC voltage V_{DC} across the junction is plotted (color) as a function of bias current, I_{DC} and gate voltage V_g^{crv} and V_g^{st} . Each of the junction is calibrated when the other junction is kept under a gate voltage of $V_g = -2.5 V$, which is sufficient to ensure complete isolation. We find that the $I_c - V_g$ characteristics of both junctions are almost identical at $B = 0$.

Figures 1.7a and 1.7b illustrate the Fraunhofer interference phenomenon in JJS and JJC, respectively. The periods $\Delta B_{JJS} = 2mT$ and $\Delta B_{JJC} = 1.8mT$ correspond to effective junction areas of $1.03\mu m^2$ and $1.15\mu m^2$ for JJS and JJC, respectively. This implies that the effective penetration depth is approximately $\lambda_{JJS} \approx 170nm$ and $\lambda_{JJC} \approx 130nm$ which is

very close to similar experiments reports elsewhere[44], [47]. When both junctions are active ($V_g^{crv} = V_g^{st} = 0$), we observe SQUID oscillations with a period of 0.2mT, enveloped by the Fraunhofer interference pattern, as depicted in Figure 1.7c. This corresponds to an effective area of $A = 10.3\mu m^2$.

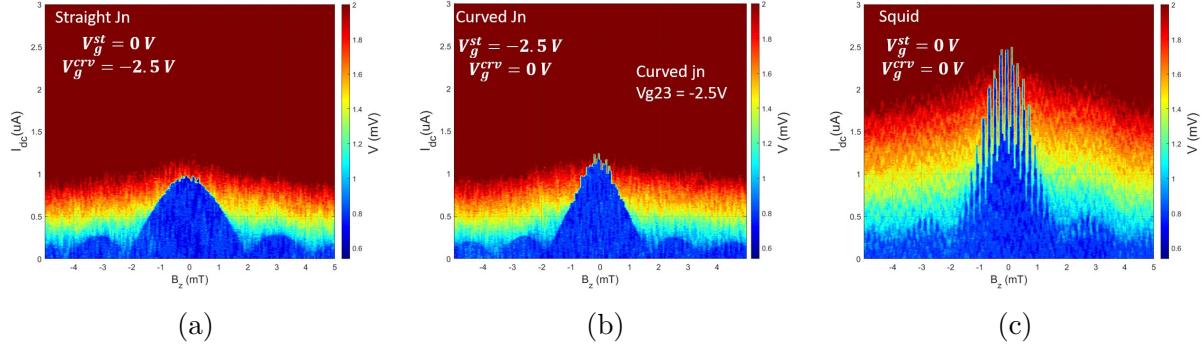


Figure 1.7. a) Fraunhofer pattern in the straight junction. b) Fraunhofer pattern in the curved junction. c) SQUID interference pattern with a Fraunhofer envelope.

The extracted $I_c R_N = 0.056$ mV product is found to be almost 10 times smaller than the maximum theoretical value $I_c R_N = \pi\Delta/e = 0.68$ mV, for a short ballistic junction Golubov. where we use experimentally measured critical temperature of Al $T_c = 1.5$ K.

1.3.1 Current phase relation of the SQUID

In an asymmetric SQUID with critical current in junctions 1 and 2 $I_{c1} \gg I_{c2}$, the phase difference across the junction 2 is approximately $\pi/2$ and the total critical current $I_c = I_{c1} + I_{c2}(\phi + \pi/2)$ where ϕ is the phase difference. For a junction with arbitrary junction transparency t , the current phase relation can be written as[52],

$$I_c = I_{c,0} \sin(\phi) / \sqrt{1 - t \sin^2(\phi/2)} \quad (1.20)$$

In order to extract the CPR a gate voltage of $V_{g, str} = 0, V_{g, crv} = -1.3$ V is applied at $T = 20$ mK resulting in $I_c^{st} \approx 3.5 I_c^{crv}$. The I_c as a function of B_z is measured as shown in fig. 1.8a. A Fraunhofer envelope is extracted by fitting a $\sin(x)/x$ function to the minima

points of the oscillations and subtracted from the curve. Data for $-0.2mT < B_z < 0.2mT$ is then used to fit eq.1.20. B_z is converted to ϕ/ϕ_0 assuming an area of $9\mu m^2$. We observe a good fit with $t = 0.75$ (magenta). Also plotted is the simulated CPR for $t = 0$ (diffusive regime) and $t = 1$ (ballistic regime). This shows that our device performs close the ballistic regime as expected since the mean free path $l_e = 300nm$ is larger than the junction length of $120nm$.

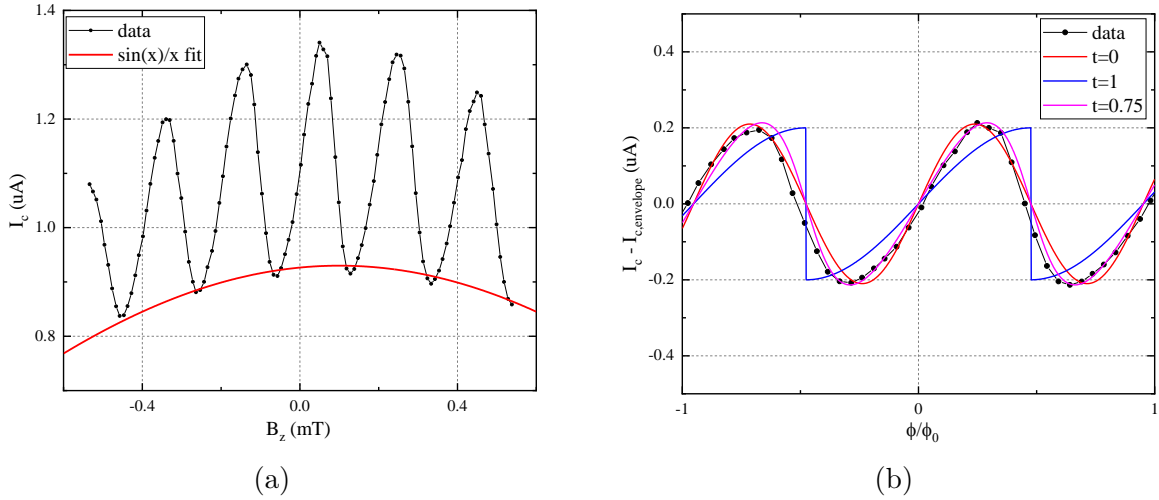


Figure 1.8. a) I_c measured as a function of B_z shows the squid pattern on top of a Fraunhofer pattern dominated by JJS. A $\sin x/x$ fit (red) is subtracted from the dependence and the B_z is converted to ϕ/ϕ_0 b) The current phase relation of the SQUID. A fit with $t = 0.75$ (magenta) indicates that the device is in ballistic regime.

1.3.2 Current distribution and Fraunhofer Pattern

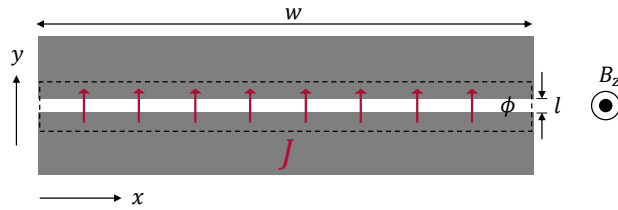


Figure 1.9. Schematic of a wide Josephson junction.

Consider a wide Josephson junction of width w and length l as shown in fig. 1.9. At any point x along the junction the local value of the Josephson current density is given by

$$J_s = J_c(x) \sin(\gamma(x)), \quad (1.21)$$

where $\gamma(x)$ is the phase difference across the junction at a position x . The total current is

$$I_s = \int J_c(x) \sin(\gamma(x)) dx \quad (1.22)$$

Both J_c and γ are, in general, can depend on the external magnetic field and be position-dependent. In the simplest case it is usually assumed that $J_c(x)$ is position-independent, $J_c(x) = J_c$, and $\gamma(x)$ varies linearly with x

$$\gamma(x) = \gamma_0 + \frac{2\pi Bl}{\phi_0} x, \quad (1.23)$$

in this case

$$I_s = I_c \left| \frac{\sin(\pi\phi/\phi_0)}{\pi\phi/\phi_0} \right| \quad (1.24)$$

This equation approximately describes measured variation of critical current in our Josephson junctions as shown in fig 1.10a, however the subtle physics is hidden in deviations from the ideal case, for example non-uniform and x -dependent $J(x)$. The measured Fraunhofer pattern for JJC is slightly tapered towards $B_z = 0$ compared to JJS and in both cases the nodes of the pattern do not reach zero.

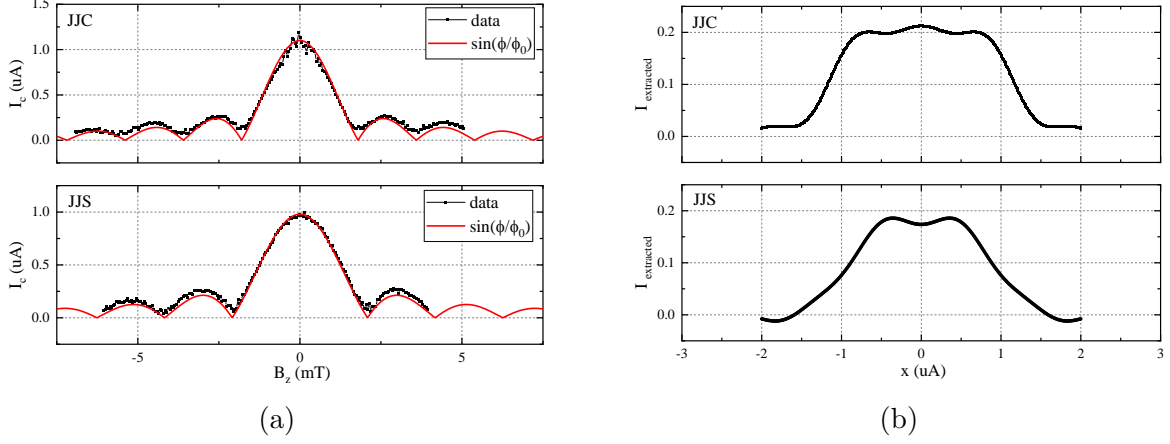


Figure 1.10. a) Fraunhofer pattern for JJC (top) and JJS (bottom) extracted from fig 1.7b and fig 1.7a b) The extracted current distribution from a) using inverse Fourier transform.

The rationale to study Fraunhofer pattern was to look for hidden signatures of MZMs and their motion in the Josephson junction. At a boundary of a topologically trivial and non-trivial phases, where MZM resides, superconducting gap closes opening an extra channel for current flow. Thus, we expected modification of $J(x)$ when the boundary is formed. A non-uniform current distribution will modify $I_s(B)$ dependence, fig. 1.11 shows $I_s(B)$ for some current distributions assuming a linear $\gamma(x)$. For example when the entire current is concentrated more on the edges the Fraunhofer pattern evolves into a SQUID like pattern, $I_c \propto \sin \pi\phi/\phi_0$. In an extreme case where there are two local spots where the current is substantially higher than the rest both the period and height of subsequent lobes become non-uniform. Eventually, when the spots fuse to one the pattern differs substantially from a usual Fraunhofer pattern.

Inversely, current distribution inside the junction can be recovered from the measured $I_s(B)$ using inverse Fourier transform on the Fraunhofer pattern. The extracted current distribution from the Fraunhofer pattern for our Josephson junctions are shown in fig. 1.10b. We note that the current distribution extracted for JJS and JJC looks different. For JJC the current is more uniform along the width of the junction, while for the JJS the current is concentrated towards the centre. We note here that the accuracy of the current extraction process is not high due to a limited number of lobes observed in the Fraunhofer pattern.

The alternate lobes of the Fraunhofer needs to be inverted before doing an inverse Fourier transform. This becomes difficult when the nodes do not reach zero as noted earlier. Hence this process can only be used to get a qualitative picture of the real distribution. Extracted current distribution of some special cases of Fraunhofer patterns is shown in appendix fig [1.12](#).

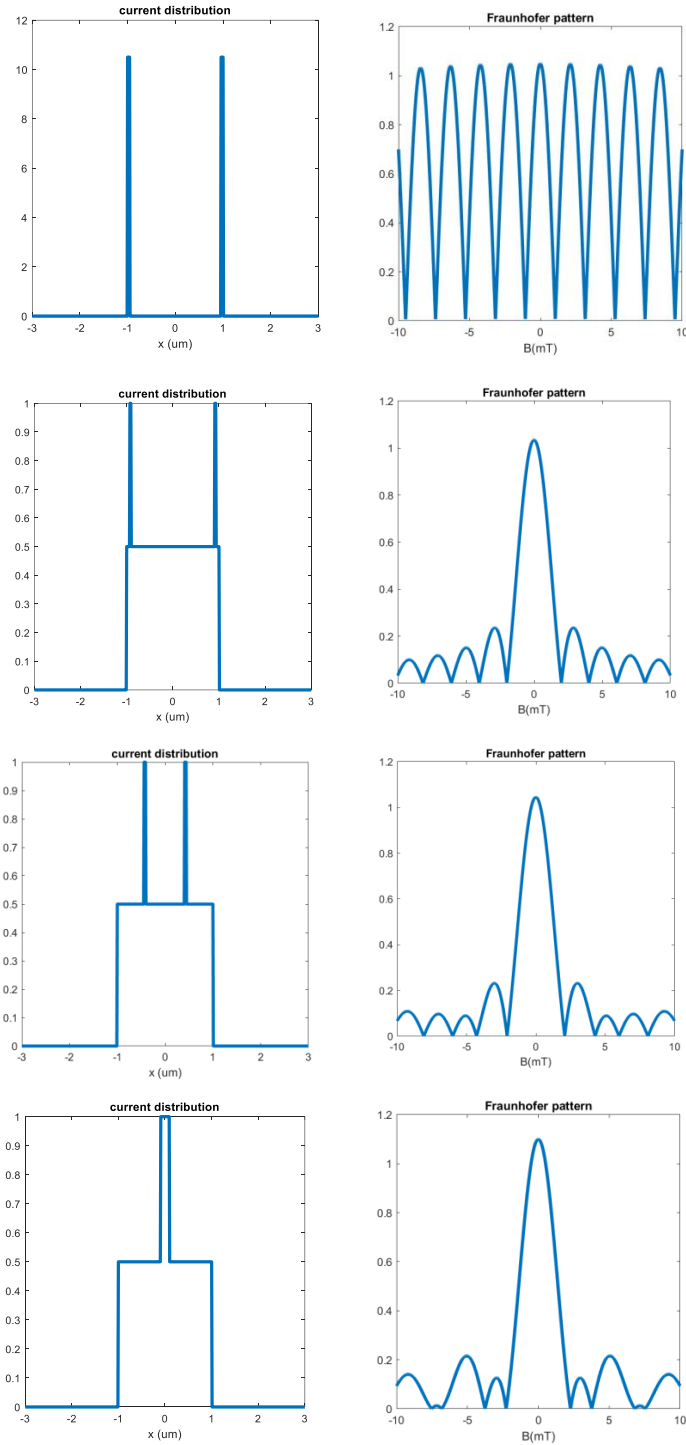


Figure 1.11. Fraunhofer patterns resulting from different current distributions with linearly increasing phase difference along the junction. As the currents are concentrated more on the edges the pattern turns SQUID-like. The motion of a local spot of high current is immediately reflected in the Fraunhofer pattern.

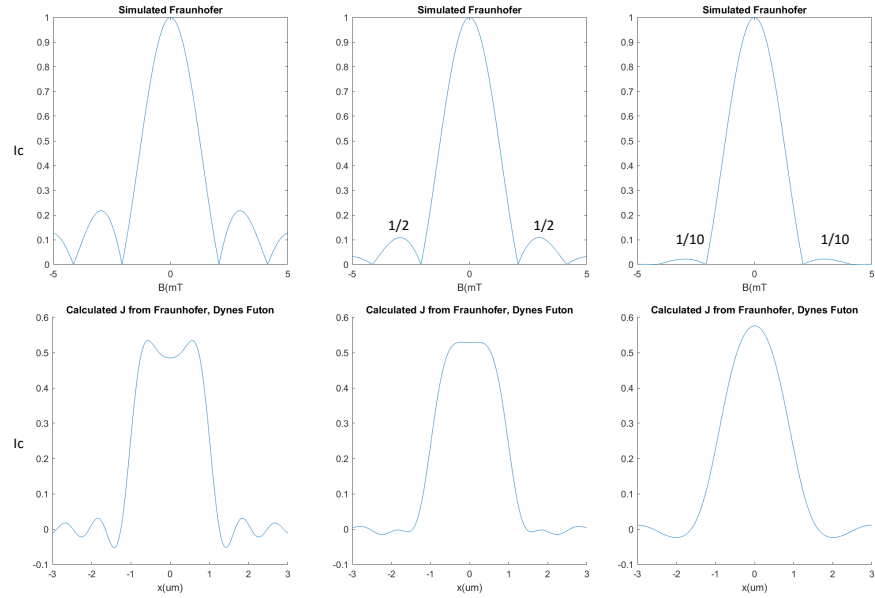


Figure 1.12. Dynes futon analysis can be used to extract the current distribution in a Josephson Junction from the Fraunhofer pattern. A simulated junction with manually suppressed side lobes are shown on top. The side lobes are suppressed by $1/2$ and $1/10$ in the second and third plots. The extracted current from the real data is shown on the bottom. As the side lobes are suppressed more the extracted current is more concentrated towards the middle.

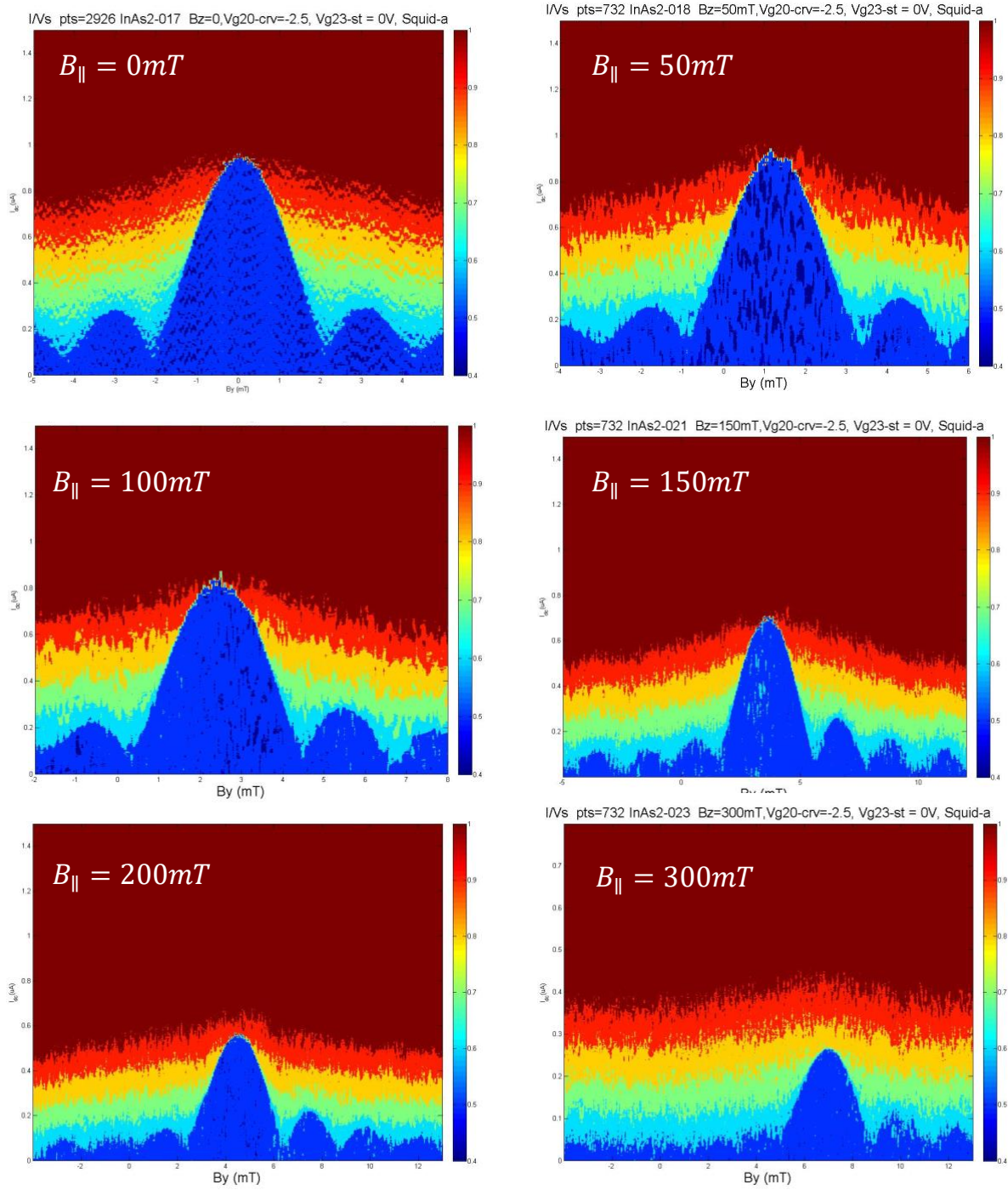


Figure 1.13. Evolution of Fraunhofer pattern with B_{\parallel} in a straight junction

1.3.3 Evolution of the Fraunhofer pattern under in-plane magnetic field

The critical in-plane magnetic fields for our junctions are approximately $B_{\parallel}^c \approx 400mT$ and $B_{\perp}^c \approx 350mT$ for magnetic fields aligned parallel and perpendicular to the junction, respectively. The lower value for B_{\perp}^c is attributed to the effect of flux focusing. In this phenomenon, magnetic field lines bend into the junction area around the edges of the superconducting Al leads resulting in non-zero B_z component. We have observed that flux focusing becomes a significant challenge in device design when dealing with curved geometries. The presence of $B_z(x)$ field component alters $J(x)$ distribution, making it challenging to establish a clear boundary between topologically trivial and non-trivial regions. Furthermore, this non-uniformity in magnetic fields can also be present in straight junctions with non-uniform edges[43].

We note here that similar device with only straight junctions was reported to have signatures of gap closing and reopening under certain magnetic fields and gate voltages[46], [47]. We do not see such a signature in our system, which can partly be attributed to the low transparency of the junctions.

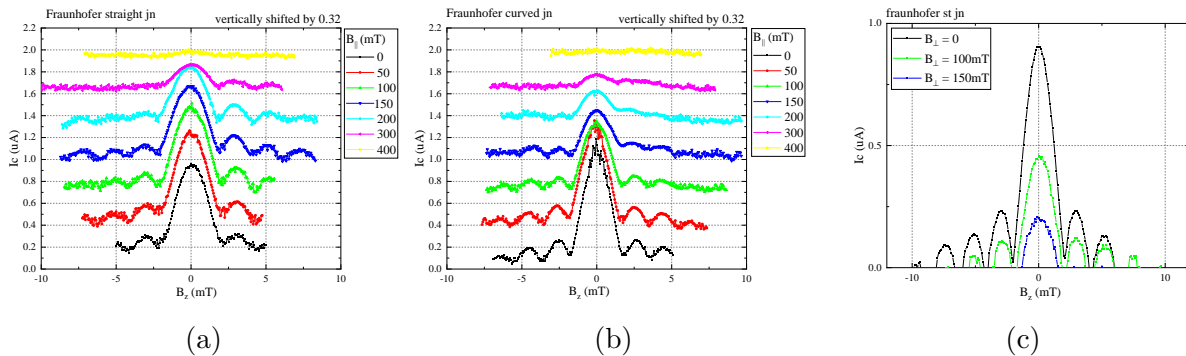


Figure 1.14. Evolution of Fraunhofer pattern for a) JJS and b) JJC under in plane magnetic field B_{\parallel} . Fraunhofer pattern of JJS becomes asymmetric for $B_{\parallel} > 50mT$. For JJC the Fraunhofer pattern becomes asymmetric and is suppressed sooner than JJS. c) On applying B_{\perp} the entire pattern is symmetrically suppressed for JJS.

The evolution of the Fraunhofer interference pattern as a response to in-plane magnetic field B_{\parallel} is shown in Fig 1.14. We observe that for JJS the Fraunhofer pattern becomes

asymmetric for $B_{\parallel} \geq 100mT$ eventually disappearing at $B_{\parallel} = 400mT$. For JJC, again, the pattern becomes asymmetric for $B_{\parallel} \geq 100mT$, but also suppressed much faster. When B_{\perp} is applied on JJS the pattern is symmetrically suppressed much faster. The plots here are extracted from the contour plots of I-V curves in fig.1.13 and 1.17.

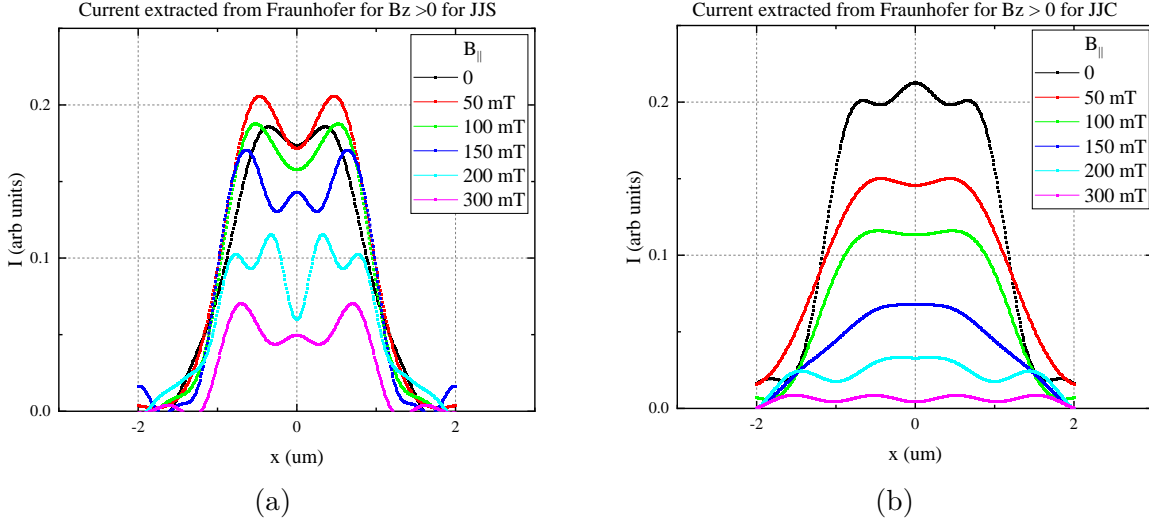


Figure 1.15. Current distribution extracted from fig.1.14 for a) JJS and b) JJC.

Fig. 1.15 displays the extracted current distribution from fig.1.14 where only the $B_z > 0$ half of the Fraunhofer pattern is used to extract the current. We find that for JJS, as B_{\parallel} is increased the current is slightly concentrated more towards the edges along with a decrease in overall magnitude, whereas in JJC we do not observe such a behaviour. The current is uniformly distributed along the junction for all values of B_{\parallel} . A qualitative understanding can also be formed from the evolution of the relative heights of the lobe as shown in fig.1.16. We observe that the relative lobe height for the 2nd lobe increases for $B_z > 0$ for both JJS and JJC. But for $B_z < 0$ the relative lobe heights decreases for JJS while it still increases for JJC. An increase in relative 2nd lobe height can be associated with a SQUID-like behaviour of a Josephson junction with currents concentrated near the edges. Such behavior has been reported in straight junctions before [43]. And the opposite can be inferred as a concentration of current towards the centre.

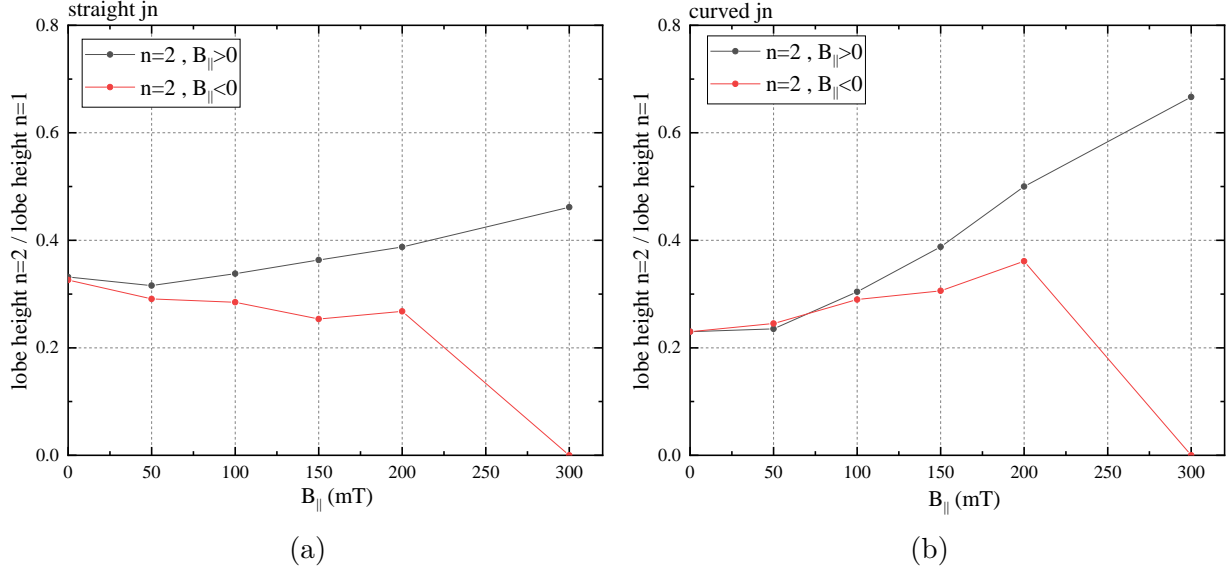


Figure 1.16. Relative heights of the 2nd lobe, as a function of B_{\parallel} for a) JJS and b) JJC

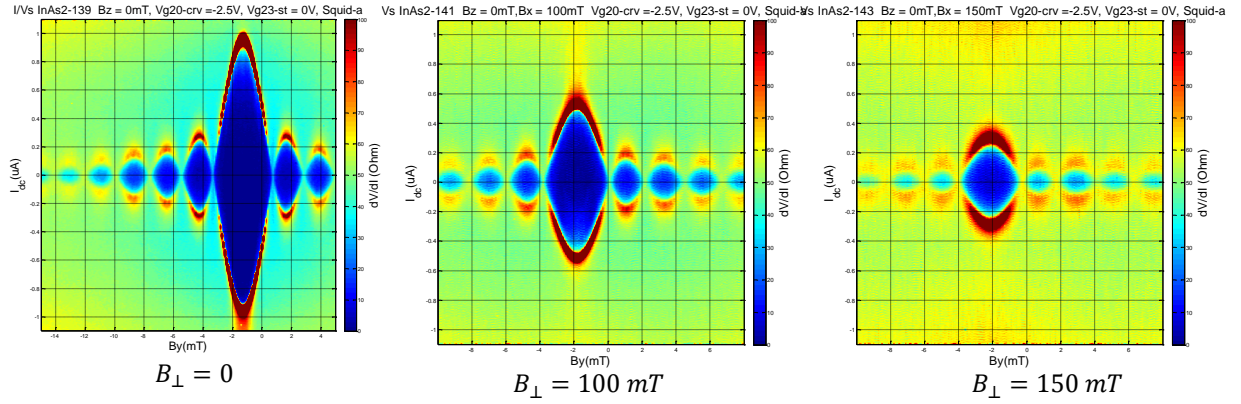


Figure 1.17. Evolution of Fraunhofer pattern with B_{\perp} in a straight junction

Looking closely at the available data, we realize that the asymmetry is present primarily in the lobe heights. The central lobe and the other lobes are symmetric around its maxima points except for the fact that the nodes do not reach zero. The nodes of the Fraunhofer pattern at the point of insertion of a full quantum flux and at each insertion the maximum critical current decreases or increases depending on the direction of the magnetic field. Hence

if n is the vorticity associated, then the equation for the Fraunhofer pattern can be written as ,

$$I_s = I_c(n) \left| \frac{\sin(\pi\phi/\phi_0)}{\pi\phi/\phi_0} \right| \quad (1.25)$$

where, $I_c(n) = I_c(0) + \text{sign}(B_z)\text{sign}(B_{\parallel})nI'_c$, where I'_c is a constant. Similar experimental result on a straight junction was reported in ref [53]. We note here that both of these observations defers from the observations of non-reciprocal super current in Josephson junctions fabricated from similar heterostructures[54] where critical current asymmetry depends on the current direction.

We also measured the Fraunhofer interference for the curved junction for different angles of in-plane fields, in particular, that shown in fig 1.18. We applied a magnetic field of 100mT. When $\theta = 45^\circ$, the component along the junction, B_l , points along the same direction relative to the junction with maximum magnitude at the middle. This causes asymmetry in the Fraunhofer pattern similar to the effect of B_{\parallel} in the straight junction. The field component perpendicular to the junction, B_p , points in opposite direction in the two sections. In the middle B_p vanishes. For $\theta = 135^\circ$, B_l points in opposite direction relative to the junction and vanishes at the middle. Whereas B_p points along the same direction with maximum magnitude at the middle. This causes the Fraunhofer pattern to be symmetric but the critical currents are much more suppressed, similar to the effect of B_{\perp} on the straight junction. The extracted current distribution only shows a suppression of the critical current distribution and no other patterns upon rotating the magnetic field.

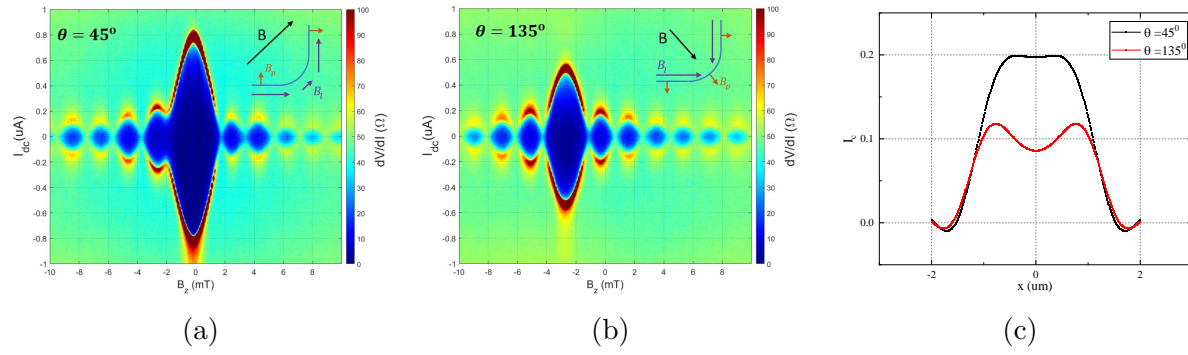


Figure 1.18. Development of Fraunhofer pattern in curved junction with in-plane magnetic field of magnitude 100mT for a) $\theta = 45^\circ$ and b) $\theta = 135^\circ$. c) The extracted current distribution from a) and b).

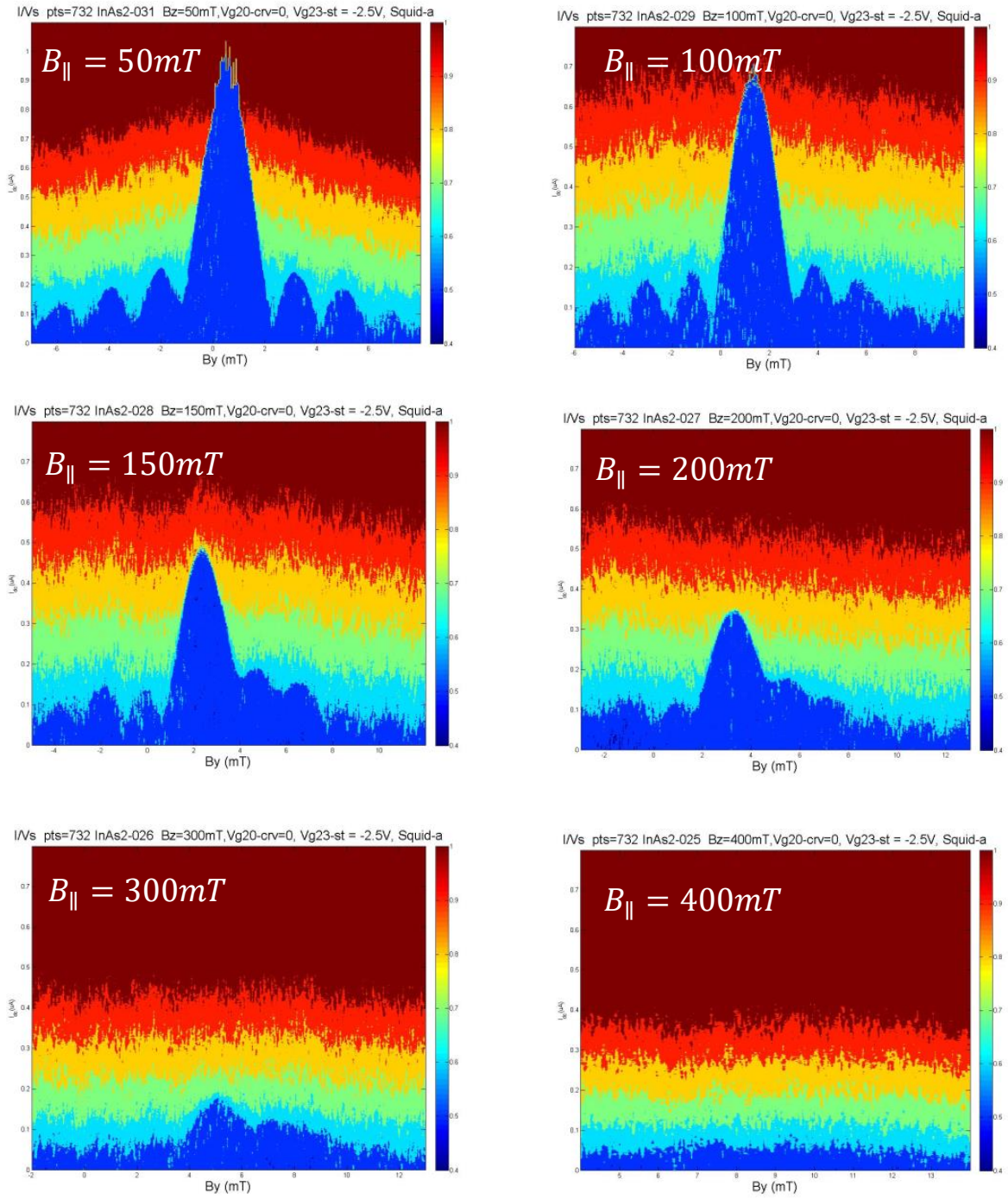


Figure 1.19. Evolution of Fraunhofer pattern with B_{\parallel} in a curved junction

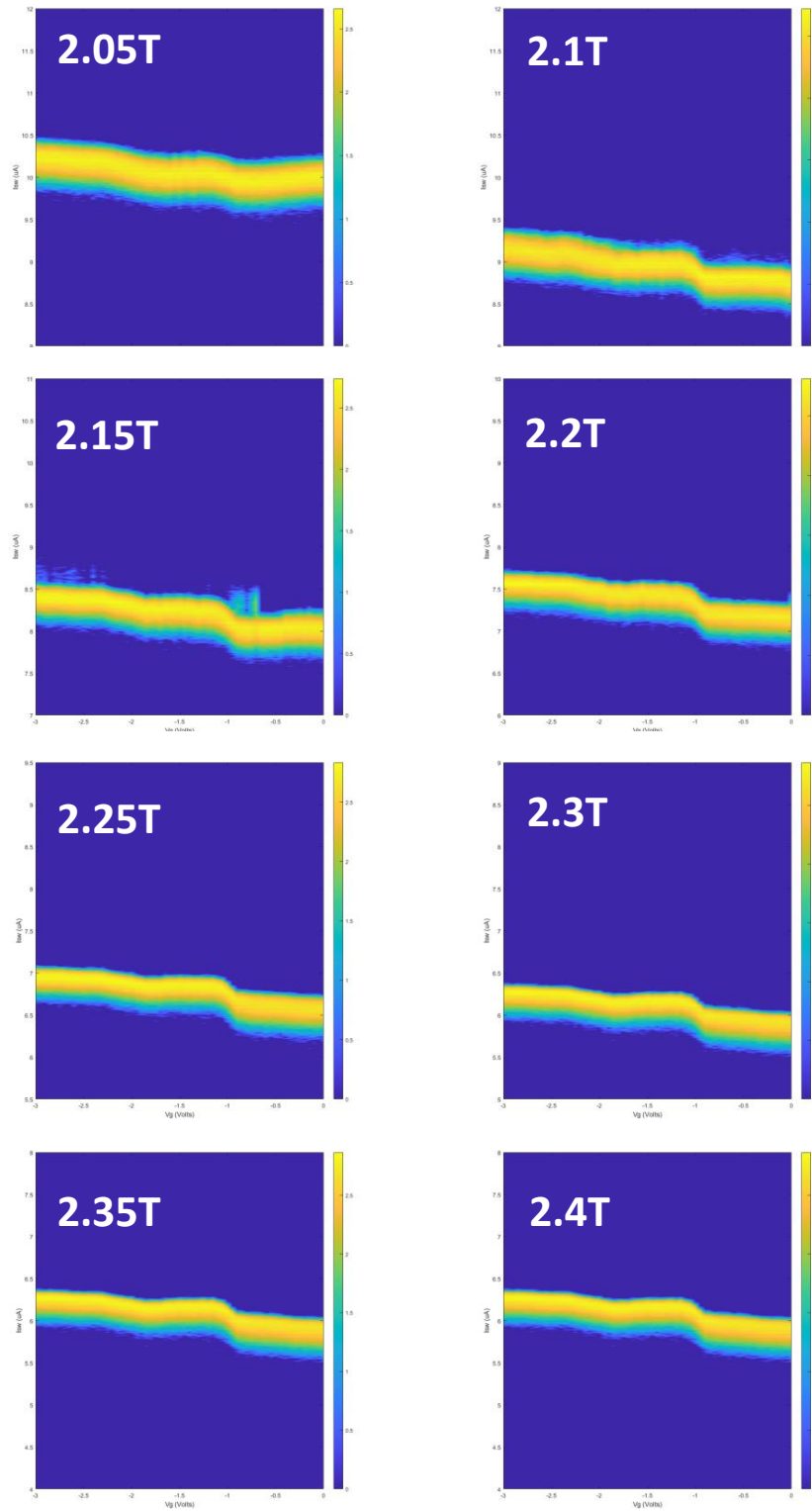


Figure 1.20. Effect of gate on critical currents for different in-plane fields for device A

1.4 A note about Josephson penetration depth

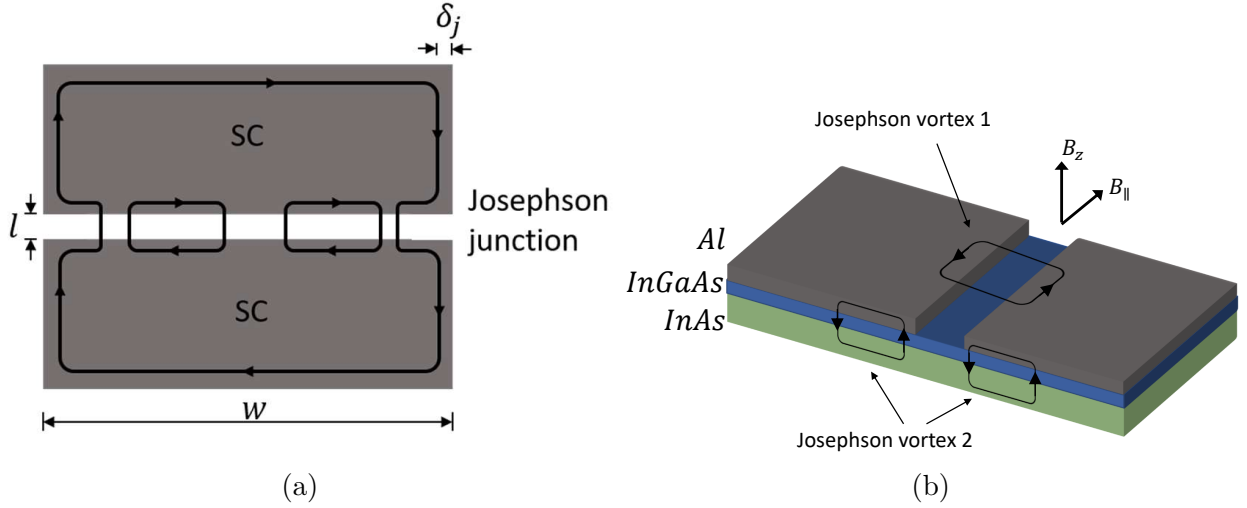


Figure 1.21. a) Formation of Josephson vortices in a wide Josephson junction. b) Vortices can be formed in the vertical heterostructure too producing additional non-reciprocal effects which could lead to asymmetric Fraunhofer patterns.

In the previous calculations, effects of the screening currents were ignored. In order to account for the screening currents, we can assume a vector potential, $\vec{A} = B_z(y)x\hat{y}$, where the magnetic field is pointed along \hat{z} , and write eq 1.23 in the form,

$$\gamma(y + dy) - \gamma(y) = \frac{2\pi}{\phi_o} B_z(y) l dy, \quad (1.26)$$

$$B_z(y) = \frac{d\gamma}{dy} \frac{\phi_o}{2\pi l} \quad (1.27)$$

employing Maxwell's equation,

$$\nabla \times \vec{B} = \mu_o \vec{j} = \mu_o \vec{j}_c \sin \gamma \quad (1.28)$$

$$\frac{d^2 \gamma}{dy^2} = \frac{\sin \gamma}{\delta_j^2} \quad (1.29)$$

where,

$$\delta_j = \sqrt{\frac{\phi_o}{2\pi j_c \mu_o l}}. \quad (1.30)$$

δ_j is the Josephson penetration depth. Eq 1.29 is the sine-Gordon equation. If j_c is sufficiently small, such that $\delta_j > w$, then we can ignore the effect of screening currents. But if $\delta_j < w$, screening effect must be considered while calculating the currents. The screening currents flow in both the superconductors in a layer of width, δ_j as shown in fig 1.21a. In case of strong fields, the sine-Gordon equation can have a "soliton" type solution,

$$\gamma(y) = 4 \arctan [e^{(y-y_o)/\delta_j}]. \quad (1.31)$$

This leads to the formation of Josephson vortices, with each vortex carrying a flux quantum, as depicted in 1.21a[55], [56]. For the Josephson junctions we fabricated, $j_c \approx 50$ uA/um², $l \approx 2 \mu\text{m}$ and $\delta_j \approx 1\text{mm} \gg w$. Hence, we can ignore the effects of screening currents here. But it becomes interesting and relevant when such vortices are formed not in the planar Josephson junction but in the vertical heterostructure as shown in fig 1.21b. Our devices are fabricated from a heterostructure of Al/InAs where the Al induces superconductivity into InAs. Josephson coupling between Al and InAs layers is strong and in the presence of in-plane magnetic field Josephson vortices can form between the layers. Formation of such vortices and associated effects of critical current non-reciprocity are discussed in Chapter 3.

1.5 Conclusion

In conclusion, in this chapter we investigate whether signatures of Majorana zero modes (MZMs) can be detected in the shape of Fraunhofer patterns. However, our attempts to observe these signatures in Josephson junctions (JJs) were hindered by two main challenges. Firstly, the critical in-plane magnetic field of the JJs was found to be significantly lower than the field of a $0 - \pi$ transition, another signature of the topological transition[46]. Secondly, strong flux focusing was found to alter current flow in the junction and further mask any

enhancement of current associated with boundaries between topologically distinct phases. Despite these obstacles, we observed intriguing effects resulting from the in-plane magnetic field in the asymmetric evolution of the Fraunhofer pattern. This observation suggests the existence of additional underlying physics in the studied heterostructure, which may have been previously overlooked. As a result, we have decided to pursue our next idea of realizing a topological superconductor (TSC) using nanowires, acknowledging the potential for novel findings and advancements in this direction.

2. STATISTICS OF SWITCHING CURRENT IN A RING

2.1 Introduction

The experimental investigations conducted on Josephson junctions have provided valuable insights into the characteristics of our heterostructures and the challenges associated with establishing a boundary of a topological superconductor (TSC) within a curved Josephson junction. Our initial attempt to localize Majorana zero modes (MZMs) in the region between the two superconducting banks of the Josephson junction proved unsuccessful primarily due to the premature loss of superconductivity at low in-plane magnetic fields and the occurrence of flux focusing effects, masked the signatures of a topological boundary. Consequently, we have shifted our focus to a new approach involving the localization of MZMs in nanowires. But a direct probe is difficult as the transport properties will be dominated by Al in an Al/InAs heterostructure in its superconducting state. Therefore, we have opted for an indirect probing method, which involves analyzing the statistics of switching current of the nanowire.

Quantum fluctuations of order parameter play a major role in superconducting transitions[57]. Intrinsic quantum fluctuations can induce phase slip events called quantum phase slips (QPS), which have been studied extensively [58]–[60]. QPS are often regarded as the dual counterpart of Josephson junctions [61]. Experimental observations of QPS have been reported in nanowires [62]–[64]. In our study, we aim to explore the possibility of detecting Majorana zero modes (MZMs) using similar methods. The presence of MZMs is associated with a 2π winding of the superconductor’s phase, enabling them to act as phase slip junctions [38], [65]. Thus, our investigation focuses on determining if we can identify signatures of MZMs as QPS centers and observe corresponding effects in the statistical properties of the switching current [62], [63].

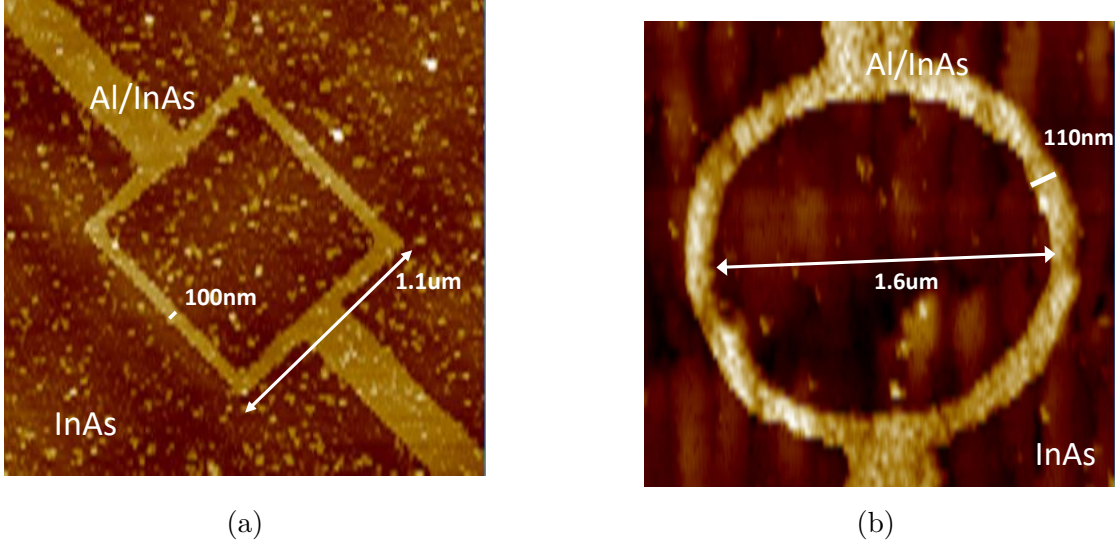


Figure 2.1. AFM images of a) device A and b) device B. The yellow regions are Al/InAs, in the dark regions Al is etched away exposing InAs. A transparent layer of AlOx covers the entire device. A Ti/Au gate layer (not shown in image) is subsequently added on top.

We extended the bend nanowire design in fig 1.2a into a doubly connected structure: a ring. We measured two devices A and B fabricated from Al/InAs quantum well wafers M and J respectively. These wafers have similar heterostructure design with a the major differences in the thickness of Al layers (7nm for wafer M and 20nm for wafer J) and surface morphology shown in the AFM image in fig2.4a and 2.4b. For further details regarding the heterostructure, refer to Chapter 4.

2.2 Critical current oscillations in a superconducting ring

A superconducting ring is governed by the relation

$$\oint dlv = 2\pi\hbar/m(n - \phi/\phi_0) \quad (2.1)$$

where n is a quantum number and ϕ is the external flux through the ring. The diamagnetic persistent current flowing through the ring is given by,

$$I_p = C(n - \phi/\phi_0) \quad (2.2)$$

where, $C = f(l, A, n_s, m)$. For the simple case of a symmetric ring with constant properties throughout the ring,

$$C = 2An_s e\pi\hbar/ml \quad (2.3)$$

and the kinetic energy of the system becomes,

$$E_n = \frac{C}{2}\phi_0\left(n - \frac{\phi}{\phi_0}\right)^2 \quad (2.4)$$

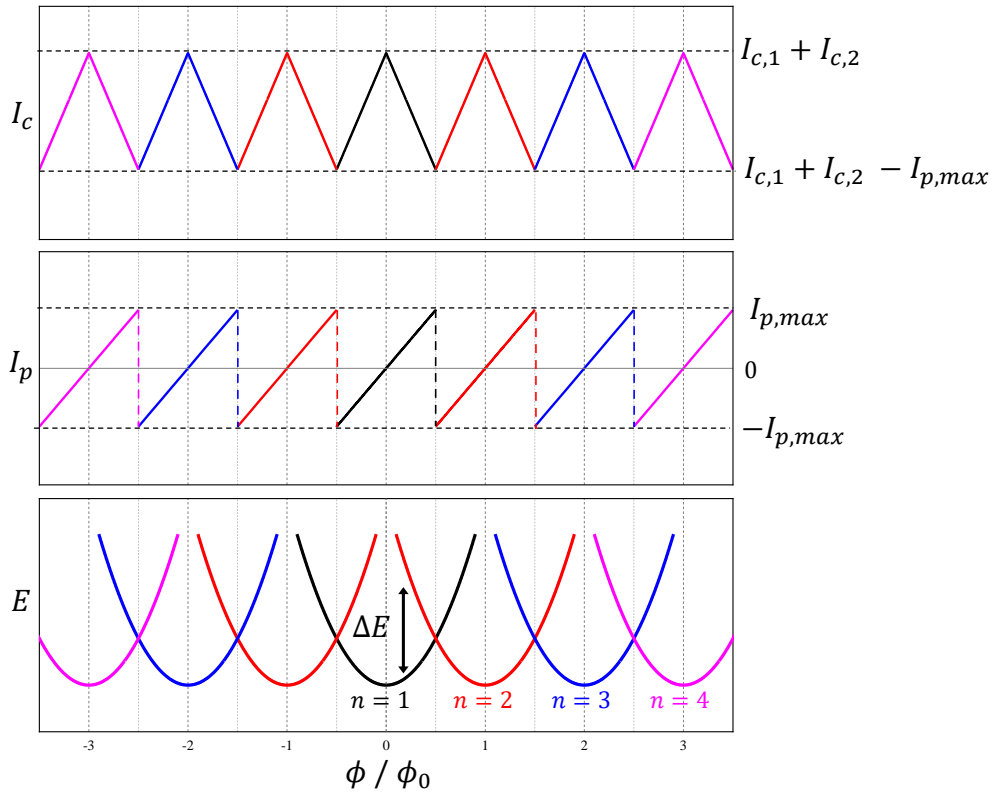


Figure 2.2. switching current dynamics for a symmetric ring. The kinetic energy curves (bottom) corresponding to the vorticity n cross each other when half fluxes ($\phi/\phi_0 = n + 1/2$) are inserted. The energy gap ΔE between two such curves exponentially suppresses the probability of the second metastable state which is reflected in the bimodal switching current distribution in fig.2.4a. The persistent currents I_p (middle) switches sign at the crossing points. Correspondingly the critical current of the ring oscillates (top) with a maxima at integer flux quantum and a minima at half fluxes (where I_p is maximum).

The kinetic energy and the persistent current variation as a function of ϕ/ϕ_0 is illustrated in fig 2.2. The vorticity is different for different parabolas. If the system evolves adiabatically, the system stays in the ground state, changing vorticity at every crossing point of the parabolas($\phi = (n + 1/2)\phi_0$). If there is a rapid change of parameters(such as a rapid change of current through a nanowire), there is a finite probability, for the system to remain in an excited state, exponentially suppressed by the energy gap ΔE . This is evident in the switching current current statistics in fig.2.4a which shows the histogram of switching currents for $N = 10000$ as a function of out-of-plane magnetic field B_z . The color scale represents the counts in a logarithmic scale. The inset shows a single histogram at $B_z = -1.6mT$, where the vertical axis shows counts in logarithmic scale, which is near a crossing point. Clearly, the first peak is exponentially smaller than the second peak conforming to the theoretical illustration of energy variation in fig 2.2. At the crossing points of parabolas the persistent current I_p switches sign.

On applying an external current I_{ext} with $B_z = 0$ the currents are distributed between the two arms in the inverse ratio of the kinetic inductances of the two arms L_k as illustrated in fig.2.3.

$$I_1/I_2 = L_{k2}/L_{k1} \quad (2.5)$$

Since the ring is symmetric $L_{k1} = L_{k2}$. Hence,

$$I_1 = I_2 = I_{ext}/2 \quad (2.6)$$

Thus the effective critical current becomes $I_{c,eff} = 2I_c$. When $B_z \neq 0$ I_p adds to the current through one arm and subtracts from the other giving,

$$I_1 = I_{ext}/2 + I_p \quad (2.7)$$

$$I_2 = I_{ext}/2 - I_p \quad (2.8)$$

Note here that the entire ring turns normal when the current through either of the arms exceeds its respective I_c . Thus $I_{c,eff}$ is determined by whichever arm turns normal first. In this case for $B_{\perp} > 0$ since $|I_p|$ adds to I_1 $I_{c,eff}$ is determined by arm 1,

$$I_{c,eff} = 2I_c - 2I_p = 2I_c - 2CB_{\perp} \quad (2.9)$$

when $B_{\perp} < 0$, $|I_p|$ adds to I_2 $I_{c,eff}$ is determined by arm 2 but takes the same form as before giving,

$$I_{c,eff} = 2I_c - 2I_p = 2I_c + 2CB_{\perp} \quad (2.10)$$

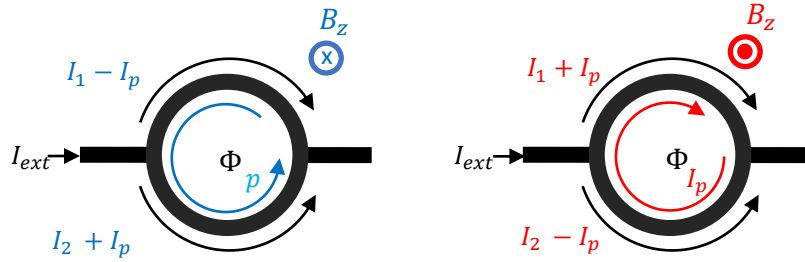


Figure 2.3. In a symmetric ring the external current is distributed equally between the two arms. For $B_z \neq 0$ the persistent current I_p adds and subtracts to the either of the arms depending on the direction of B_z and vorticity n of the ring.

Thus $I_{c,eff}$ falls linearly and symmetrically as the magnitude of B_{\perp} is increased in either directions. The same effect is repeated at every addition of half a flux quantum, when I_p switches sign and the arm determining the $I_{c,eff}$ also switches repeating the triangular pattern as illustrated in the top section of fig2.2.

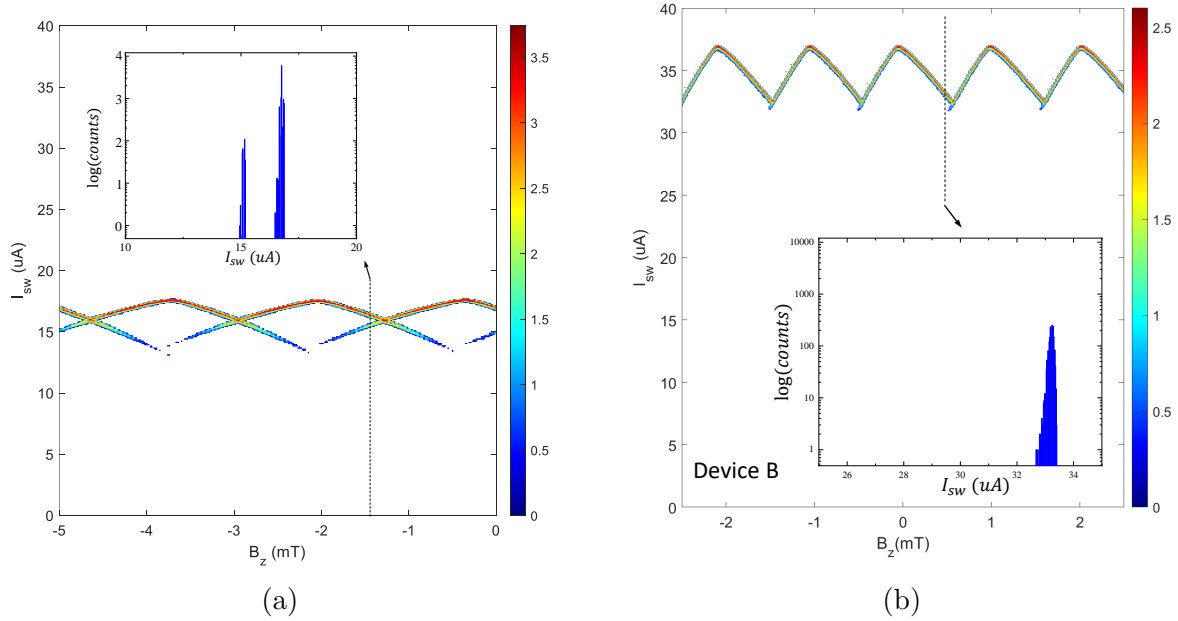


Figure 2.4. Contour plots of histogram of switching current as function of B_z of a) device A and b) device B. The color scale indicates the counts in a logarithmic scale. Device A shows normal oscillations and bimodal histogram corresponding to the meta-stable states associated with multiple vorticity. The lower peak is exponentially suppressed as is obvious from the exponentially smaller peak value in the line cut shown in the inset. Device B shows an unusual behaviour where the bimodal distribution is not seen near the minima indicating the absence of meta-stable states which is also seen in the line cut in the inset.

2.3 Switching current statistics in superconducting rings

In order to measure the switching current statistics the current was ramped from 0 to a large value and the voltage across the ring was measured. The voltage jump from zero to a non-zero value was detected and the corresponding current was recorded. The process is repeated N times with a typical value of $N = 10000$. The standard deviation and mean value was computed in a standard way.

Switching current statistics of device A and B is shown in fig 2.4a and 2.4b respectively. Here, the histograms of switching currents are plotted in the vertical axis where the color represents the counts in a logarithmic scale. The insets display the line cuts showing the histogram for a fixed value of B_z on a logarithmic scale.

In device A the switching current I_{sw} follows the discussion in section 2.2. I_{sw} oscillates with a period $\Delta B \approx 2mT$ matching the calculated period $\Delta B = \phi_0/A_{loop}^A$ where A_{loop} is the area of the ring. The switching current distribution is multi-valued due to the meta-stable states associated with the winding number n of the order parameter (vorticity). The vorticity fluctuates between the nearest number near the crossing points with the state with higher energy exponentially suppressed. This is evident from the exponentially different heights of the peaks in fig 2.4a. Similar statistics and oscillations of the switching current has been previously observed [66], [67] in superconducting rings.

The I_{sw} statistics of device B is significantly different from device A as shown in fig 2.4b. We observe that the histogram oscillations do not show any signs of a double distribution associated with the fluctuations in n . The vertical cut (inset) shows only a single peak in logarithmic scale showing no signs of meta-stable states. The periodicity of the oscillations match the theoretically calculated value $\Delta B = \phi_0/A_{loop}^B \approx 1mT$.

2.4 Effect of in-plane magnetic field

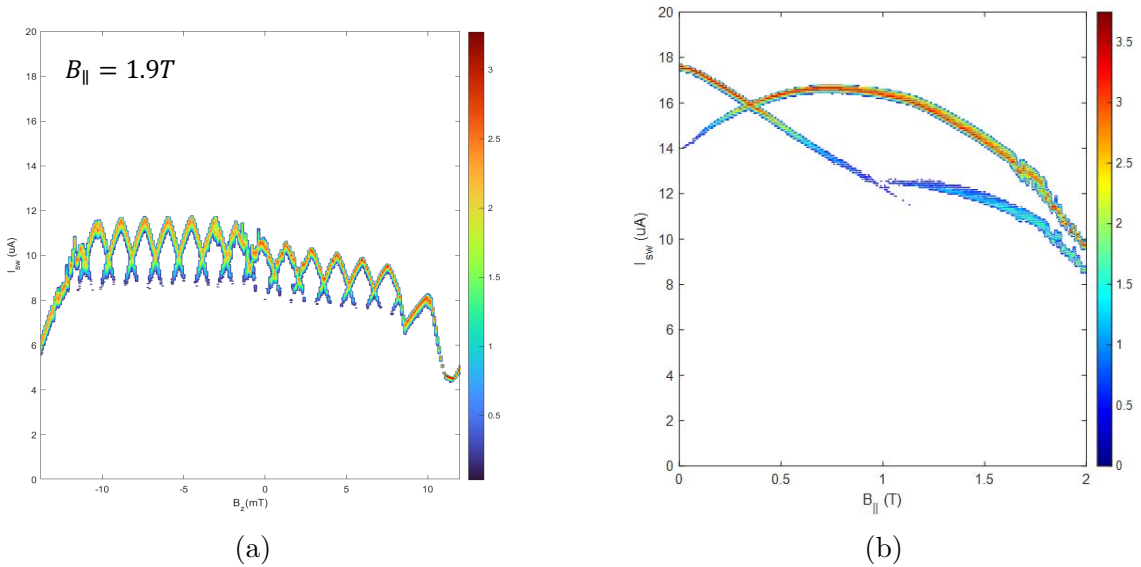


Figure 2.5. a) Contour plot of histograms of switching currents in device A at $B_{\parallel} = 1.9T$. b) Histogram of switching currents as a function of B_{\parallel} shows an anti-crossing at $B_{\parallel} = 1.8T$.

Fig 2.5a shows the switching current statistics as a function of B_z when in-plane field $B_{\parallel} = 1.9T$ is applied. The switching current is suppressed to about 50% of its value at $B = 0$. We do not notice any other significant effect of B_{\parallel} . But we notice a unique anti-crossing behaviour in the plot of I_{sw} vs B_{\parallel} as seen in fig 2.5b. B_{\parallel} exhibits a slight misalignment of $\phi \approx 0.05^\circ$, resulting in a non-zero B_z component. The distribution in this scenario follows the expected behavior, with a crossing point observed at $B_{\perp} \approx 0.4$ T. At $B_{\perp} \approx 1.8$ T, an anti-crossing is observed instead of the expected crossing. This implies a gap opening in the $E - B_z$ curve shown in fig2.2. But the absence of any such signatures in in fig 2.5a is intriguing.

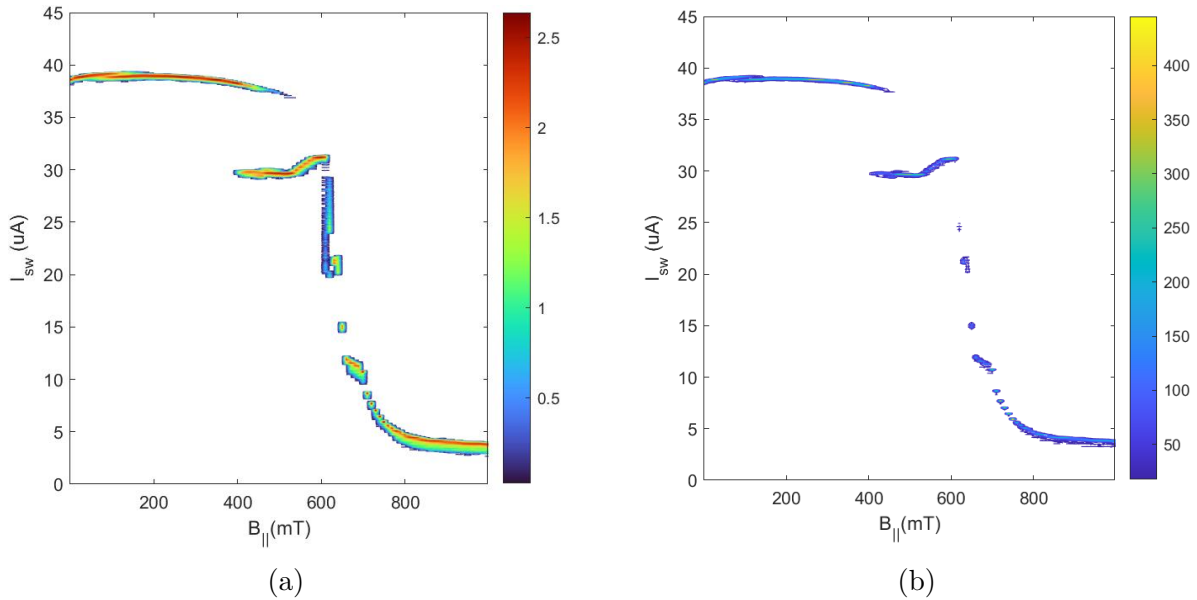


Figure 2.6. switching current distribution as function of in-plane magnetic field B_{\parallel} in a) logarithmic and b) linear scale. The distribution turns bimodal distribution of switching currents is observed for $B_{\parallel} > 400mT$. This is not the same as the meta-stable states as the lower arm of the distribution is not exponentially suppressed.

The I_{sw} distribution in device B under B_{\parallel} is shown in fig 2.6a. Initially, a slight increase in I_{sw} is observed, reaching a maximum at $B_{\parallel} \approx 0.2$ T (A similar behavior was also observed in the nanowires discussed in Chapter 3, suggesting a common underlying mechanism). Notably, an unexpected and surprising behavior manifests itself at $B_{\parallel} = 0.4$ T in device B. The histogram exhibits a bimodal distribution, a departure from the single-peaked distribution

observed in other regions. Importantly, this bimodal distribution is observed specifically within the range of $0.4 \text{ T} < B_{\parallel} < 0.5 \text{ T}$. It is crucial to emphasize that this bimodal distribution is distinct from the bimodal behavior caused by fluctuations in the vorticity of the ring, where the distribution is exponentially suppressed due to the presence of an energy gap. In contrast, the bimodal distribution observed in this case remains observable and comparable, even in a linear color plot as seen in fig 2.6b.

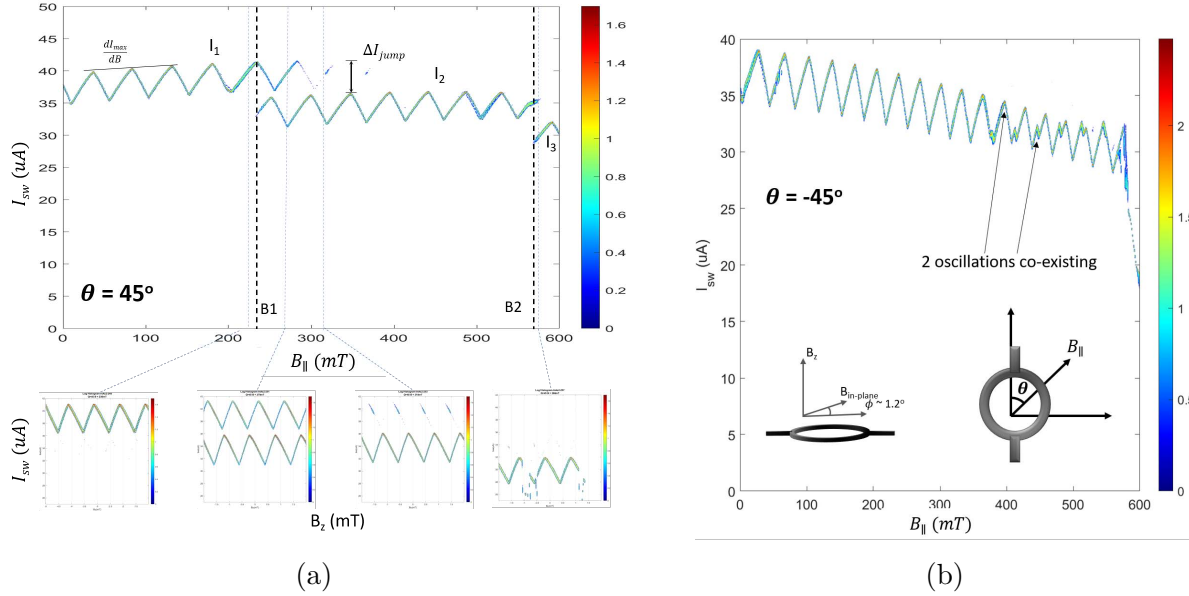


Figure 2.7. Histogram of switching currents as a function of in-plane magnetic field B_{\parallel} for a) $\theta = 45^\circ$ and b) $\theta = -45^\circ$. A field misalignment of $\phi = 1.2^\circ$ effects in a small B_z component for B_{\parallel} which provides more information regarding the nature of the bi-stable states. The colors represent the counts in a logarithmic scale. The bottom plots in a) shows the I_{sw} distribution as function of B_z at fixed B_{\parallel} showing the transition between the two bi-stable states.

Further insights into the bimodal distribution is gained by intentionally misaligning B_{\parallel} by an angle of approximately 1.2° . This deliberate misalignment allows for a comparison of the vortex state of the ring in two distinct states. Fig 2.7a and 2.7b summarizes all the different observations. First, the two multi-valued states have phase difference of approximately π , as evidenced by the phase-shifted oscillations of the switching current (I_{sw}) shown in Fig. 2.5 fro $\theta = 45^\circ$ where θ is the angle between the in-plane field and the current direction. Second we observe two bimodal distribution, the first beginning at $B_{\parallel} = B_1$ and the second at B_{\parallel}

$= B_2$. For $\theta = -45^\circ$ we observe that the bimodal distribution vanishes but a new set of phase shifted oscillations intertwined starts at $B_{\parallel} \approx 400mT$. A complete set of data showing the dependence of the statistics on θ is plotted in fig 2.8 where there is no B_z component for B_{\parallel} and in fig 2.9 where a small misalignment is present. A summary of the extracted parameters from these plots is shown in fig 2.10. The slope, $\alpha = \frac{dI_{\max}}{dB_{\parallel}}$, plotted as a function of θ shows a sinusoidal oscillation with the maxima and minima occurring around $\theta = 90^\circ$ and $\theta = 270^\circ$. This results from the non-reciprocity due to the diamagnetic currents in the Al-InAs multilayer structure[68]. When the direction of the current is inverted, the slope of the entire curve is inverted, as shown in fig 2.11 which, again, shows the non-reciprocal superconductivity due to the diamagnetic response to in-plane field. B_1 stays between $200mT$ and $400mT$ while $B_2 \approx 600mT$ only for specific values of θ . The gap between the peaks of the bimodal distribution ΔI_{jump} remains constant in magnitude switching sign around $\theta = 150^\circ$.

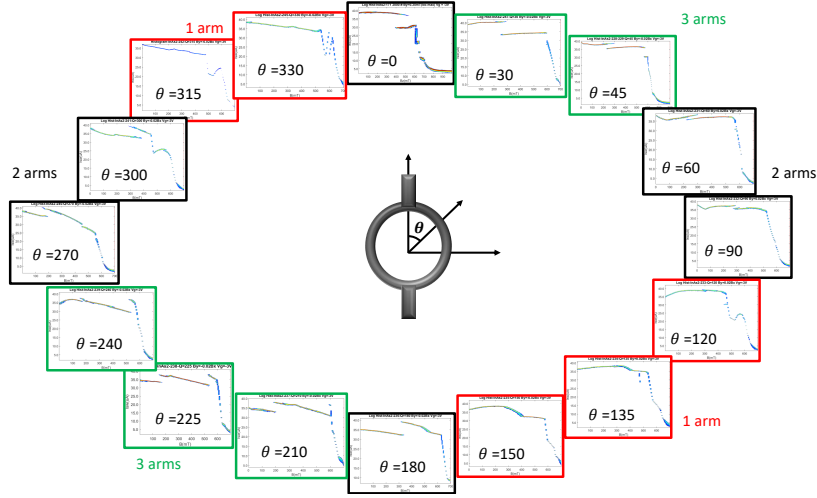


Figure 2.8. Complete set of data for the histogram of switching currents as a function of in-plane magnetic fields for different θ .

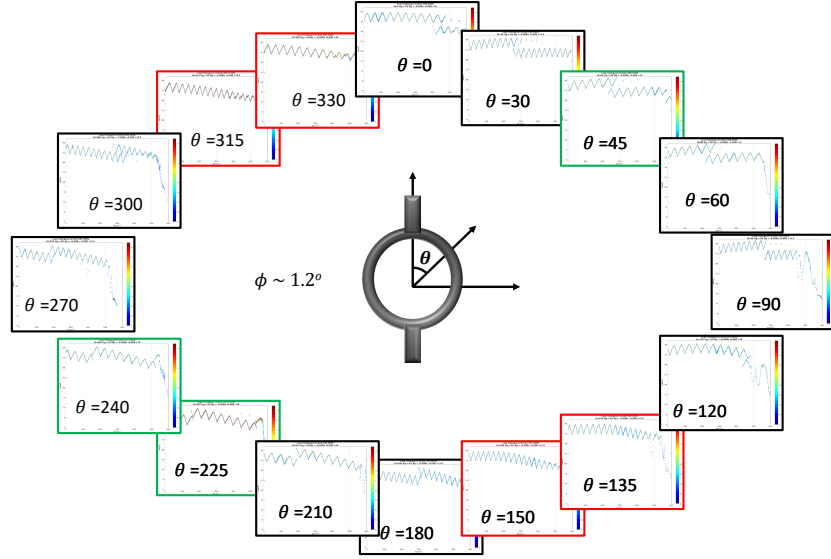


Figure 2.9. Complete set of data for the histogram of switching currents as a function of in-plane magnetic fields for different θ with slightly misaligned magnetic field producing a B_z component.

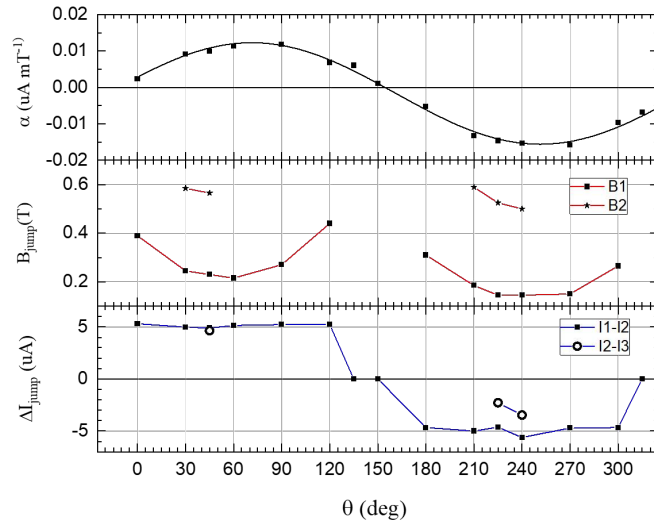


Figure 2.10. Plot of extracted parameters as a function of θ for device B. The slope $\alpha = \frac{dI_{\max}}{dB_{\parallel}}$ varies sinusoidally with angle θ with a maxima and minima at $\theta = 90^\circ$ and $\theta = 270^\circ$ where the perpendicular component B_{\perp} has the maximum magnitude. B_1 stays between $200mT$ and $400mT$ while $B_2 \approx 600mT$ only for specific values of θ . The gap between the peaks of the bimodal distribution ΔI_{jump} remains constant in magnitude switching sign around $\theta = 150^\circ$.

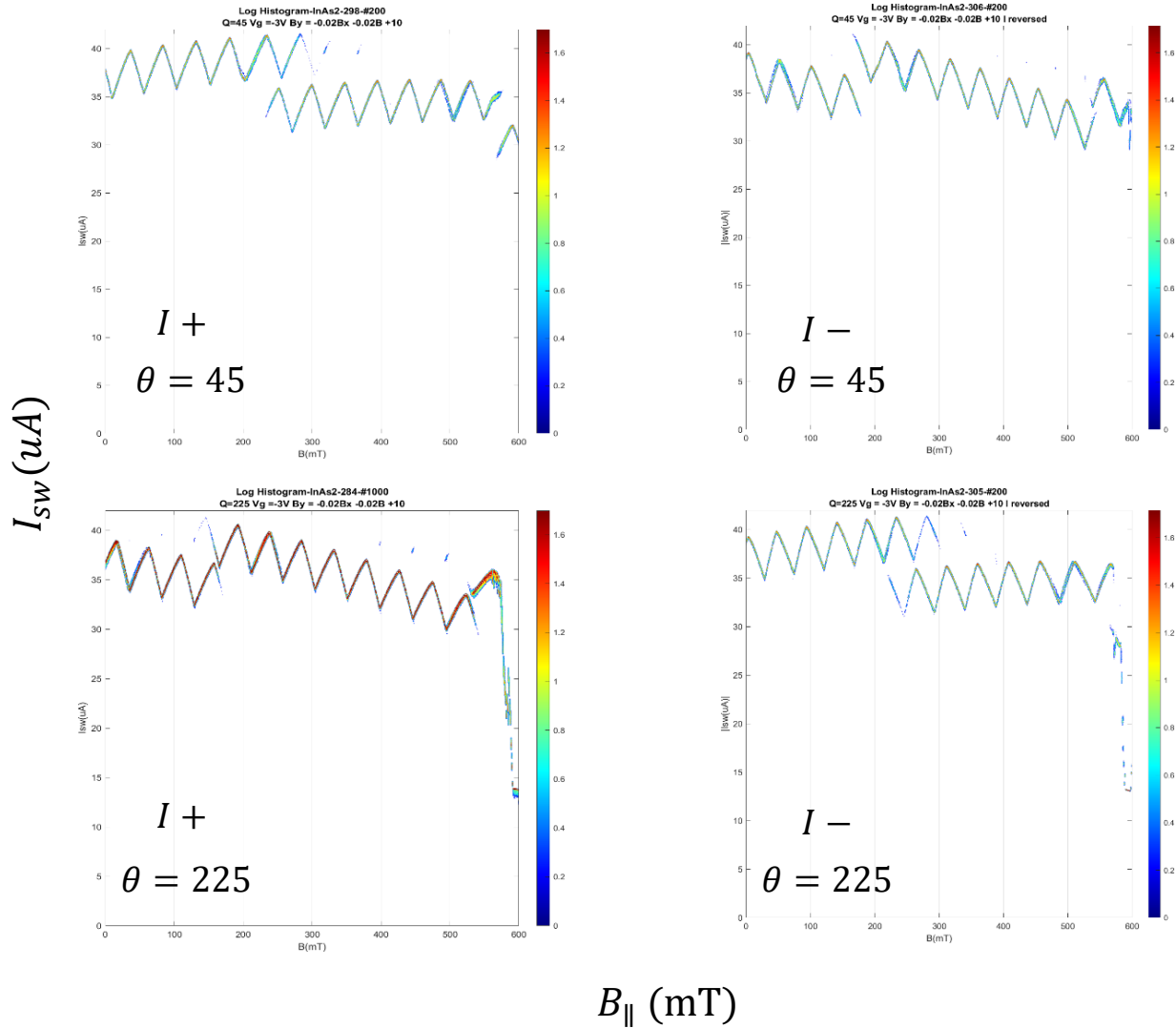


Figure 2.11. a) When the direction of current is inverted, the slope of the entire curve is inverted which results from the non-reciprocity due to the diamagnetic currents in the Al-InAs multi-layer structure.

2.4.1 Effect of gating

One of the unique and unexpected observations of the effect of gating on switching currents is that the switching current shows an increase in magnitude on applying negative gate voltage as shown in fig. 2.12. Such a behaviour was observed on multiple superconducting devices. The underlying physics is not clearly understood yet although we hypothesize the physics as follows. On applying a negative gate voltage the InAs around the superconductor

is depleted of conducting electrons and the superconducting gap is hardened. This reduces scattering of electrons into the normal regions from the superconducting InAs. This could potentially increase the current current. The increase is very small ($< 1\%$) albeit observable within the precision of our measurement technique. Detailed contour plots of gating is shown in fig. 1.20 in appendix.

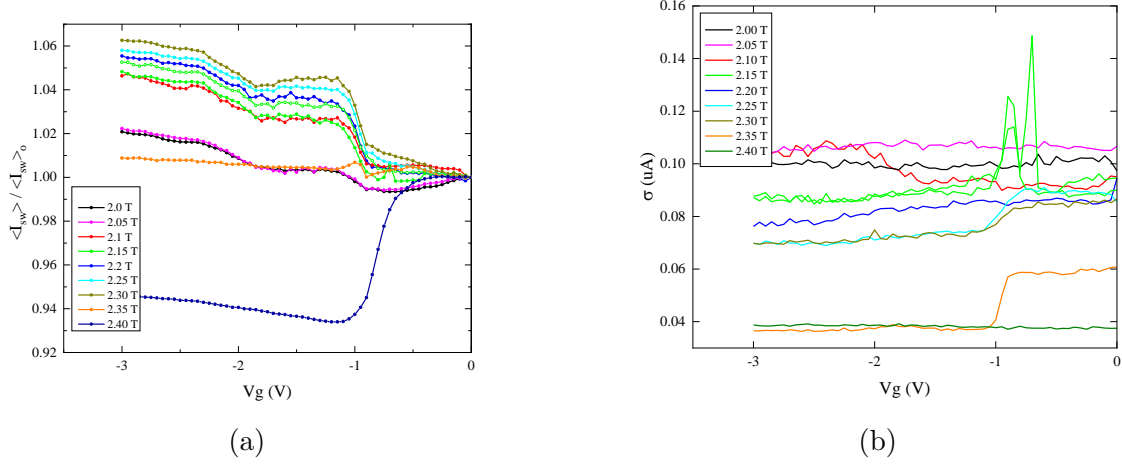


Figure 2.12. a) A negative gate voltage causes the switching current to increase for $B_{||} < 2.35T$. b) Standard deviation as a function of gate voltage for different $B_{||}$

2.4.2 Effect of temperature

As seen in fig 2.13, on cooling down device A we observed that the mean value of the switching current follows an expected Bardeen relation[69]. The standard deviation decreases initially until $T = 800$ mK and then remains constant. This is a unique behaviour associated with a quantum phase transition from a thermally activated phase slip regime to a quantum phase slip regime[62], [63]. But we did not see any other signatures and hence cannot confirm conclusively of any phase transitions.

Another remarkable phenomenon emerges in device B. The theoretical curves for the Bardeen dependence of I_c on temperature and the BCS energy gap Δ_{BCS} are also displayed. Strikingly, the experimental curve aligns with the curve corresponding to $\Delta_{BCS}(T)$ rather than $I_c(T)$, defying our expectations.

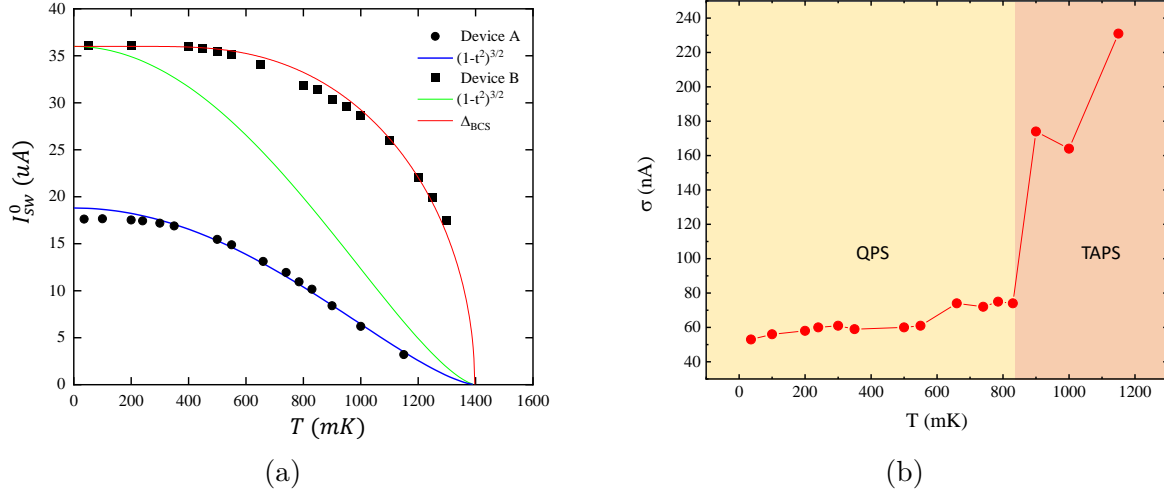


Figure 2.13. a) The switching current follows the Bardeen relation[69] b) Standard deviation decreases and saturates below $T = 800mK$ which is a signature of quantum phase transition from a thermally activated phase slip regime to a quantum phase slip regime.

It is important to mention that several additional circular loop devices from the same wafer (wafer J) were fabricated and measured. However, this effect was not observed in any other devices. Nevertheless, the observed phenomenon in device B remained robust across multiple cooling cycles. Furthermore, no abnormal features were detected in the AFM image of the device. Regrettably, the origin of these observations has not yet been comprehensively understood. We speculate that the underlying physics may be intricately linked to the mechanisms governing non-reciprocal effects in multi-layer superconductors, combined with non-uniform material parameters within the specific region of the wafer where the ring is fabricated. This motivated us to further study superconducting nanowires fabricated from this heterostructure.

2.5 Conclusion

In light of the observed switching current statistics of Device A, although certain distinctive characteristics are present, we have determined that they lack the necessary significance to be considered indicative of a topological transition. However, the remarkable anti-crossing

behavior exhibited at high magnetic fields necessitates further experimentation. The experimental observation of bimodal distribution has provided invaluable insights into the underlying physics of the heterostructure which might have been previously overlooked. Bistable devices form a critical component of quantum computing technologies. Nevertheless, the non-reproducibility of our devices raises concerns and emphasizes the need for further investigation. Consequently, we have embarked on additional experimental investigations concerning Al/InAs superconducting nanowires. In Chapter 3, we discuss non-reciprocal superconductivity, which, when combined with local non-uniformity in heterostructure growth, emerges as the most plausible explanation for the observed bimodal distribution.

3. NON-RECIPROCAL CRITICAL CURRENT IN A NANOWIRE

3.1 Introduction

This chapter presents an experimental investigation of the non-reciprocal critical current (NRC) in nanowires fabricated from an Al/InAs hybrid heterostructure. The primary objective of this study is to unravel the underlying origin of this observed non-reciprocity. By carefully designing and fabricating the nanowires, we gain insights into the fundamental physical mechanisms governing the NRC phenomenon. We discover that the mechanism is applicable to any generic multi-layer superconductors. Our findings provide a compelling explanation to the NRC observed in previous works [70] and [71] and can lead to development of future applications.

3.2 Observation of non-reciprocal critical current in a nanowire

The term “superconducting diode effect” has been used to describe NRC in different systems, including thin superconducting films [72]–[77] and Josephson junctions [54], [78]–[85]. In the former experiments the presence of out-of-plane magnetic field and formation of vortices is essential for the observation of NRC, in this case the critical current is determined by the strength and symmetry of the flux pinning potential. In the latter case the critical current in Josephson junctions is determined by the overlap of Andreev states. In this paper we restrict our discussion to the origin of NRC in long nanowires, where critical current is determined by the de-pairing velocity of Cooper pairs (the Bardeen limit [69]).

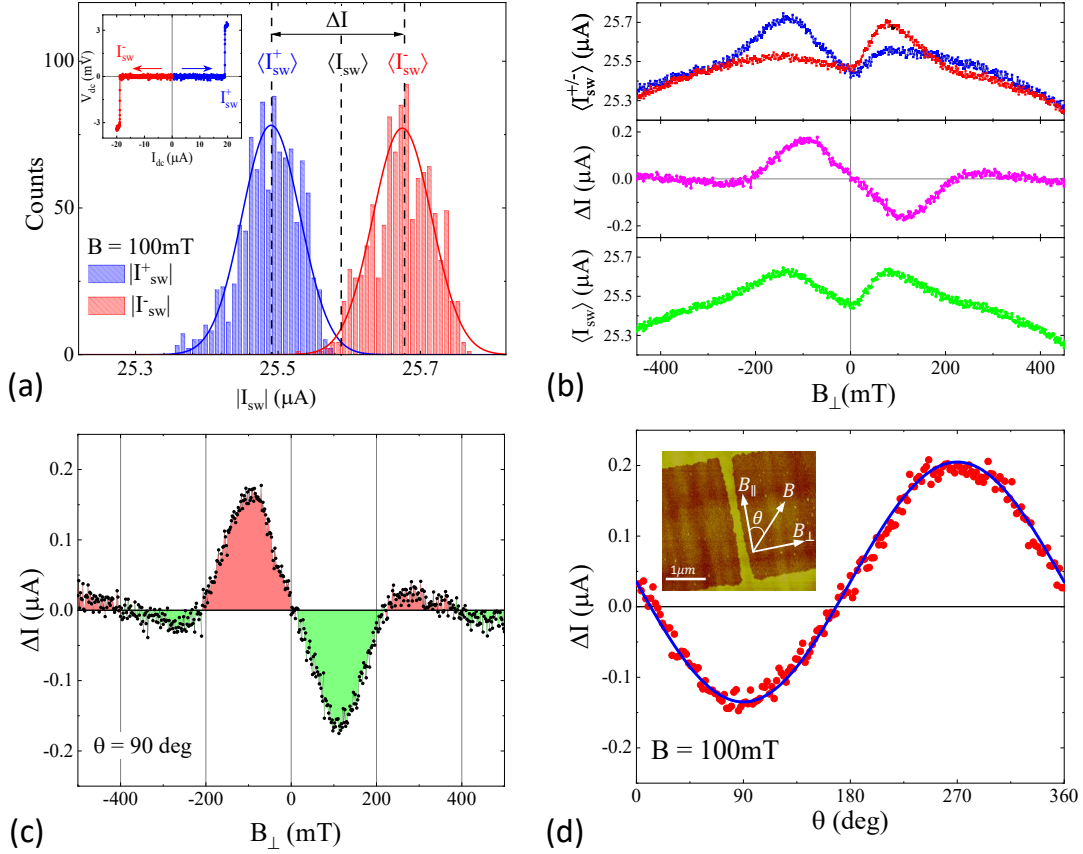


Figure 3.1. Non-reciprocal critical current in Al/InAs nanowires. (a) Histograms of switching currents for 10,000 positive I_{sw}^+ and negative I_{sw}^- current sweeps performed at $T = 30$ mK and $B_{\perp} = 100$ mT. Inset shows a typical current-voltage characteristic. (b) Average switching current for positive $\langle I_{sw}^+ \rangle$ and negative $\langle I_{sw}^- \rangle$ sweeps, non-reciprocal difference $\Delta I = \langle I_{sw}^+ \rangle - \langle I_{sw}^- \rangle$ and an average of all sweeps $\langle I_{sw} \rangle$ is plotted as a function of in-plane magnetic field B_{\perp} . In (c) enlarged ΔI data is colored to signify non-monotonic field dependence and multiple sign changes. (d) Dependence of ΔI on in-plane field orientation is measured at a constant $B = 100$ mT. Blue line is a fit with a sine function. Inset shows an AFM image of a $3 \mu\text{m}$ -long wire connected to wide contacts, yellow areas are Al, in darker areas Al is removed and InAs is exposed.

We have studied switching currents I_{sw} defining a transition from superconducting to normal state in nanowires fabricated from Al/InGaAs/InAs/InGaAs heterostructures [39], where patterned Al top layer forms a nanowire and induces superconductivity in a high mobility InAs quantum well via the proximity effect. An AFM micrograph of a typical

device is shown in the inset in Fig. 3.1. A typical current-voltage characteristic exhibits a sharp switching transition limited by the current resolution (< 5 nA for the fastest sweep rates used in our experiments). A histogram of switching currents I_{sw}^{\pm} for positive (+) and negative (-) current sweeps is shown in Fig. 3.1(a) for 10,000 sweeps. Field dependence of average values $\langle I_{sw}^+ \rangle$ and $\langle I_{sw}^- \rangle$ is plotted in Fig. 3.1(b) for the in-plane field B_{\perp} perpendicular to the wire. The $\langle I_{sw}^+ \rangle$ and $\langle I_{sw}^- \rangle$ can be separated into a symmetric $\langle I_{sw} \rangle = (\langle I_{sw}^+ \rangle + \langle I_{sw}^- \rangle)/2$ and asymmetric $\Delta I = \langle I_{sw}^+ \rangle - \langle I_{sw}^- \rangle$ parts, the latter being the non-reciprocal component of the supercurrent. Both $\langle I_{sw} \rangle$ and ΔI are non-monotonic functions of magnetic field. As shown in the Supplement, a minima of $\langle I_{sw} \rangle$ at low fields vanishes above 350 mK ($0.3 T_C$), while there is no change in ΔI at least up to 750 mK ($> 0.6 T_C$). This difference in energy scales for the appearance of NRC and non-monotonic evolution of $\langle I_{sw} \rangle$ indicates that these are unrelated phenomena, and below we focus on the origin of NRC. Some devices were fabricated with a top gate, which allows electrostatic control of the electron density in the InAs layer not covered by Al; we found that depletion of the 2D electron gas in the exposed InAs results in a slight increase of $\langle I_{sw} \rangle$ but does not affect ΔI . Similar field effect has been observed previously in superconductor nanodevices [86] and was attributed to the presence of quasiparticles [87], a conclusion consistent with the observed gate dependence of the $\langle I_{sw} \rangle$.

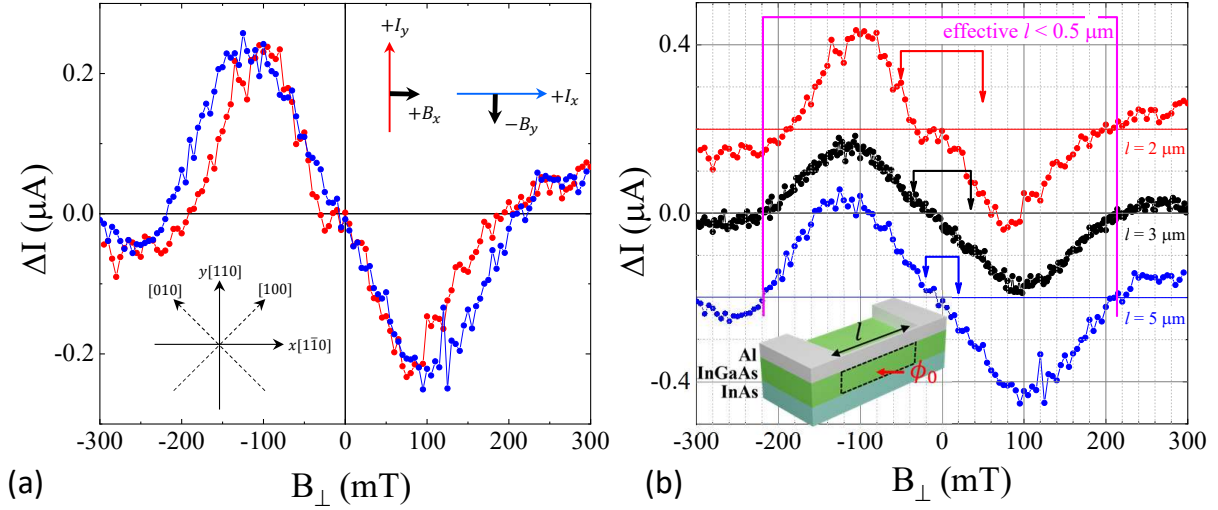


Figure 3.2. Dependence of NRC on the nanowire length and crystallographic orientation. (a) NRC is plotted for two $2 \mu\text{m}$ -long wires oriented along $[110]$ and $[1\bar{1}0]$ crystallographic axes. Insets define mutual orientation of wires and fields. (b) NRC for 2 , 3 , and $5 \mu\text{m}$ wires. The top and bottom curves are shifted vertically by $0.2 \mu\text{A}$. Brackets with arrows indicate a maximum ΔB needed to insert a flux $\phi_0 = h/2e$ in the area defined by the corresponding wire lengths, as indicated by a dashed loop in the inset. An effective length for the period marked by a magenta bracket is $l = 0.5 \mu\text{m}$ for the same loop.

3.3 Diamagnetic source of non-reciprocity

Unlike the linear in Cooper pair momentum terms, higher order terms cannot be removed by gauge transformation and it was shown that the presence of terms $\sim \alpha_3 Q^3 \Delta^2$ cubic in the Cooper pair momentum in an expansion of the Ginsburg-Landau coefficients can generally lead to non-zero ΔI which is a non-monotonic function of B and can even change sign [88], [89] (here $\mathbf{Q} = -i\hbar\nabla - 2e\mathbf{A}$ is a generalized Cooper pair momentum, \mathbf{A} is electromagnetic vector-potential). However, for proximitized InAs layer, a generation of the terms higher order in the Cooper pair momentum in the presence of the Rashba spin-orbit and Zeeman interactions coexists with a similar generation of such terms due to the Dresselhaus spin-orbit interactions. The importance of the Dresselhaus-like terms in the electron spectrum is not limited to proximity structures, and they can play significant role in any noncentrosymmetric material.

Investigation of realistic cubic terms in the Cooper pair momentum showed [90] that nonreciprocity becomes highly anisotropic as a result of Dresselhaus-induced contribution. For comparison with experiments, it is instructive to express the odd in Cooper pair momentum part of the kinetic energy in coordinates rotated by $\pi/2$ with respect to the principal crystallographic axes of InAs, where $\hat{x} \parallel [1\bar{1}0]$ and $\hat{y} \parallel [110]$, see insert in Fig. 3.2(a). In these coordinates, the cubic in the Cooper pair momentum kinetic term originating from the cubic Dresselhaus electron spin-orbit interaction reads

$$f_k = | \kappa(B_y Q_x^3 + B_x Q_y^3 - Q_x Q_y [B_x Q_y + B_y Q_x]) \Delta |^2, \quad (3.1)$$

where coefficient κ contains the Dresselhaus constant β_D and other material parameters. The resulting NRC correction to the supercurrent is

$$\Delta I \propto (B_y I_x^2 + B_x I_y^2). \quad (3.2)$$

This correction is independent of the sign of I and is added or subtracted to the $B = 0$ current value depending on the direction of the current flow. Here B_x and B_y enter symmetrically for wires oriented along x and y . However, in the configuration with the current $I \parallel \hat{x}$ and magnetic field B_y and the configuration with $I \parallel \hat{y}$ and B_x , this expression has opposite signs for the same mutual orientation of I and B , see inset in Fig. 3.2(a). Thus, the Dresselhaus-induced contribution results in NRC with opposite sign for wires oriented along $[1\bar{1}0]$ and $[110]$ crystallographic axis. The cubic (and generally all odd) in Cooper pair momentum terms originating from the Rashba electronic interactions, when added with the Dresselhaus-induced terms, will produce anisotropy in the absolute value of NRC, and, in particular, different values of non-reciprocal asymmetrical component of the current for those two directions. Theoretical investigation of electronic spectra of these systems [91] suggests that in narrow InAs quantum wells cubic Dresselhaus terms are larger than the Rashba terms. The lower limit for the value of the Dresselhaus contribution can be extracted from the total spin-orbit anisotropy (which is defined by the ratio between a linear Rashba, and a linear and cubic Dresselhaus terms in electronic spectrum), which was measured to be

70% in spin-galvanic and circular photogalvanic experiments [92] and $> 15\%$ in transport experiments [93], [94]. Such anisotropies must result in the corresponding crystallographic anisotropy of the NRC, which is not observed in our experiments, Fig. 3.2(a). Therefore, we conclude that the NRC we observed is not intrinsic. The observed NRC does not depend on the wire length, Fig. 3.2b, which rules out trivial effects related to the formation of spurious loops due to the presence of wire/contact boundaries.

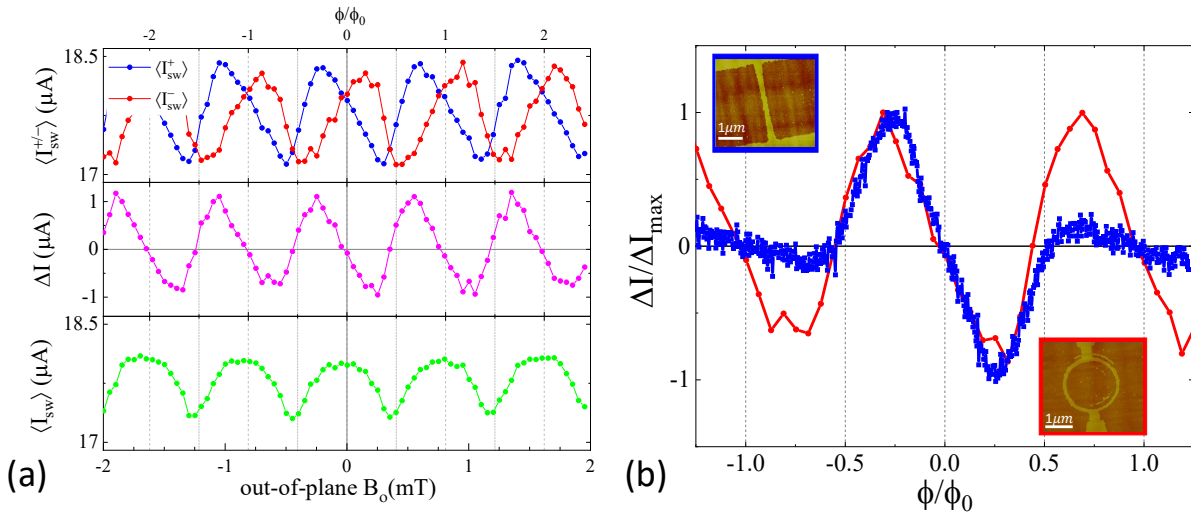


Figure 3.3. NRC in an asymmetric superconducting loop. (a) An average switching current for positive $\langle I_{sw}^+ \rangle$ and negative $\langle I_{sw}^- \rangle$ sweeps, non-reciprocal difference $\Delta I = \langle I_{sw}^+ \rangle + \langle I_{sw}^- \rangle$ and an average of all sweeps $\langle I_{sw} \rangle$ plotted as a function of out-of-plane magnetic field B_o for a loop shown in the insert in (b). Note that $\langle I_{sw} \rangle$ is maximal while $\Delta I = 0$ when the flux $\phi = n\phi_0$. In (b) ΔI for the nanowire and the loop are plotted together as a function of a reduced flux ϕ/ϕ_0 , where we used $S_{wire} = 0.0052 \mu\text{m}^2$ for the effective area in the wire and $S_{loop} = 2.59 \mu\text{m}^2$ in the loop.

While recent interest in NRC has been motivated by a possibility of the *intrinsic* origin of the effect, NRC naturally arises in multiply-connected superconductors. In superconducting loops, the critical current is modulated by an external flux $\phi = BS_{loop}$ piercing the loop. In a loop with asymmetric arms, the current maximum is shifted from $B = 0$, and the sign of the shift depends on the direction of the current as shown in Fig. 3.3(a). A non-reciprocal component of the switching current ΔI is linear in B in the vicinity of $B = 0$, reaches extrema

at $\phi \approx \phi_0/4$, changes sign and oscillates with a period $\Delta\phi = \phi_0$. Thus, an asymmetric loop is the simplest “superconducting diode”. There is a clear similarity between ΔI measured in an asymmetric superconducting loop and in an Al/InAs nanowire as emphasized in Fig. 3.3(b), suggesting that non-monotonic NRC in our nanowires may be due to emerging current loops.

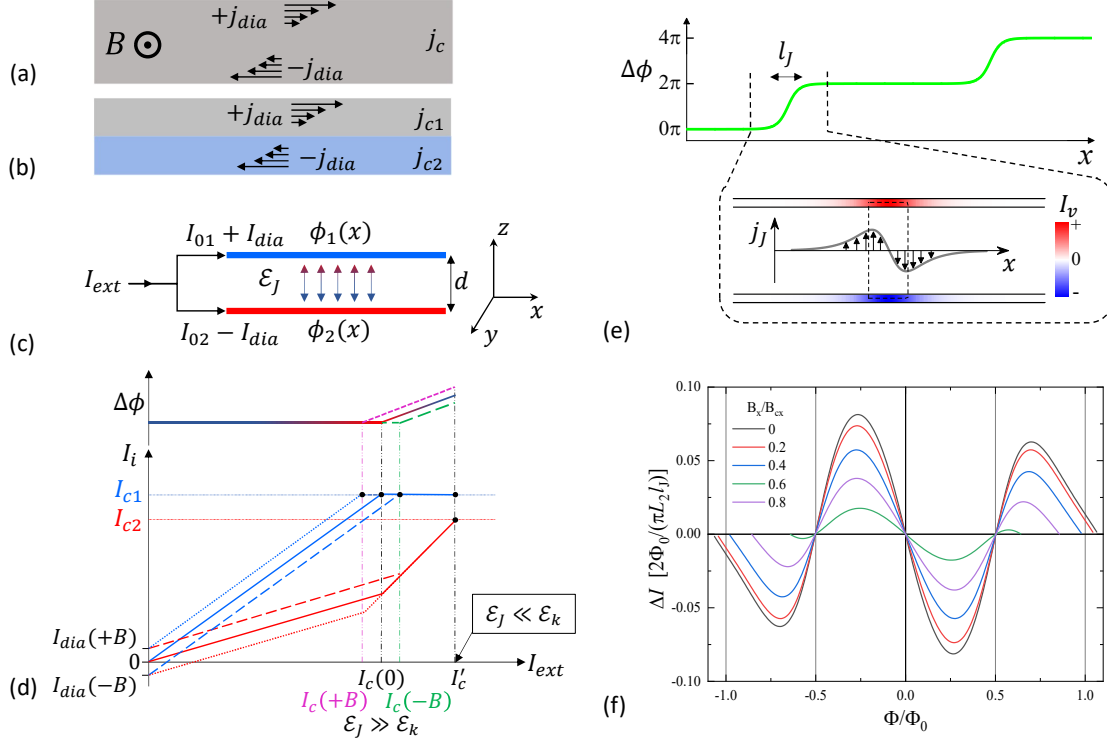


Figure 3.4. Non-reciprocity of the critical current in the presence of diamagnetic currents. Diamagnetic currents in (a) a uniform superconductor and (b) a heterostructure. (c) A two-layer heterostructure is modeled as two zero thickness wires separated by a distance d with coupling described by the Josephson energy \mathcal{E}_J . (d) Schematic of current distribution between the wires $I_i = I_{0i} - (-1)^i I_{dia}$, $i = 1, 2$, and the phase difference $\Delta\phi$ as a function of an external current $I_{ext} = I_1 + I_2$ for $B = 0$ (solid lines), $B > 0$ (dotted lines) and $B < 0$ (dashed lines). For weakly coupled wires $\mathcal{E}_J \ll \mathcal{E}_k$, the critical current is field-independent $I'_c = I_{c1} + I_{c2}$, see the text; the critical current is reduced and acquires a linear-in- B correction in a strong coupling regime $\mathcal{E}_J \gg \mathcal{E}_k$ due to the phase locking $\Delta\phi = 0$. (e) In the intermediate coupling regime $\mathcal{E}_J \sim \mathcal{E}_k$ Josephson vortices may form generating a 2π phase twist, in this case NRC becomes a non-monotonic function of B . (f) Calculated NRC ΔI is plotted as a function of flux $\Phi = S_v B_y$ for several B_x , Eq. (3.15).

External magnetic field generates circular diamagnetic currents in a superconductor, as shown schematically in Fig. 3.4(a,b), and these currents affect the critical current. In homogeneous superconductors the presence of diamagnetic currents will not result in the critical current non-reciprocity, but in a heterogeneous superconductor, in general, their presence will lead to NRC. Qualitatively, the origin of NRC can be understood from a simplified model of a superconductor heterostructure represented as two coupled zero thickness superconducting wires separated by a distance d , Fig. 3.4(c). The total energy of the two-wire system can be written as a sum of kinetic and Josephson energies,

$$E_{\text{tot}} = \int dx [\mathcal{E}_k - \mathcal{E}_J \cos(\Delta\phi)] , \quad (3.3)$$

where $\mathcal{E}_k = L_1 I_1^2 + L_2 I_2^2$, \mathcal{E}_J is the Josephson coupling, $\Delta\phi = \phi_1(x) - \phi_2(x)$ is the phase difference between superconducting condensates, and L_i are the kinetic inductances per unit length in wires labeled by an index $i = 1, 2$. Supercurrents in each wire $I_i = (2eL_i)^{-1}(\hbar\partial_x\phi_i - 2eA_x)$ should satisfy charge conservation constraint $I_1(x) + I_2(x) = I_{\text{ext}}$, where I_{ext} is the applied external current. Detailed solution for this model can be found in the Supplementary Materials, and we outline now the main results. For small external currents ($I_1 < I_{c1}$ and $I_2 < I_{c2}$, where I_{ci} are the critical currents in the wires) it is energetically favorable to keep the phase difference $\Delta\phi$ constant ($\Delta\phi = 0$ for $\mathcal{E}_J > 0$). Then, the currents can be expressed as $I_1 = I_{01} + I_{\text{dia}}$ and $I_2 = I_{02} - I_{\text{dia}}$, where $I_{01}, I_{02} \propto I_{\text{ext}}$ with $I_{01}/I_{02} = L_2/L_1 = \eta^{-1}$ and $I_{\text{dia}} = B_y d / (L_1 + L_2)$. Dependence of I_1 and I_2 on I_{ext} for $B_y > 0$, $B_y = 0$ and $B_y < 0$ is plotted schematically in Fig. 3.4(d). As I_{ext} increases and one of the currents (I_1 in our example) reaches the critical value I_{c1} , further external current increase requires an increase of $|\Delta\phi|$ because the excess current has to flow through the remaining superconducting wire with the current I_2 . In the case of weak interwire coupling, $\mathcal{E}_J \ll \mathcal{E}_k$, deviation of $\Delta\phi$ from zero does not lead to a significant energy penalty and the critical current of the whole system $I'_c = I_{c1} + I_{c2}$ does not depend on the magnetic field direction. In the opposite regime of strong coupling, $\mathcal{E}_J \gg \mathcal{E}_k$, the energy cost associated with the formation of Josephson currents (the last term in Eq. (3.3)) is prohibitively high and the whole system transitions to a normal state at $I_{\text{ext}} \approx (1 + \eta)(I_{c1} - I_{\text{dia}})$, resulting in $\Delta I = -2(\eta + 1)I_{\text{dia}}(B_y)$ (this

equation is correct for $\beta > \eta + (\eta + 1)I_{dia}/I_{c1}$, where $\beta = I_{c2}/I_{c1}$, NRC for other scenarios is listed in the Supplementary Materials). *Thus a superconducting diode effect is a generic property of coupled multilayer superconductors.*

As B_y and diamagnetic currents increase, the phase locking condition $\Delta\phi = 0$ along the length of the wires leads to a significant increase of \mathcal{E}_k . At a critical field $B_c = (3/\pi^2)\Phi_0/(l_J d)$ it becomes energetically favorable to reduce the overall energy by twisting the phase difference by 2π locally forming a Josephson vortex ($l_J \approx \Phi_0/(2\pi\sqrt{2\mathcal{E}_J L_2})$ and $\Phi_0 = h/2e$ is the flux quantum). Evolution of the phase difference $\Delta\phi(x) = 4 \arctan[\exp(x/l_J)]$, vortex-induced currents in the wires $I_v(x)$, and interwire Josephson current density $j_J(x)$ across a vortex are shown schematically in Fig. 3.4(e). The maximum of $I_v(x)$ at the center of the vortex determines the Josephson vortex contribution to NRC. In the absence of quantum fluctuations formation of a vortex is accompanied by an abrupt re-distribution of currents between the wires, which results in a sawtooth NRC dependence on magnetic field. Generation of multiple Josephson vortices does not modify NRC compared to a single vortex case unless the vortices significantly overlap so that the maximum of $I_v(x)$ exceeds its single-vortex value.

In Fig. 3.4(f) we plot $\Delta I(B_y)$ for several B_x using Eq. (3.15) in the Supplemental Material. A gradual change of ΔI near $\Phi_0/2$ is due to quantum fluctuations of the winding number due to strong coupling of the vortex to current-carrying wires. This smearing is similar to the gradual change of a critical current in a ring connected to superconducting leads (Fig. 3.3), as compared to an abrupt reversal of persistent currents at $\Phi_0/2$ in isolated rings [95]. The period of oscillations of ΔI corresponds to the flux threading an effective vortex area $S_v = (\pi^2/3)l_J d = l_v d$. The period $\Delta B_\perp = 400$ mT translates into the length $l_v \approx 500$ nm, where $\Delta\phi$ substantially deviates from zero. We estimate $l_v < \xi_{InAs} = \sqrt{\xi_{InAs}^0 l_{InAs}^m} \approx 750$ nm and expect proximity-induced superconductivity in InAs to be preserved in the presence of a vortex. Here we use $\xi_{InAs}^0 = \hbar v_F / \pi \Delta^* \approx 1.8 \mu\text{m}$, induced gap in InAs $\Delta^* \approx \Delta = 1.796 k_B T_c = 230 \mu\text{eV}$ (induced gap is close to the gap of Al in these heterostructures [42]), and the mean free path in uncapped InAs 2D gas $l_{InAs}^m \approx 300$ nm.

Finally, we use the two-wire model to estimate the temperature and in-plane field $B_{\parallel} \parallel \hat{x}$ dependences of NRC assuming that both parameters affect the Cooper pair density n_2 in

InAs. In the vicinity of $B_{\perp} = 0$ the amplitude of $\Delta I \propto L_2^{-1} \propto n_2$ and is expected to decrease with an increase of T or B_{\parallel} . The critical field $B_c \propto \sqrt{\mathcal{E}_J L_2}$ depends on $\mathcal{E}_J \propto n_2$, and the period of oscillations is expected to be T - and B_{\parallel} -independent, Fig. 3.4(d). Josephson coupling \mathcal{E}_J is exponentially sensitive to the thickness of the InGaAs spacer and we expect slight variations of the period ΔB_{\perp} between the samples. These qualitative estimates are consistent with experimental observations, see Figs. 3.6 and 3.7 in the Supplemental Material.

3.4 Dependence of non-reciprocity on various parameters

Comparison of symmetric and asymmetric contributions to the critical current.

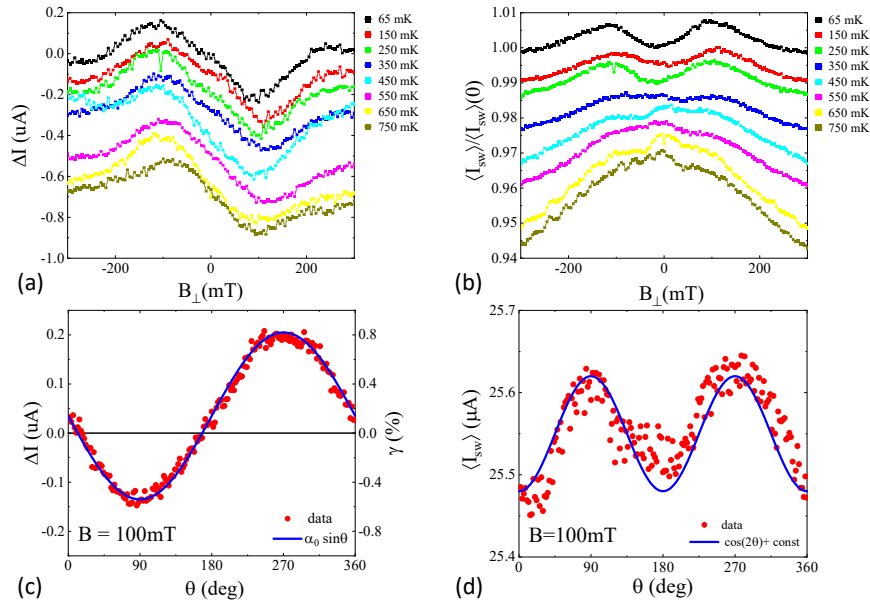


Figure 3.5. Field dependence of symmetric and asymmetric parts of the switching current. (a,b) Temperature dependence of ΔI and $\langle I_{sw} \rangle$ measured as a function of B_{\perp} ($\theta = 90$ deg). The curves are offset by $-0.1 \mu\text{A}$ (ΔI) and 0.01 ($\langle I_{sw} \rangle$). (c,d) Angle dependence is measured by rotating magnetic field of constant magnitude $B = 100$ mT at the base temperature.

The switching current can be decomposed into symmetric $\langle I_{sw} \rangle = (\langle I_{sw}^+ \rangle + \langle I_{sw}^- \rangle)/2$ and asymmetric $\Delta I = \langle I_{sw}^+ \rangle - \langle I_{sw}^- \rangle$ parts. Their dependence on magnetic field is plotted in Fig. 3.5. Both $\langle I_{sw} \rangle$ and ΔI are non-monotonic functions of B_{\perp} , however they have very

different T - and field-angle-dependencies. ΔI is almost unaffected by temperature up to $T \sim 0.6T_c$, while a dip around $B_{\perp} = 0$ in $\langle I_{sw} \rangle$ is developed at $T < 0.3T_c$. At constant $B = 100$ mT, the angular dependences are $\Delta I \propto \sin(\theta)$, but field-dependent correction to $\langle I_{sw} \rangle$ is $\propto \cos(2\theta)$. These differences in energy scales (T -dependence) and angular dependencies indicate that suppression of $\langle I_{sw} \rangle$ near $B = 0$ and asymmetric ΔI have different physical origins. Indeed, suppression of a critical current near $B = 0$ has been reported in previous works on single-layer nanowires and was attributed to the presence of quasiparticles and/or magnetic impurities [87], [96], which differ from geometrical effects responsible for $\Delta I(B)$ dependence.

Dependence of NRC on Temperature.

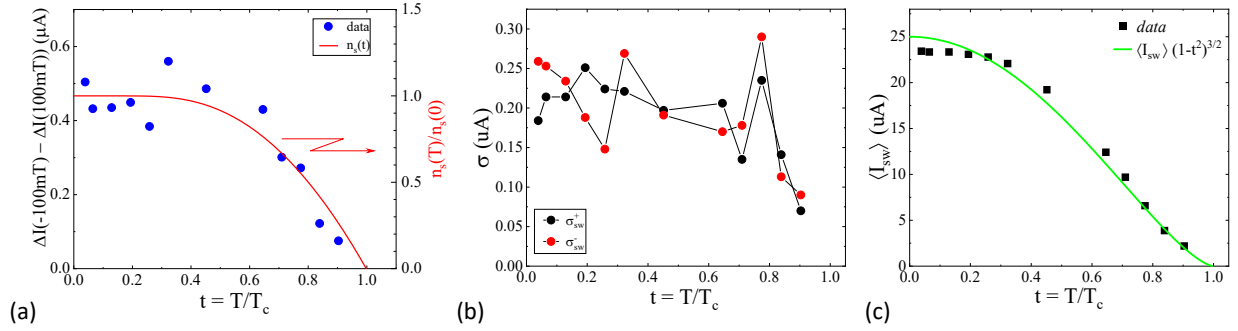


Figure 3.6. The effect of temperature on NRC. (a) The amplitude of NRC [$\Delta I(-100mT) - \Delta I(100mT)$], (b) the standard deviation of the switching currents at $B_{\perp} = 0$, and (c) the average switching current at $B_{\perp} = 0$ are plotted as a function of the reduced temperature. NRC amplitude follows the T -dependence of the Cooper pair density $n_s(T)$, consistent with Eq. (3.16). $\langle I_{sw} \rangle(T)$ follows the Bardeen relation[69].

Dependence of NRC on in-plane field.

Non-reciprocity of the switching current is linearly suppressed by an in-plane magnetic field $B_{\parallel} \parallel I$ and vanishes at ≈ 750 mT. Within the same range of B_{\parallel} the magnitude of the switching current remains almost constant (decreases $< 2.5\%$ at $B_{\parallel} = 750$ mT).

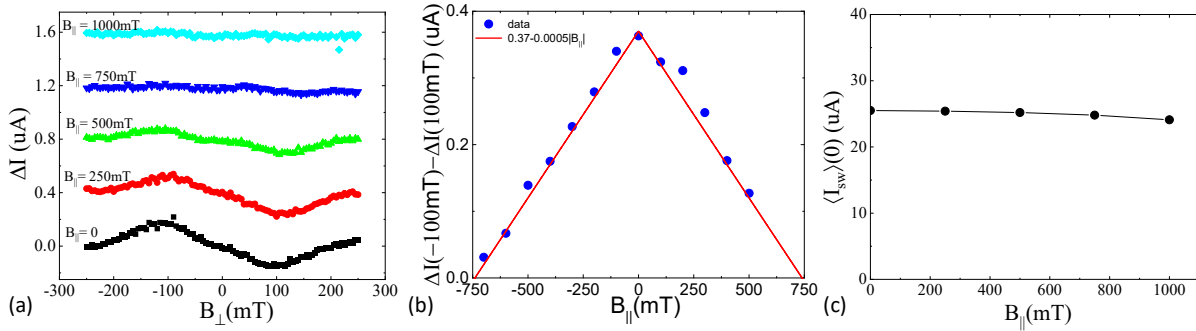


Figure 3.7. The effect of an in-plane current $B \parallel I$ on the non-reciprocal supercurrent. (a) Evolution of ΔI in the presence of B_{\parallel} . The plots are vertically shifted for clarity (b) The NRC amplitude falls approximately linearly with $|B_{\parallel}|$ (c) Dependence of average switching current $\langle I_{sw} \rangle$ at $B_{\perp} = 0$ on B_{\parallel} . All data is taken at the base temperature.

NRC in nanowires of various width

We have studied NRC in several nanowires of different width and length. Since all devices were fabricated from similar wafers, the Josephson coupling and, therefore, l_J are similar in all devices, and we expect the amplitude of ΔI and period ΔB to be similar. Indeed, that is the case for most devices, see Fig. 3.8a. One nanowire showed $\approx 2\times$ enhancement of ΔI and $\approx 2\times$ reduction of ΔB , which would be consistent with a local enhancement of l_J by a factor of 2.

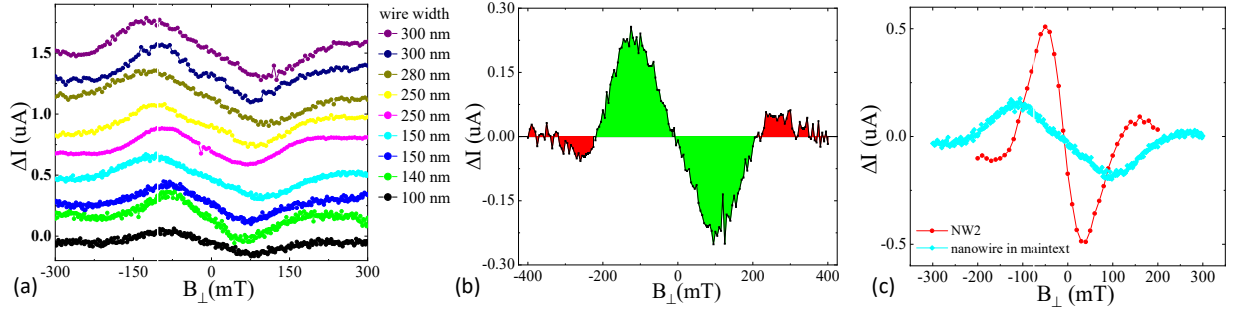


Figure 3.8. NRC in other devices. (a) NRC in nanowires of different width. The plots are shifted vertically for clarity. (b) Multiple sign reversal of ΔI in another nanowire. (c) one out of ~ 20 nanowires fabricated from similar wafers showed enhanced magnitude of ΔI and reduced ΔB .

Gate dependence of NRC and critical current.

On one of the samples we fabricated an electrostatic gate which covered the wire and a surrounding InAs 2D gas. In order to deplete electrons in InAs in the regions where it is not screened by Al, we apply a large negative gate voltage. We see no observable effect on the NRC when varying the gate voltage. InAs is expected to be fully depleted for applied gate voltage -1.5V. We measured NRC at different gate voltages varying from 0 to -4.5V and observed no variation of $\alpha = d\Delta I/dB_{\perp}$ near $B = 0$ or ΔB . Slight (up to 0.26%) increase of $\langle I_{sw} \rangle$ at large negative gate voltages is observed. Negative gate voltage also depletes carriers in Al (albeit their negligibly small fraction) and, thus, should result in the *decrease* of I_c , contrary to the observed increase. The observed increase of the switching current may result from the reduction of quantum fluctuations due to the reduction of InAs volume for Cooper pairs to enter and, as a consequence, increasing switching current to be closer to the value of the critical current.

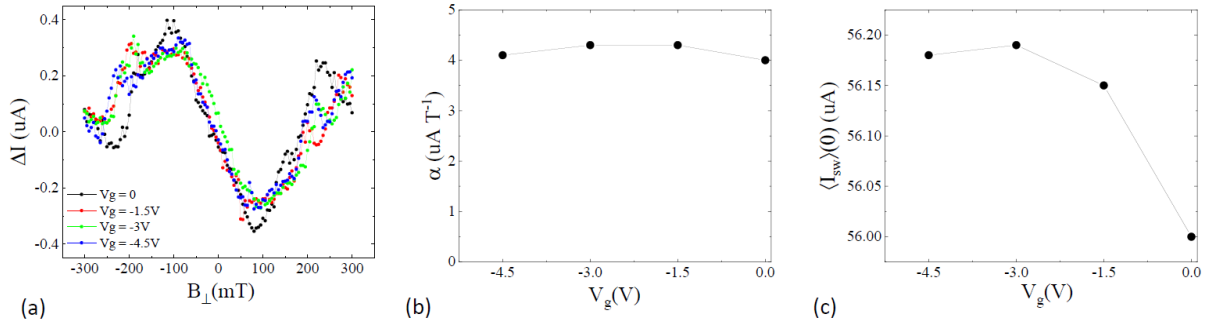


Figure 3.9. The effect of gate voltage on NRC. (a) NRC shows no observable difference on varying the gate voltage. (b) α shows very little variation with gate voltage. (c) When a negative gate voltage is applied the $\langle I_{sw} \rangle$ increases.

Absence of NRC in aluminum nanowire.

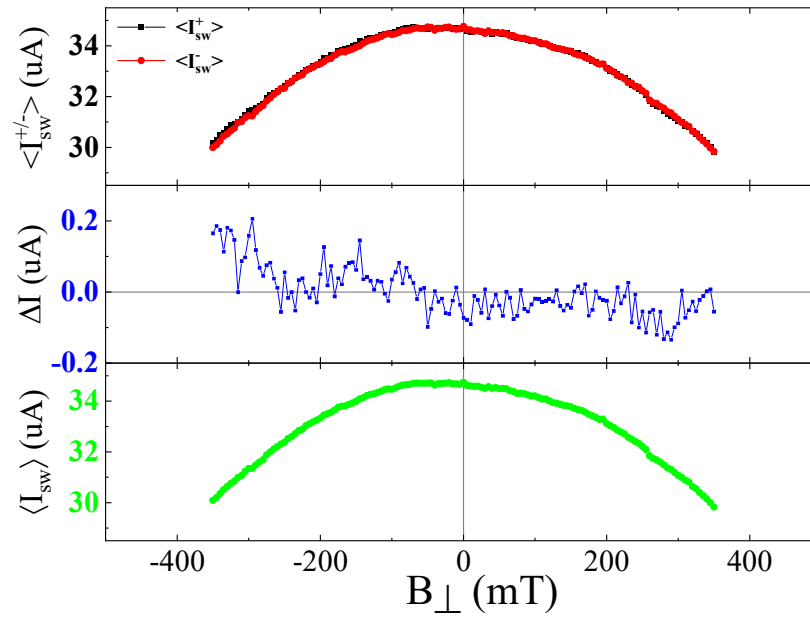


Figure 3.10. No NRC in a control device. A control 150 nm wide and $3 \mu\text{m}$ long nanowire is fabricated from a 20 nm thick Al film deposited on a semi-insulating Si wafer. This device shows no NRC.

In-plane magnetic field alignment

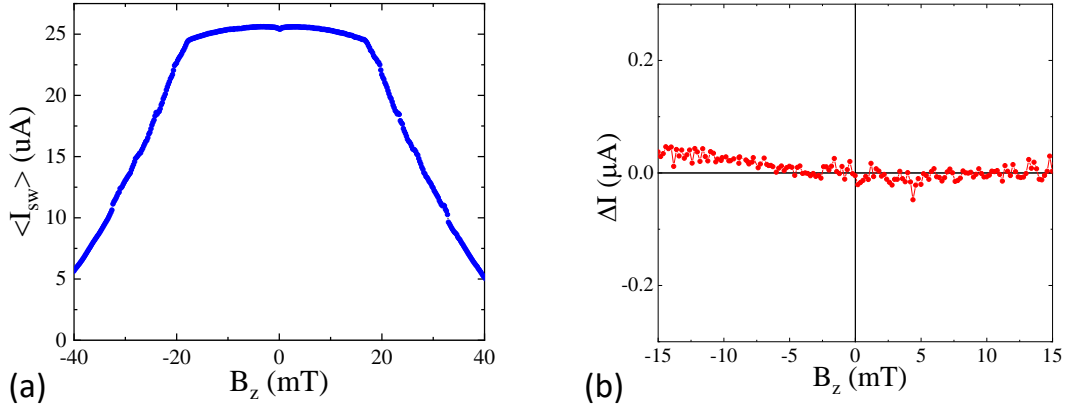


Figure 3.11. (a) Field dependence of $\langle I_{sw} \rangle$ shows a Meissner state up to $B_z \approx 18$ mT. (b) No NRC is observed in an out-of- plane magnetic field.

Magnetic fields are generated by a 3-axis vector magnet. The critical out-of-plane field for our wires is $B_{c2}^z \approx 60$ mT. A sharp reduction of $\langle I_{sw} \rangle$ at $B_z > 18$ mT is associated with an entrance of Abrikosov vortices. In order to align the in-plane field with the plane of the sample the following alignment procedure has been used. The in-plane field was ramped to $B'_{\parallel} \approx 800$ mT, beyond the field where NRC is observed. Next, B_z field is scanned ± 30 mT and a symmetry point B'_z is determined. In subsequent scans a linear correction $B_z = aB_{\parallel}$, where $a = B'_z/B'_{\parallel}$, is applied to keep B_{\parallel} aligned with the sample plane with a precision of < 0.1 degree.

3.5 Geometric effects and critical current non-reciprocity in coupled superconducting wires

In this section we derive the critical superconducting current in two Josephson-coupled superconducting wires (the “two-wire model”) in the presence of an external magnetic field. We show that at high enough magnetic field, it becomes energetically favorable to form a Josephson vortex (Fig. 3.12a), which in turn can lead to an oscillatory non-reciprocity of the

critical current (Fig. 3.4 of the main text). Furthermore, the oscillations will be damped due to one of the wires turning normal upon increasing the magnetic field.

Let us consider a pair of parallel superconducting wires 1 (Al wire) and 2 (proximitized InAs) along the x -direction with a magnetic field B_\perp in the y -direction, normal to the plane containing two wires. The corresponding vector potential is $A_x(z) = B_\perp z$ with the two wires separated by distance d being at positions $z = z_{1,2} = -(-1)^{1,2}d/2$, see Fig. 3.12a. We ignore here the screening of the magnetic field by the Josephson vortex; this effect would merely modify the Josephson length l_J (introduced below). We also approximate the wires as one-dimensional, given that their typical thickness is smaller than the penetration depth and the

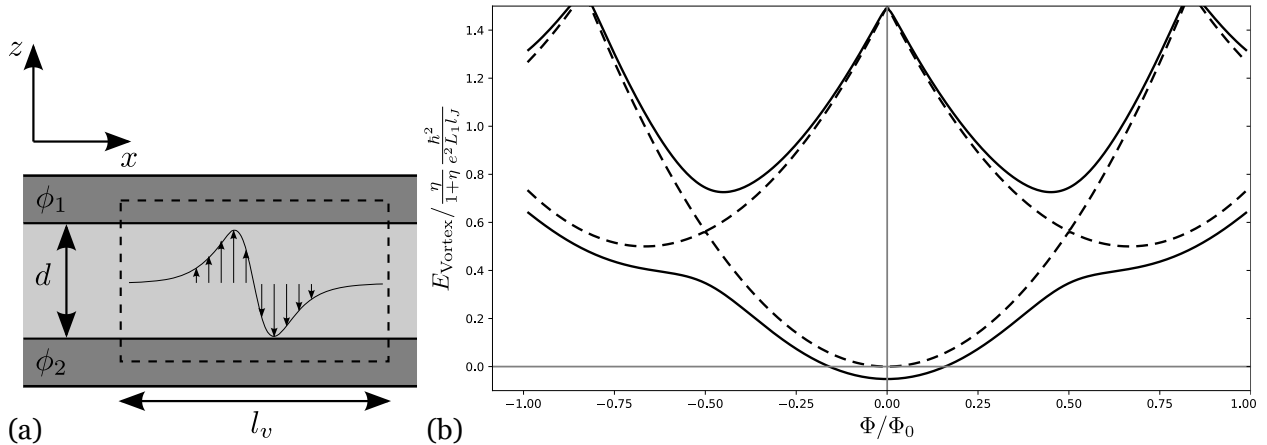


Figure 3.12. (a) Schematic picture of the model to explain non-reciprocity. The dark grey regions depict two superconducting wires labeled 1 and 2 (corresponding to Al and proximitized InAs wires, respectively) with the order parameter phases ϕ_1 , ϕ_2 . The region between the wires denotes the insulating barrier of thickness d . In most positions x , the phases are locked to $\phi_1 = \phi_2 \pmod{2\pi}$ due to a strong Josephson coupling. In the region of length l_v spanned by the Josephson vortex the phases are not equal and as a result the phase difference winds by an additional $2\pi n$ over the vortex. The vertical arrows denote the resulting Josephson currents flowing between the two wires in the vortex. (b) Total energy vs magnetic field in the two-wire model. The dashed curves show the spectrum obtained from Eq. (3.10). The three parabolas correspond to Josephson vortices/antivortices with $n = -1, 0, 1$. The solid curves show the energies when coherent vortex tunneling (strength $E_t = 0.4$ in units of $\frac{\eta}{1+\eta} \frac{\hbar^2}{e^2 L_1 l_J}$) is included, leading to avoided crossings of states with different n .

width is smaller than the size of the Peal vortex. This makes the supercurrent distribution approximately uniform within the wire. Denoting $\phi_{1,2}$ the phases of the superconducting order parameters, we have a supercurrent in wire i given by

$$I_i = \frac{1}{2eL_i} (\hbar\partial_x\phi_i - 2eA_x(x, z_i)) , \quad (3.4)$$

in terms of the kinetic inductances (per length) $L_i = m_i/(e^2S_i n_i)$ for wires $i = 1, 2$. Here S_i , m_i , and n_i denote the cross-sectional area, the effective mass, and the Cooper pair densities. For Al wire ($i = 1$) we will account for disorder by multiplying n_i by $\sqrt{l/\xi}$, where $l \approx 2\text{nm}$ is the mean free path and $\xi \approx 1\mu\text{m}$ is the coherence length [69]. Thus, we use $L_1 \rightarrow L_1\sqrt{\xi/l}$ in our final estimates.

The phases $\phi_{1,2}(x)$ can be found by minimizing the total energy

$$E_{\text{tot}} = \int dx \left[\frac{1}{2}L_1I_1^2 + \frac{1}{2}L_2I_2^2 - \mathcal{E}_J \cos(\phi_1 - \phi_2) \right] , \quad (3.5)$$

that includes kinetic energies of each wire and a Josephson energy density \mathcal{E}_J coupling the two wires. In the presence of an applied external supercurrent I_{ext} , there is a constraint $I_1(x) + I_2(x) = I_{\text{ext}}$ at every point x . The constrained energy minimization leads to the Sine-Gordon equation for $\varphi = \phi_1 - \phi_2$,

$$\frac{\partial^2\varphi}{\partial x^2} = l_J^{-2} \sin \varphi , \quad (3.6)$$

where $l_J = 1/\sqrt{8e^2\mathcal{E}_J(L_1 + L_2)/\hbar^2}$ is the Josephson length that determines the characteristic size of a Josephson vortex. We now solve Eq. (3.6) with the appropriate boundary conditions. We assume that the Josephson coupling in Eq. (3.5) is strong, such that $\phi_1 = \phi_2 \pmod{2\pi}$ for most x . If the two phases were locked for *all* x , i.e. $\varphi(x) = 0 \pmod{2\pi}$, we would find a non-reciprocal critical current $I_c(B_\perp)$ with the non-reciprocity $\Delta I = I_{c,+} - I_{c,-}$ that increases monotonically with B_\perp . Experimentally, a non-monotonic dependence is observed, see Fig. 3.1b.

The non-monotonic ΔI can be explained by a formation of a Josephson vortex, see Fig. 3.4. In the Josephson vortex, the phase difference φ increases by 2π approximately over the distance $2\pi l_J$; explicitly, $\varphi(x) = 4 \arctan e^{x/l_J}$ for a vortex at $x = 0$.

The Josephson vortex solution yields a current distribution

$$I_1(x) = \frac{1}{1 + \eta} I_{ext} + \delta I_n(x), \quad (3.7)$$

$$I_2(x) = \frac{\eta}{1 + \eta} I_{ext} - \delta I_n(x), \quad (3.8)$$

$$\delta I_n(x) = \frac{2\eta}{1 + \eta} \frac{1}{2eL_1} \frac{\hbar}{l_J} \left(n \operatorname{sech} \frac{x}{l_J} - \frac{3}{\pi} \frac{\Phi}{\Phi_0} \right), \quad (3.9)$$

where we introduced an integer index n , $n = \pm 1$ for the Josephson vortex/antivortex and $n = 0$ in the absence of the vortex. The vortex is centered at $x = 0$, which also turns out to be the position of the maximal circulating currents in the wires 1 and 2. We denote $\eta = L_1/L_2 = S_2 \frac{n_2}{m_2}/S_1 \frac{n_1}{m_1}$ and introduce the flux $\Phi/\Phi_0 = S_v B_\perp/(\pi\hbar/e)$ through the effective vortex area $S_v = (\pi^2/3)l_J d$.

The formation of the Josephson vortex becomes energetically favorable at a large enough magnetic field B_\perp . The energy cost is determined from Eq. (3.5) by the balance of the Josephson energy E_J lost and the kinetic energy gained in the creation of a vortex. Ignoring n -independent terms, we find (see Fig. 3.12b),

$$E_{\text{Vortex}}(n) = \frac{\eta}{1 + \eta} \frac{\hbar^2}{e^2 L_1 l_J} \left[\left(n - \frac{3}{2} \frac{\Phi}{\Phi_0} \right)^2 + \frac{1}{2} |n| \right] \quad (3.10)$$

where $n = 0, \pm 1$. This energy is analogous to the (inductive) energy of a superconducting ring with a phase winding $2\pi n$ [97] apart from the last term in Eq. (3.10) which is the cost in Josephson energy. In the absence of quantum fluctuations and at $T = 0$, one finds from Eq. (3.10) that the thermal average $\langle n \rangle = [\Phi/\Phi_0]$ is given by the nearest integer to Φ/Φ_0 , leading to a sawtooth-like dependence for ΔI versus B_\perp (see below). Fluctuations will smear out the sawtooth dependence. In analogy to a superconducting ring [97], we expect to find

a harmonic dependence on the flux on a linear background in the case of strong quantum or thermal fluctuations,

$$\langle n \rangle = \frac{\Phi}{\Phi_0} - \delta n \sin \frac{2\pi\Phi}{\Phi_0}, \quad (3.11)$$

where $\delta n \ll 1$ due to strong fluctuations.

Importantly, in the case of quantum fluctuations, δn is independent of the temperature, whereas for thermal fluctuations one has exponential dependence on $1/T$. As we discuss below, the harmonic dependence on the flux translates to a similar dependence in the non-reciprocal part ΔI of the critical current, in agreement with experimental data. The observed weak T -dependence in Fig. 3.5a indicates that quantum fluctuations exceed thermal fluctuations in the experiment.

The critical current through our two wire system with contacts, effectively forming a ring-like structure is determined by the condition that at large enough I_{ext} , one of the wires (arms of the ring) turns normal. (Experiment indicates that the switching happens in Al, i.e.,

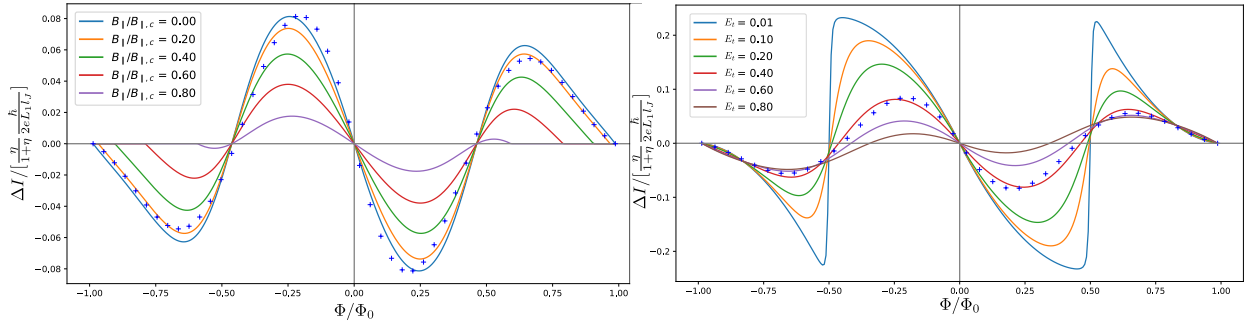


Figure 3.13. *Left:* The critical current non-reciprocity ΔI , Eq. (3.15), versus the flux $\Phi = B_{\perp} dl_v$ through the Josephson vortex. The crosses correspond to the approximation, Eq. (3.16). The applied field B_{\parallel} suppresses the proximity effect and therefore ΔI . In the figure $E_t = 0.4$ in units of $\frac{\eta}{1+\eta} \frac{\hbar^2}{e^2 L_1 l_J}$. *Right:* ΔI (at $B_{\parallel} = 0$) for different strengths E_t (in units of $\frac{\eta}{1+\eta} \frac{\hbar^2}{e^2 L_1 l_J}$) of coherent vortex tunneling that controls vortex number fluctuations; weak tunneling leads to a sawtooth-like ΔI .

wire 1, see below.) Assuming that $I_{ext} > 0$ and the wire 1 turns normal, the corresponding condition is $I_{ext} = I_{c,+}$, where

$$I_{c,\pm} = (1 + \eta)(\pm I_{1,c} - \delta I), \quad (3.12)$$

$I_{1,c}$ is the critical current of wire 1 and $\delta I = \langle \delta I_n(0) \rangle$ is the circulating current at its peak value at $x = 0$. Likewise, for $I_{ext} < 0$ we find $I_{ext} = I_{c,-}$. This yields

$$\Delta I = I_{c,+} + I_{c,-} \quad (3.13)$$

$$= -2\eta \frac{1}{L_1 e l_J} \left(\langle n \rangle - \frac{3}{\pi} \frac{\Phi}{\Phi_0} \right), \quad (3.14)$$

which determines the slope $\alpha = d\Delta I/dB_{\perp}$. We note that if the wire 2 is normal, then $n_2 = 0$, $\eta = 0$ and ΔI vanishes. The B_{\perp} -dependence of the critical current $I_{c,\pm}$ in such case would merely show a monotonic decrease (without non-reciprocity) corresponding to suppression of the superconducting gap in Al. Experiments show a few distinct oscillations in the asymmetric non-reciprocal part ΔI of the critical current, see Figs. 3.1c and 3.7. We attribute the experimentally observed vanishing amplitude of ΔI (loss of non-reciprocity) at fields higher than $B_{\perp} \approx 750\text{mT}$ to the destruction of proximity effect. We can model this by taking η in Eq. (3.14) to be magnetic field -dependent, detailed below.

Proximity effect is also destroyed by an in-plane field B_{\parallel} along the wire (along x) at roughly the same 750mT scale, see Fig. 3.6a. Since the wire 2 is proximitized in our model, we include a linear in the field suppression of the Cooper pair density n_2 at fields lower than those describing the superconducting gap suppression in the Al wire. This leads to $\eta = \eta_0(1 - |\mathbf{B}|/B_{\text{InAs},c})$ in Eq. 3.14. Here We take $B_{\text{InAs},c} \approx 750\text{mT}$ and denote $|\mathbf{B}| = \sqrt{B_{\perp}^2 + B_{\parallel}^2}$ assuming that the suppression of proximity is isotropic (in a magnetic field parallel to heterostructure layers).

The linear suppression is taken to match with experimental observations. In particular, a linear field-dependence is seen in Fig. 3.7b where the slope α is plotted as a function of B_{\parallel} . The measurement shows also that the switching current does not differ much from its $B_{\perp} = 0$ value (see Fig. 3.6c), indicating that the critical current is determined by Al wire,

as we assumed in Eq. (3.12). We thus obtain the following expression for the non-reciprocal contribution to the critical current, plotted in Fig. 3.4 and Fig. 3.13,

$$\Delta I(B_{\perp}, B_{\parallel}) = -2\eta_0 \frac{1}{L_1 e} \frac{\hbar}{l_J} \left(\langle n \rangle - \frac{3}{\pi} \frac{\Phi}{\Phi_0} \right) \left(1 - \frac{|\mathbf{B}|}{B_{\text{InAs},c}} \right) \quad (3.15)$$

$$\approx -2\eta_0 \frac{1}{L_1 e} \frac{\hbar}{l_J} \left(c \frac{\Phi}{\Phi_0} - \delta n \sin \frac{2\pi\Phi}{\Phi_0} \right) \left(1 - \frac{|\mathbf{B}|}{B_{\text{InAs},c}} \right), \quad (3.16)$$

where $c = (1 - \frac{3}{\pi}) \approx 0.05$ and we assumed strong quantum fluctuations of n , see discussion below Eq. (3.11). The approximate period is $B_{\perp} = \Phi_0(3/\pi^2)/(l_J d)$, experimentally observed to be approximately 400mT. This period indicates 500nm for the effective size of the vortex, given that $d = 10\text{nm}$.

From Eq. (3.16) we obtain a zero-field slope $d\Delta I/dB_{\perp} \approx -c_0 \eta_0 d/L_1$. Here $c_0 = (2\pi/3)(c - \delta n 2\pi)$ is an unknown numerical coefficient (since δn is unknown). However, the dimensionless quantity $\delta n_q \ll 1$ characterizes the amplitude of the persistent current in the loop (Fig. 3.4) and is suppressed due to quantum phase slips [97]. We can therefore take $c_0 \approx 2\pi c/3 \approx 0.1$. Using values $S_1 = 150\text{nm} \times 10\text{nm}$, $n_1 = 18 \cdot 10^{28} \text{m}^{-3}$ and $m_1 = 9.1 \cdot 10^{-31} \text{kg}$ (Al electron density and effective mass), we obtain $d/L_1 = \sqrt{l/\xi} S_1 \frac{e^2 n_1 d}{m_1} \approx 3.4 \text{mA/T}$. By comparing to the zero-field slope $d\Delta I/dB_{\perp} \approx 1.6 \mu\text{A/T}$ in Fig. 3.6b, we obtain $\eta_0 \approx 10^{-2}$. This is consistent with an estimate $\eta_0 \approx 10^{-2}$ based on the ratio of Al and InAs kinetic inductances. We note that non-reciprocal component is proportional to the Cooper pair density, $\Delta I \propto L_2^{-1} \propto n_2$, which is consistent with the temperature-dependence of both quantities plotted in Fig. 3.6a.

Different properties of wires 1 and 2, i.e., their asymmetry, is essential to get non-reciprocity in our model. If the wires were identical, the wire that switches to normal state first [in Eq. (3.12)] would change upon reversing the current direction. We note that non-reciprocity emerges even if there is no loop ($l_J \rightarrow 0$) due to Josephson vortex and no phase winding, $n = 0$ from Eq. (3.10), but there is nevertheless a circulating diamagnetic current I_{dia} , Eq. (3.9), leading to non-reciprocity, Eq. (3.15), due to the assumed Josephson coupling induced phase locking $\phi_1 = \phi_2$ between the wires.

3.6 Determining total critical current in a 2 wire model

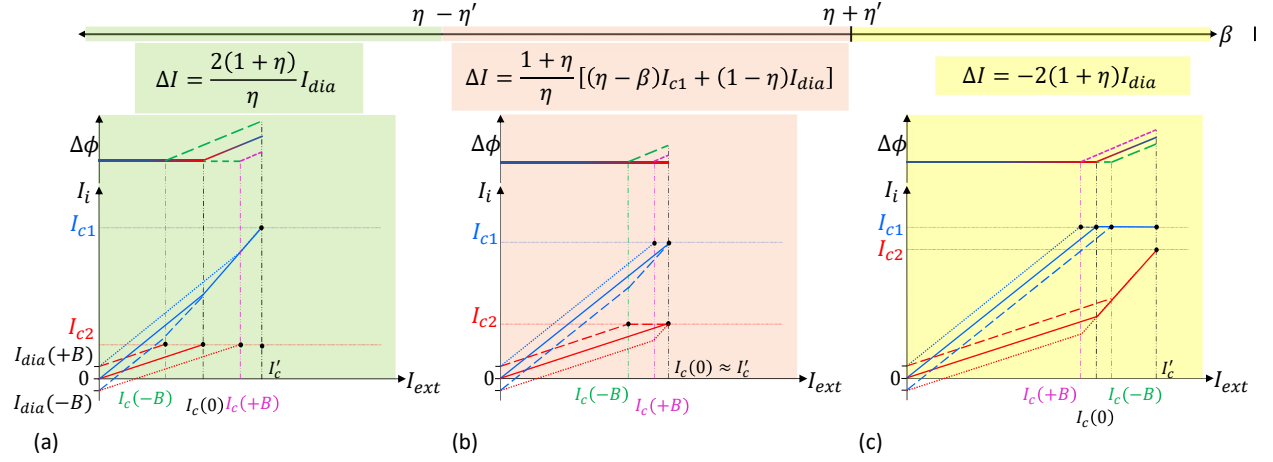


Figure 3.14. Schematic of current distribution between the wires $I_i = I_{0i} - (-1)^i I_{dia}$, $i = 1, 2$, and the phase difference $\Delta\phi$ as a function of an external current $I_{ext} = I_1 + I_2$ for (a) $\beta \leq \eta - \eta'$, (b) $\eta - \eta' < \beta < \eta + \eta'$ and (c) $\beta \geq \eta + \eta'$.

The total critical current in a two-wire model depends on the two dimensionless parameters: the ratio of kinetic inductances $\eta = L_{k1}/L_{k2}$ and the ratio of critical currents $\beta = I_{c2}/I_{c1}$. (The former also determines the current distribution in the absence of magnetic field, $\eta = I_2/I_1$.) In a magnetic field, the total critical current will also depend on the diamagnetic current, which enters via the dimensionless ratio $\eta' = (\eta + 1)I_{dia}/I_{c1}$. The expression of NRC depends on the magnitude of $\beta \gtrless \eta + \eta'$.

For $\beta \geq \eta + \eta'$, the wire 1 turns normal first for both directions of B_y , $I_c(B) = (1 + \eta)(I_{c1} - I_{dia})$ and

$$\Delta I = -2(1 + \eta)I_{dia} \quad (3.17)$$

For $\beta \leq \eta - \eta'$, the wire 2 turns normal first for both directions of B_y and

$$\Delta I = +2\frac{1 + \eta}{\eta}I_{dia} \quad (3.18)$$

Finally, for $\eta - \eta' \leq \beta \leq \eta + \eta'$, the wire 1 turns normal first for $B_y > 0$ and the wire 2 turns normal first for $B_y < 0$ resulting in

$$\Delta I = \frac{1 + \eta}{\eta} [(\eta - \beta)I_{c1} + (1 - \eta)I_{dia}] \quad (3.19)$$

The current distribution between the wires for these three cases is shown schematically in Fig. 3.14

We note that the slope $d\Delta I/dB_{\perp}$ differs by a large factor $1/\eta$ depending on which wire turns normal first. Our data is consistent with Al (wire 1) turning normal first (at that point the whole structure is turned normal).

4. DEVICE FABRICATION AND MEASUREMENT

4.1 Fabrication

Wafer Heterostructure

All the devices in my experiments were fabricated from one of the two wafers, wafer M and wafer J, grown in the laboratories of Prof. Michael Manfra and Prof Javad Shabani respectively. These two wafers are very similar in structure, as shown in fig 4.1, except for the thickness of the Al layer. The wafers differ in mobility and density of InAs, and critical fields of Al.

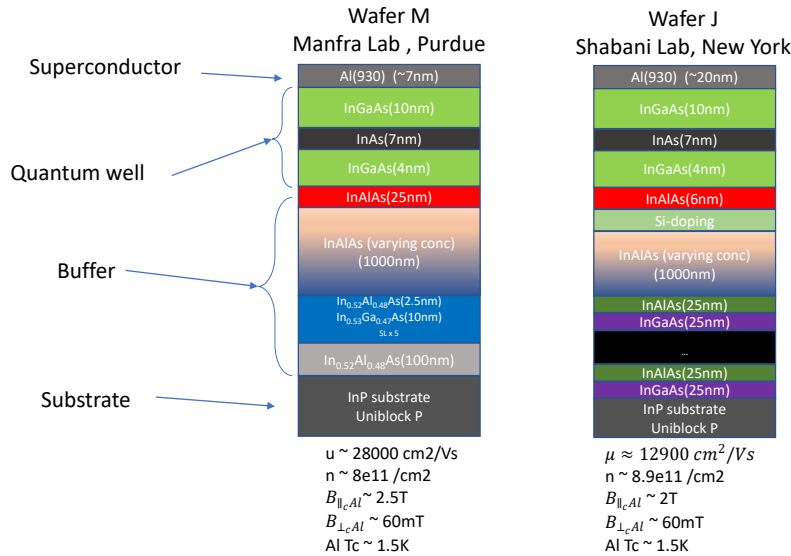


Figure 4.1. Heterostructure and properties of wafer M and wafer J.

Sample preparation

The fabrication starts with preparing small chips of 4x4 cm lateral dimensions. The pieces are cut from a 2" wafer. The heterostructure usually is grown in MBE chambers where the substrate is attached to the chuck using Indium. This indium is removed by mildly heating the pieces and wiping the Indium using a Qtip. The sample is then immersed in Acetone for

5-10 minutes followed by an Isopropyl Alcohol spray to remove acetone residue and then blow dried using a Nitrogen gun. The sample is then spin coated with e-beam photoresist typically PMMA A series followed by a baking on a hot-plate. Maintaining a low temperature of the sample is imperative to prevent Al diffusion, which can have a significant impact on the band structure. To this end, the pre-baking temperature is kept below 150 C for a duration of 3 minutes, followed by an extended oven bake at 90 C. This pre-bake temperature is lower than the conventional 180 C pre-bake used for PMMA. For the purpose of etching, thinner PMMA is preferred, especially for finer features. PMMA A2 when spin coated at 5000 rpm or more gives a thickness of 80-90 nm which is ideal for defining sub 100nm structures.

E-beam Patterning

The spin-coated sample is further subjected to electron beam lithography to define specific devices. Usually multiple devices are patterned in a single sample which is cut into individual at the end of all the fabrication. A Zeiss Evo 40 system is primarily used to define devices with feature sizes bigger than a few hundred nanometers. Finer features are defined using a Raith e-line system with a Field emitter. The samples exposed to electron beams are further processed by dipping into developers which dissolves the resist in the exposed area (or unexposed areas if negative resist). We usually use 2 developers : MIBK:IPA(1:3) and DI water:IPA (1:3). The latter developer is a fast developer compared to the former. A typical dose of 100uC/cm² is ideal for PMMA A2 if developed using MIBK:IPA(1:3). The ideal dose decreases to about 60 uC/cm² if DI water:IPA (1:3) is used. Higher doses are required as the thickness of the resist increases.

Aluminium etching

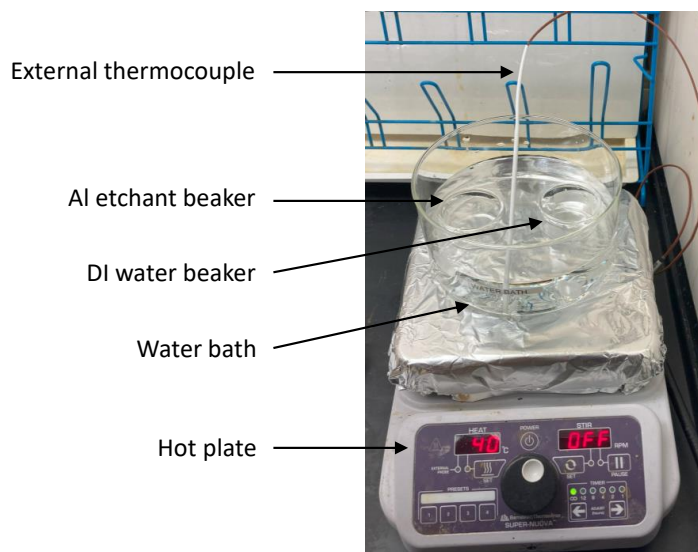


Figure 4.2. Caption

Aluminum is etched using Transene D. The etch rate is highly temperature-dependent. In cases where the thickness of Al is less than 9nm, the majority of the etching time is spent removing the 2nm oxide layer on the surface, while the rest is rapidly etched away. Hence, timing plays a critical role in this process, and even shaking can affect the etch rate. Placing the glass beaker directly on top of the heater may yield non-reproducible results, as the temperature of the etchant can deviate from that indicated by the heater thermocouple. To ensure temperature reproducibility, a water bath arrangement is utilized, with an external thermocouple immersed in the water to maintain its temperature at 40 ± 0.3 C. The beaker containing the etchant is also immersed in the water bath, placed on top of a plastic spacer to avoid direct heating from the bottom. After allowing approximately 30 minutes for the temperature to stabilize, the sample is immersed in the etchant for 9 ± 1 seconds, while being gently stirred. Failure to stir the sample could lead to a localized increase in temperature, resulting in an increased etch rate and reduced reproducibility. This etching recipe is applicable for samples with 5-7nm thick Al, while for thicknesses of 15-20 nm, the etching time is extended to approximately 13 seconds. At the end of the etching

duration, the sample is promptly dipped into a water beaker, which is kept immersed in the same water bath. While it may not be critical to maintain the temperature of water beaker, keeping it near facilitates the immediate transfer of the sample from the etchant to the water, arresting the etching process faster. Finally, the sample is cleaned using acetone/IPA.

Mesa etching

The process of mesa etching entails the initial removal of the aluminum (*Al*) top layer, followed by the etching of the indium arsenide (*InAs*) heterostructure. The etching solution used in this process is a mixture of phosphoric acid (H_3PO_4), hydrogen peroxide (H_2O_2), and deionized (DI) water (H_2O). The etch rate of the solution is heavily dependent on the specific ratio of the chemicals employed. In our experimentation, a ratio of 1:8:85 by volume was found to produce an etch rate of approximately 90 nanometers per minute. The addition of acetic acid to the etchant solution reduces the roughness of the etched surface, thereby enhancing the adhesion of metals deposited on top of the surface. Notably, Al is impervious to this etchant and can be employed as an etch mask if necessary. It was also observed that the PMMA C series exhibits weaker adhesion and etch resistance compared to the PMMA A series over areas where Al was previously removed. In fact, some of the samples were destroyed entirely when PMMA C4 was used as an etch mask. A long bake of 1 hour in an oven at 90 °C significantly enhances the etch resistance.

Gate fabrication

The process of gate fabrication involves the deposition of a gate dielectric across the sample surface using an atomic layer deposition (ALD) system (Cambridge Nanotech FIJI ALD). Typically, the growth of the dielectric is carried out at a temperature of 900°C, wherein atomic layers of the dielectric material are deposited using a cycle of precursor and water pulses at a rate of approximately 1 angstrom per cycle. The two types of dielectrics commonly used for this purpose are HfOx and AlOx, with HfOx possessing a higher dielectric constant than AlOx, albeit with a greater propensity for charge trap states. Trimethylaluminum and

Tetrakis(dimethylamino)hafnium are employed as the precursors for the growth of AlOx and HfOx, respectively.

For our devices, a 20nm HfOx film grown at 90°C is found to be optimal for achieving good electrical properties. WE observed that HfOx exhibits superior electrical stability and is less prone to breakdown compared to AlOx. The low-temperature growth process takes approximately 8 hours to complete.

After the dielectric is grown, gate electrodes are deposited. For very fine features a 10nm Ti is deposited as the gate electrode. For bigger features Ti/Au (5nm/120nm) is deposited.

Bond pads and wire-bonding

Usually for bond pads the pre-grown Aluminium is good enough although it is less than 10nm thick. But depositing a thick gold layer helps in improving adhesion. The processed samples are finally cut into individual devices of 2x 2 mm in size. These are glued on the chip carriers using GE varnish and then wire-bonded usually using Aluminium wires. The bond pads below the gate dielectric is contacted by using higher powers for wire-bonding and physically punching through the oxide. A power about 200W usually works well. For Gold bond pads Gold wires works much better than Aluminium wires at much lower powers of approximately 125W.

4.2 Measurement Techniques

4.2.1 Dilution refrigerator

The wirebonded samples are loaded to the probe which is then loaded to the dilution refrigerator Leiden CF50. The probe is loaded to the bellow and pumped for about 2 hours before loading inserting it into the fridge. It takes roughly 7 hours for the probe to go from room temperature to 4K. It takes another 2 hours once the mixture condensation is started to go to milliKelvin temperatures. Care is taken to keep all the contacts grounded during the entire process to ensure that the device does not feel any sudden electrical shocks which can damage the device, particularly the gates. The dielectric is prone to breakdowns

especially at higher temperatures. The dielectric resistance increases substantially at lower temperatures.

4.2.2 Transport and Fast critical current measurements

The resistance measurements are conducted employing conventional lock-in techniques. Specifically, an ac voltage of 1 volt is applied on resistance of 100MO in series with the device under test (DUT) resulting in an ac excitation current of 10nA. The voltage probes are either directly connected to the input amplifier of the lock-in instrument or, alternatively, amplified using an external pre-amplifier before being fed into the lock-in input. Usually a frequency between 10Hz and 100Hz is used depending on other instruments in use around and staying away from 60Hz harmonics. A spectrum analyzer is usually employed to find the optimal frequency and eliminating noise sources and ground loops.

For precise measurements of critical, a specialized setup employing a Digital-to-Analog Converter (DAC) was assembled. This setup utilized a DAC chip controlled by a programmable micro-controller module (Teensy). The DAC assembly was capable of generating output voltages within the range of $\pm 10V$. By incorporating a high resistance in series with the Device Under Test (DUT), this setup could effectively function as a current source.

The voltage probes across the DUT were connected to a preamplifier. The amplified signal was subsequently fed into the Analog-to-Digital Converter (ADC) input of the Teensy module. The current was incrementally increased at a constant rate starting from zero until the voltage surpassed a predetermined threshold. The precise value of the current at which this voltage jump occurred was recorded in the Teensy's memory. This ramping procedure was repeated a fixed number of times after which the recorded values were transferred to a computer for further analysis. The data was processed to generate a histogram and subsequently scrutinized to extract relevant statistical parameters. It should be noted that the switching currents observed during the measurements were contingent upon the specific parameters employed during the ramping process, particularly the ramp rate and the wait time between consecutive ramps.

A higher ramp rate could potentially prompt the DUT to transition to a normal state at an earlier stage. Similarly, a slower ramp rate could also induce this transition due to the heating effect caused by normal conductors carrying current until reaching the sample. Additionally, the wait time between ramps needed to be sufficiently long to mitigate the heating effect arising from the DUT in its resistive state. Optimal parameter values were determined prior to commencing the actual measurements in order to ensure reliable and accurate results.

4.2.3 Optimizing Noise Filtering for critical current measurements

The performance of superconducting devices is significantly impacted by electrical and thermal noises originating from their surroundings. Various factors such as thermal and RF radiations, noise induced by current-carrying wires, the presence of metal frames in refrigeration systems, and residual magnetic fields and flux trapping affect the behavior of superconductors. Mitigating these issues is crucial for achieving optimal device performance.

A reliable indicator of noise levels can be obtained by measuring the critical currents of a standardized test device featuring a thin nanowire fabricated from Al or Nb. A higher critical current corresponds to lower noise levels. To optimize the measurement setup, the test device was subjected to multiple cooling cycles using different configurations of wiring and filters in order to maximize the critical currents. This process was carried out using both the Leiden refrigerator and the Oxford Heliox He3 system. The results of these experiments are summarized in the table below:

4.2.4 Experimental artifacts in critical current statistics

Although the term critical current is used throughout this thesis, in reality the actual critical current is unattainable and the measured values are always smaller than the actual unattainable value. So a more accurate term would be switching current. The switching current is very sensitive to the experimental setup, noise, contacts including the connectors along the wiring. We observed that under certain experimental setups, randomly, the critical current distribution deviates from the actual distribution. But we noticed this disappears

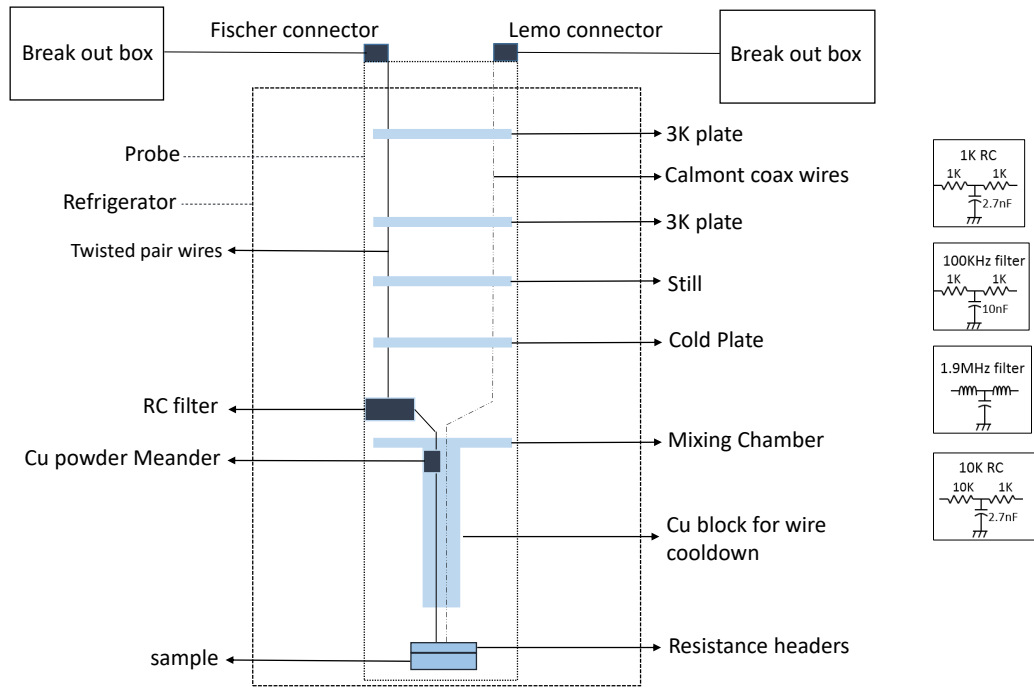


Figure 4.3. Arrangement of filters on the dilution refrigerator

when the bnc cables were disconnected and connected properly. Critical current statistics are prone to such artifacts and need to be separated from real effects.

Moreover the statistics also depends heavily on the current ramp parameters especially the ramp rate and wait time between ramps. The wait time between ramps ensures that the device cools down to the lowest temperature after the short joule heating when the device turns normal.

Configuration		Critical current
Wires	Filter	
Coax	No filters	0.6uA
Coax	100KHz RC	22uA
Coax	1.9MHz LC)	13uA
Coax	100KHz RC +1.9MHz LC	22uA
Twisted pair	Cu Meander + 100KHz RC/1.9MHz LC	2uA
Twisted pair	Cu Meander + 1K RC @ mixing chamber	15uA
Twisted pair	Cu Meander +10K RC @ mixing chamber	12uA
Twisted pair	Cu Meander+ 10K RC(grounded to fridge) @ mixing chamber	0
Twisted pair	Cu Meander+1K RC @ mixing chamber +10KO resistance header	16uA
Twisted pair	(NO meander) 10K RC @ mixing chamber	0
<i>Oxford Kelvinox</i>	10KO resistance header	23

Figure 4.4. Effect of different wirings and filters on the critical current in the dilution refrigerator

	Header	Wires	Copper shield	Filter	Critical current
Leiden Dry 50mK	No header	Calmont coax	YES	1.9 MHz filter @RT	35
He3 250mK	10KO header	Twisted pair	NO	No filter	16
He3 250mK	10KO header	Twisted pair	NO	1.9 MHz LC @ RT	11
He3 250mK	10KO header	Twisted pair	NO	100KHz RC @ RT	17
He3 250mK	No header	Twisted pair	NO	No filter	0
He3 250mK	No header	Twisted pair	YES	1.9 MHz LC / 100KHz RC	6
He3 250mK	No header	1 Twisted pair + 1 SS coax ending in SMA at top	NO	1.9 MHz LC / 100KHz RC	4
He3 250mK	No header	2 coax + ending in SMA at top	NO	No filter	5
He3 250mK	No header	2 coax ending in SMA at top	NO	1.9 MHz LC	27
He3 250mK	No header	2 coax ending in SMA at top	NO	100KHz RC	32
He3 250mK	No header	Twisted pair	NO	24 x 100KHz RC filter on probe top at RT (black box)	30

Figure 4.5. Effect of different wirings and filters on the critical current in the He3 refrigerator

5. SUMMARY AND PERSPECTIVES

This thesis embarked on a quest to explore topological superconductivity in an Al/InAs heterostructure. The initial objective was to shift the topological boundary away from the ends of one-dimensional systems by utilizing curved Josephson junctions, nanowires, and rings, while modulating the magnetic field to vary the superconducting gap.

However, the investigation of planar Josephson junctions proved unsuccessful due to a critically low magnetic field and the disruptive effects of flux focusing, which hindered the formation of a distinct boundary. As a result, attention turned towards studying the statistics of rings. Although some indications of a quantum transition were observed, the findings were inconclusive. Notably, an unexpected behavior in the form of a bimodal critical current distribution was discovered in a superconducting ring, prompting a more detailed exploration of nanowires.

This deeper investigation led to the identification of non-reciprocal critical currents in the Al/InAs heterostructure nanowires. The underlying physics responsible for this phenomenon was elucidated as the diamagnetic response and the formation of Josephson vortices within the vertical heterostructure, now recognized as the Superconducting Diode Effect.

While significant progress was made, further experiments are warranted to gain a more comprehensive understanding of the statistics of rings and curved Josephson junctions. Enhancing the edge uniformity and reducing the Josephson junction gap size could potentially facilitate these investigations. Moreover, the evolution of the Fraunhofer pattern emerged as a valuable tool for probing the search for topological superconductivity.

In conclusion, this thesis has shed light on the search for topological superconductivity in an Al/InAs heterostructure. Through the exploration of various system geometries, statistical analyses, and the observation of intriguing phenomena, significant progress has been achieved. The discoveries of the Superconducting Diode Effect and the importance of the Fraunhofer pattern evolution provide valuable insights for future studies and pave the way for further advancements in the field of topological superconductivity.

REFERENCES

- [1] M. Kohmoto, “Topological invariant and the quantization of the hall conductance,” *Annals of Physics*, vol. 160, no. 2, pp. 343–354, 1985, ISSN: 0003-4916. DOI: [https://doi.org/10.1016/0003-4916\(85\)90148-4](https://doi.org/10.1016/0003-4916(85)90148-4). [Online]. Available: <https://www.sciencedirect.com/science/article/pii/0003491685901484>.
- [2] A. Y. Kitaev, “Unpaired Majorana fermions in quantum wires,” *Physics-Uspekhi*, vol. 44, no. 10S, pp. 131–136, 2001, ISSN: 1468-4780. DOI: [10.1070/1063-7869/44/10s/s29](https://doi.org/10.1070/1063-7869/44/10s/s29). arXiv: [0010440](https://arxiv.org/abs/0010440) [[cond-mat](#)].
- [3] R. N and G. Dmitry, “Paired states of fermions in two dimensions with breaking of parity and time-reversal symmetries and the fractional quantum Hall effect,” *Physical Review B*, 2000. DOI: [10.1103/PhysRevB.61.10267](https://doi.org/10.1103/PhysRevB.61.10267).
- [4] A.Yu. Kitaev, “Fault-tolerant quantum computation by anyons,” *Annals of Physics*, vol. 303, pp. 2–30, 2002.
- [5] C. Nayak, S. H. Simon, A. Stern, M. Freedman, and S. Das Sarma, “Non-Abelian anyons and topological quantum computation,” *Reviews of Modern Physics*, vol. 80, no. 3, pp. 1083–1159, 2008, ISSN: 00346861. DOI: [10.1103/RevModPhys.80.1083](https://doi.org/10.1103/RevModPhys.80.1083). arXiv: [0707.1889](https://arxiv.org/abs/0707.1889).
- [6] S. D. Sarma, M. Freedman, and C. Nayak, “Majorana zero modes and topological quantum computation,” *npj Quantum Information*, vol. 1, no. 1, 2015, ISSN: 20566387. DOI: [10.1038/NPJQI.2015.1](https://doi.org/10.1038/NPJQI.2015.1). arXiv: [1501.02813](https://arxiv.org/abs/1501.02813). [Online]. Available: <http://dx.doi.org/10.1038/npjqi.2015.1>.
- [7] C. Nayak and F. Wilczek, “2N-Quasihole States Realize 2N-1-Dimensional Spinor Braiding Statistics in Paired Quantum Hall States,” *Nuclear Physics B*, vol. 479, no. 3, pp. 529–553, 1996, ISSN: 05503213. DOI: [10.1016/0550-3213\(96\)00430-0](https://doi.org/10.1016/0550-3213(96)00430-0). arXiv: [9605145](https://arxiv.org/abs/9605145) [[cond-mat](#)].
- [8] X.-G. Wen, “Topological Order and Edge Structure of $\nu=1/2$ Quantum Hall State,” *Physical Review Letters*, vol. 70, no. 3, 1993.
- [9] S. D. Sarma, M. Freedman, and C. Nayak, “Topologically protected qubits from a possible non-abelian fractional quantum hall state,” *Physical Review Letters*, vol. 94, no. 16, pp. 1–4, 2005, ISSN: 00319007. DOI: [10.1103/PhysRevLett.94.166802](https://doi.org/10.1103/PhysRevLett.94.166802). arXiv: [0412343](https://arxiv.org/abs/0412343) [[cond-mat](#)].
- [10] A. Stern and B. I. Halperin, “Proposed experiments to probe the non-abelian $\hat{\nu}=5/2$ quantum hall state,” *Physical Review Letters*, vol. 96, no. 1, pp. 1–4, 2006, ISSN: 10797114. DOI: [10.1103/PhysRevLett.96.016802](https://doi.org/10.1103/PhysRevLett.96.016802). arXiv: [0508447](https://arxiv.org/abs/0508447) [[cond-mat](#)].
- [11] D. A. Ivanov, “Non-Abelian statistics of half-quantum vortices in p-wave superconductors,” *Physical Review Letters*, vol. 86, no. 2, pp. 268–271, 2001, ISSN: 00319007. DOI: [10.1103/PhysRevLett.86.268](https://doi.org/10.1103/PhysRevLett.86.268). arXiv: [0005069](https://arxiv.org/abs/0005069) [[cond-mat](#)].

- [12] S. D. Sarma, C. Nayak, and S. Tewari, “Proposal to stabilize and detect half-quantum vortices in strontium ruthenate thin films: Non-Abelian braiding statistics of vortices in a $px + i py$ superconductor,” *Physical Review B - Condensed Matter and Materials Physics*, vol. 73, no. 22, pp. 3–6, 2006, ISSN: 10980121. DOI: [10.1103/PhysRevB.73.220502](https://doi.org/10.1103/PhysRevB.73.220502). arXiv: [0510553](https://arxiv.org/abs/0510553) [[cond-mat](https://arxiv.org/archive/cond)].
- [13] S. B. Chung, H. Bluhm, and E. A. Kim, “Stability of half-quantum vortices in $px+ipy$ superconductors,” *Physical Review Letters*, vol. 99, no. 19, pp. 1–4, 2007, ISSN: 00319007. DOI: [10.1103/PhysRevLett.99.197002](https://doi.org/10.1103/PhysRevLett.99.197002). arXiv: [0706.2660](https://arxiv.org/abs/0706.2660).
- [14] L. Fu and C. L. Kane, “Superconducting proximity effect and majorana fermions at the surface of a topological insulator,” *Physical Review Letters*, vol. 100, no. 9, pp. 1–4, 2008, ISSN: 00319007. DOI: [10.1103/PhysRevLett.100.096407](https://doi.org/10.1103/PhysRevLett.100.096407). arXiv: [0707.1692](https://arxiv.org/abs/0707.1692).
- [15] J. Linder, Y. Tanaka, T. Yokoyama, A. Sudbø, and N. Nagaosa, “Unconventional superconductivity on a topological insulator,” *Physical Review Letters*, vol. 104, no. 6, pp. 1–4, 2010, ISSN: 00319007. DOI: [10.1103/PhysRevLett.104.067001](https://doi.org/10.1103/PhysRevLett.104.067001). arXiv: [0911.3918](https://arxiv.org/abs/0911.3918).
- [16] A. Cook and M. Franz, “Majorana fermions in a topological-insulator nanowire proximity-coupled to an s-wave superconductor,” *Physical Review B - Condensed Matter and Materials Physics*, vol. 84, no. 20, pp. 1–4, 2011, ISSN: 10980121. DOI: [10.1103/PhysRevB.84.201105](https://doi.org/10.1103/PhysRevB.84.201105).
- [17] M. Sato and S. Fujimoto, “Topological phases of noncentrosymmetric superconductors: Edge states, Majorana fermions, and non-Abelian statistics,” *Physical Review B - Condensed Matter and Materials Physics*, vol. 79, no. 9, 2009, ISSN: 10980121. DOI: [10.1103/PhysRevB.79.094504](https://doi.org/10.1103/PhysRevB.79.094504). arXiv: [0811.3864](https://arxiv.org/abs/0811.3864).
- [18] I. Martin and A. F. Morpurgo, “Majorana fermions in superconducting helical magnets,” *Physical Review B - Condensed Matter and Materials Physics*, vol. 85, no. 14, pp. 1–6, 2012, ISSN: 10980121. DOI: [10.1103/PhysRevB.85.144505](https://doi.org/10.1103/PhysRevB.85.144505). arXiv: [1110.5637](https://arxiv.org/abs/1110.5637).
- [19] J. D. Sau and S. Tewari, “Topological superconducting state and Majorana fermions in carbon nanotubes,” *Physical Review B - Condensed Matter and Materials Physics*, vol. 88, no. 5, pp. 1–5, 2013, ISSN: 10980121. DOI: [10.1103/PhysRevB.88.054503](https://doi.org/10.1103/PhysRevB.88.054503).
- [20] A. M. Black-Schaffer and J. Linder, “Majorana fermions in spin-orbit-coupled ferromagnetic Josephson junctions,” *Physical Review B - Condensed Matter and Materials Physics*, vol. 84, no. 18, pp. 1–4, 2011, ISSN: 10980121. DOI: [10.1103/PhysRevB.84.180509](https://doi.org/10.1103/PhysRevB.84.180509). arXiv: [1106.1801](https://arxiv.org/abs/1106.1801).
- [21] M. Sato and Y. Ando, “Topological superconductors: A review,” *Reports on Progress in Physics*, vol. 80, no. 7, pp. 1–45, 2017, ISSN: 00344885. DOI: [10.1088/1361-6633/aa6ac7](https://doi.org/10.1088/1361-6633/aa6ac7). arXiv: [arXiv:1608.03395v3](https://arxiv.org/abs/1608.03395v3).
- [22] T. D. Stanescu and S. Tewari, “Majorana fermions in semiconductor nanowires: Fundamentals, modeling, and experiment,” *Journal of Physics Condensed Matter*, vol. 25, no. 23, 2013, ISSN: 09538984. DOI: [10.1088/0953-8984/25/23/233201](https://doi.org/10.1088/0953-8984/25/23/233201). arXiv: [1302.5433](https://arxiv.org/abs/1302.5433).

- [23] R. Aguado, “Majorana quasiparticles in condensed matter,” *Rivista del Nuovo Cimento*, vol. 40, no. 11, pp. 523–593, 2017, ISSN: 0393697X. DOI: [10.1393/ncr/i2017-10141-9](https://doi.org/10.1393/ncr/i2017-10141-9). arXiv: [1711.00011](https://arxiv.org/abs/1711.00011).
- [24] X. L. Qi and S. C. Zhang, “Topological insulators and superconductors,” *Reviews of Modern Physics*, vol. 83, no. 4, pp. 1–54, 2011, ISSN: 00346861. DOI: [10.1103/RevModPhys.83.1057](https://doi.org/10.1103/RevModPhys.83.1057). arXiv: [1008.2026](https://arxiv.org/abs/1008.2026).
- [25] J. Alicea, “New directions in the pursuit of Majorana fermions in solid state systems,” *Reports on Progress in Physics*, vol. 75, no. 7, 2012, ISSN: 00344885. DOI: [10.1088/0034-4885/75/7/076501](https://doi.org/10.1088/0034-4885/75/7/076501). arXiv: [1202.1293](https://arxiv.org/abs/1202.1293).
- [26] J. D. Sau, R. M. Lutchyn, S. Tewari, and S. Das Sarma, “Generic new platform for topological quantum computation using semiconductor heterostructures,” *Physical Review Letters*, vol. 104, no. 4, pp. 1–4, 2010, ISSN: 00319007. DOI: [10.1103/PhysRevLett.104.040502](https://doi.org/10.1103/PhysRevLett.104.040502). arXiv: [0907.2239](https://arxiv.org/abs/0907.2239).
- [27] J. Alicea, “Majorana fermions in a tunable semiconductor device,” *Physical Review B - Condensed Matter and Materials Physics*, vol. 81, no. 12, pp. 1–10, 2010, ISSN: 10980121. DOI: [10.1103/PhysRevB.81.125318](https://doi.org/10.1103/PhysRevB.81.125318). arXiv: [0912.2115](https://arxiv.org/abs/0912.2115).
- [28] Y. Oreg, G. Refael, and F. Von Oppen, “Helical liquids and Majorana bound states in quantum wires,” *Physical Review Letters*, vol. 105, no. 17, pp. 1–4, 2010, ISSN: 00319007. DOI: [10.1103/PhysRevLett.105.177002](https://doi.org/10.1103/PhysRevLett.105.177002). arXiv: [1003.1145](https://arxiv.org/abs/1003.1145).
- [29] R. M. Lutchyn, J. D. Sau, and S. Das Sarma, “Majorana fermions and a topological phase transition in semiconductor-superconductor heterostructures,” *Physical Review Letters*, vol. 105, no. 7, pp. 1–4, 2010, ISSN: 00319007. DOI: [10.1103/PhysRevLett.105.077001](https://doi.org/10.1103/PhysRevLett.105.077001). arXiv: [1002.4033](https://arxiv.org/abs/1002.4033).
- [30] Y. A. Bychkov and E. I. Rashba, “Oscillatory effects and the magnetic susceptibility of carriers in inversion layers,” *Journal of Physics C: Solid State Physics*, vol. 17, no. 33, pp. 6039–6045, 1984, ISSN: 00223719. DOI: [10.1088/0022-3719/17/33/015](https://doi.org/10.1088/0022-3719/17/33/015).
- [31] H. J. Kwon, K. Sengupta, and V. M. Yakovenko, “Fractional ac Josephson effect in p- and d-wave superconductors,” *European Physical Journal B*, vol. 37, no. 3, pp. 349–361, 2004, ISSN: 14346028. DOI: [10.1140/epjb/e2004-00066-4](https://doi.org/10.1140/epjb/e2004-00066-4). arXiv: [0210148](https://arxiv.org/abs/0210148) [[cond-mat](https://arxiv.org/abs/0210148)].
- [32] L. P. Rokhinson, X. Liu, and J. K. Furdyna, “The fractional a.c. Josephson effect in a semiconductor-superconductor nanowire as a signature of Majorana particles,” *Nature Physics*, vol. 8, no. 11, pp. 795–799, 2012, ISSN: 17452481. DOI: [10.1038/nphys2429](https://doi.org/10.1038/nphys2429). [Online]. Available: <http://dx.doi.org/10.1038/nphys2429>.
- [33] M. T. Deng, C. L. Yu, G. Y. Huang, M. Larsson, P. Caroff, and H. Q. Xu, “Anomalous zero-bias conductance peak in a Nb-InSb nanowire-Nb hybrid device,” *Nano Letters*, vol. 12, no. 12, pp. 6414–6419, 2012, ISSN: 15306984. DOI: [10.1021/nl303758w](https://doi.org/10.1021/nl303758w).

- [34] A. Das, Y. Ronen, Y. Most, Y. Oreg, M. Heiblum, and H. Shtrikman, “Zero-bias peaks and splitting in an Al-InAs nanowire topological superconductor as a signature of Majorana fermions,” *Nature Physics*, vol. 8, no. 12, pp. 887–895, 2012, ISSN: 17452481. DOI: [10.1038/nphys2479](https://doi.org/10.1038/nphys2479).
- [35] V. Mourik, K. Zuo, S. M. Frolov, S. R. Plissard, E. P. Bakkers, and L. P. Kouwenhoven, “Signatures of majorana fermions in hybrid superconductor-semiconductor nanowire devices,” *Science*, vol. 336, no. 6084, pp. 1003–1007, 2012, ISSN: 10959203. DOI: [10.1126/science.1222360](https://doi.org/10.1126/science.1222360).
- [36] D. I. Pikulin and Y. V. Nazarov, “Phenomenology and dynamics of a Majorana Josephson junction,” *Physical Review B - Condensed Matter and Materials Physics*, vol. 86, no. 14, pp. 1–5, 2012, ISSN: 10980121. DOI: [10.1103/PhysRevB.86.140504](https://doi.org/10.1103/PhysRevB.86.140504). arXiv: [1112.6368](https://arxiv.org/abs/1112.6368).
- [37] R. Hütten, A. Zazunov, B. Braunecker, A. L. Yeyati, and R. Egger, “Majorana single-charge transistor,” *Physical Review Letters*, vol. 109, no. 16, pp. 1–5, 2012, ISSN: 00319007. DOI: [10.1103/PhysRevLett.109.166403](https://doi.org/10.1103/PhysRevLett.109.166403). arXiv: [1206.3912](https://arxiv.org/abs/1206.3912).
- [38] L. Fu, “Electron Teleportation via Majorana Bound States in a Mesoscopic Superconductor,” vol. 056402, no. February, pp. 1–4, 2010. DOI: [10.1103/PhysRevLett.104.056402](https://doi.org/10.1103/PhysRevLett.104.056402).
- [39] J. Shabani, M. Kjaergaard, H. J. Suominen, *et al.*, “Two-dimensional epitaxial superconductor-semiconductor heterostructures: A platform for topological superconducting networks,” *Physical Review B*, vol. 93, no. 15, p. 155402, Apr. 2016. DOI: [10.1103/physrevb.93.155402](https://doi.org/10.1103/physrevb.93.155402). [Online]. Available: <https://doi.org/10.1103/PhysRevB.93.155402>.
- [40] H. Takayanagi and T. Kawakami, “Superconducting proximity effect in the native inversion layer on InAs,” *Physical Review Letters*, vol. 54, no. 22, pp. 2449–2452, 1985, ISSN: 00319007. DOI: [10.1103/PhysRevLett.54.2449](https://doi.org/10.1103/PhysRevLett.54.2449).
- [41] P. Krogstrup, N. L. Ziino, W. Chang, *et al.*, “Epitaxy of semiconductor-superconductor nanowires,” *Nature Materials*, vol. 14, no. 4, pp. 400–406, 2015, ISSN: 14764660. DOI: [10.1038/nmat4176](https://doi.org/10.1038/nmat4176).
- [42] F. Nichele, A. C. Drachmann, A. M. Whiticar, *et al.*, “Scaling of Majorana Zero-Bias Conductance Peaks,” *Physical Review Letters*, vol. 119, no. 13, pp. 1–5, 2017, ISSN: 10797114. DOI: [10.1103/PhysRevLett.119.136803](https://doi.org/10.1103/PhysRevLett.119.136803). eprint: [1706.07033](https://arxiv.org/abs/1706.07033). [Online]. Available: <https://doi.org/10.1103/PhysRevLett.119.136803>.
- [43] H. J. Suominen, M. Kjaergaard, A. R. Hamilton, *et al.*, “Zero-Energy Modes from Coalescing Andreev States in a Two-Dimensional Semiconductor-Superconductor Hybrid Platform,” *Physical Review Letters*, vol. 119, no. 17, pp. 1–5, 2017, ISSN: 10797114. DOI: [10.1103/PhysRevLett.119.176805](https://doi.org/10.1103/PhysRevLett.119.176805).
- [44] A. Fornieri, A. M. Whiticar, F. Setiawan, *et al.*, “Evidence of topological superconductivity in planar Josephson junctions,” *Nature*, 2019, ISSN: 14764687. DOI: [10.1038/s41586-019-1068-8](https://doi.org/10.1038/s41586-019-1068-8). arXiv: [1809.03037](https://arxiv.org/abs/1809.03037). [Online]. Available: <http://dx.doi.org/10.1038/s41586-019-1068-8>.

- [45] H. Ren, F. Pientka, S. Hart, *et al.*, “Topological superconductivity in a phase-controlled Josephson junction,” *Nature*, pp. 3–8, 2019, ISSN: 14764687. DOI: [10.1038/s41586-019-1148-9](https://doi.org/10.1038/s41586-019-1148-9). arXiv: [1809.03076](https://arxiv.org/abs/1809.03076). [Online]. Available: <http://dx.doi.org/10.1038/s41586-019-1148-9>.
- [46] M. C. Dartiailh, W. Mayer, J. Yuan, *et al.*, “Phase Signature of Topological Transition in Josephson Junctions,” *Physical Review Letters*, vol. 126, no. 3, pp. 1–6, 2021, ISSN: 10797114. DOI: [10.1103/PhysRevLett.126.036802](https://doi.org/10.1103/PhysRevLett.126.036802). arXiv: [1906.01179](https://arxiv.org/abs/1906.01179).
- [47] W. Mayer, M. C. Dartiailh, J. Yuan, K. S. Wickramasinghe, E. Rossi, and J. Shabani, “Gate controlled anomalous phase shift in Al/InAs Josephson junctions,” *Nature Communications*, vol. 11, no. 1, pp. 1–11, 2020, ISSN: 20411723. DOI: [10.1038/s41467-019-14094-1](https://doi.org/10.1038/s41467-019-14094-1). arXiv: [1905.12670](https://arxiv.org/abs/1905.12670).
- [48] A. Banerjee, O. Lesser, M. A. Rahman, *et al.*, “Signatures of a topological phase transition in a planar Josephson junction,” pp. 1–22, 2022. arXiv: [2201.03453](https://arxiv.org/abs/2201.03453). [Online]. Available: <http://arxiv.org/abs/2201.03453>.
- [49] F. Pientka, A. Keselman, E. Berg, A. Yacoby, A. Stern, and B. I. Halperin, “Topological superconductivity in a planar Josephson junction,” *Physical Review X*, vol. 7, no. 2, pp. 1–17, 2017, ISSN: 21603308. DOI: [10.1103/PhysRevX.7.021032](https://doi.org/10.1103/PhysRevX.7.021032).
- [50] M. Hell, M. Leijnse, and K. Flensberg, “Two-Dimensional Platform for Networks of Majorana Bound States,” *Physical Review Letters*, vol. 118, no. 10, pp. 1–6, 2017, ISSN: 10797114. DOI: [10.1103/PhysRevLett.118.107701](https://doi.org/10.1103/PhysRevLett.118.107701).
- [51] F. Dominguez, E. G. Novik, and P. Recher, “Fraunhofer pattern in the presence of Majorana zero modes,” pp. 44–48, 2022. arXiv: [2210.02065](https://arxiv.org/abs/2210.02065). [Online]. Available: <http://arxiv.org/abs/2210.02065>.
- [52] A. A. Golubov and D. Jena, “The current-phase relation in Josephson junctions,” vol. 76, no. April, pp. 411–469, 2004.
- [53] C. J. Palmstrøm, M. Kjaergaard, J. Danon, *et al.*, “Anomalous Fraunhofer interference in epitaxial superconductor-semiconductor Josephson junctions,” *Physical Review B*, vol. 95, no. 3, pp. 1–11, 2017, ISSN: 2469-9950. DOI: [10.1103/physrevb.95.035307](https://doi.org/10.1103/physrevb.95.035307).
- [54] C. Baumgartner, L. Fuchs, A. Costa, *et al.*, “Supercurrent rectification and magnetochiral effects in symmetric Josephson junctions,” *Nature Nanotechnology*, vol. 17, no. 1, pp. 39–44, 2022, ISSN: 17483395. DOI: [10.1038/s41565-021-01009-9](https://doi.org/10.1038/s41565-021-01009-9). [Online]. Available: <https://doi.org/10.1038/s41565-021-01009-9>.
- [55] A. A. Abrikosov, *Fundamentals of the Theory of Metals*.
- [56] M. Tinkham, *Introduction to Superconductivity*.
- [57] W. A. Little, “Decay of persistent currents in small superconductors,” *Physical Review*, vol. 156, no. 2, pp. 396–403, 1967, ISSN: 0031899X. DOI: [10.1103/PhysRev.156.396](https://doi.org/10.1103/PhysRev.156.396).
- [58] A. Bezryadin, “Quantum suppression of superconductivity in nanowires,” *Journal of Physics Condensed Matter*, vol. 20, no. 4, 2008, ISSN: 09538984. DOI: [10.1088/0953-8984/20/04/043202](https://doi.org/10.1088/0953-8984/20/04/043202).

- [59] J. M. Martinis, M. H. Devoret, and J. Clarke, “Tests for,” vol. 35, no. 10, pp. 4682–4698, 1987.
- [60] N. Giordano, “Evidence for Macroscopic Quantum Tunneling in One-Dimensional Superconductors,” *Physical Review Letters*, vol. 61, no. 18, pp. 2137–2140, Oct. 1988, ISSN: 0031-9007. DOI: [10.1103/PhysRevLett.61.2137](https://doi.org/10.1103/PhysRevLett.61.2137). [Online]. Available: <https://link.aps.org/doi/10.1103/PhysRevLett.61.2137>.
- [61] J. E. Mooij and Y. V. Nazarov, “Superconducting nanowires as quantum phase-slip junctions,” *Nature Physics*, vol. 2, no. 3, pp. 169–172, Mar. 2006, ISSN: 17452481. DOI: [10.1038/nphys234](https://doi.org/10.1038/nphys234).
- [62] T. Aref, A. Levchenko, V. Vakaryuk, and A. Bezryadin, “Quantitative analysis of quantum phase slips in superconducting Mo 76 Ge 24 nanowires revealed by switching-current statistics,” *Physical Review B*, vol. 024507, pp. 1–7, 2012. DOI: [10.1103/PhysRevB.86.024507](https://doi.org/10.1103/PhysRevB.86.024507).
- [63] A. Belkin, M. Belkin, V. Vakaryuk, S. Khlebnikov, and A. Bezryadin, “Formation of Quantum Phase Slip Pairs in Superconducting Nanowires,” vol. 021023, pp. 1–9, 2015. DOI: [10.1103/PhysRevX.5.021023](https://doi.org/10.1103/PhysRevX.5.021023).
- [64] C. N. Lau, N. Markovic, M. Bockrath, A. Bezryadin, and M. Tinkham, “Quantum Phase Slips in Superconducting Nanowires,” *Physical Review Letters*, vol. 87, no. 21, p. 217003, Nov. 2001, ISSN: 0031-9007. DOI: [10.1103/PhysRevLett.87.217003](https://doi.org/10.1103/PhysRevLett.87.217003). [Online]. Available: <https://link.aps.org/doi/10.1103/PhysRevLett.87.217003>.
- [65] S. Vijay, T. H. Hsieh, and L. Fu, “Majorana Fermion Surface Code for Universal Quantum Computation,” *Physical Review X*, vol. 5, no. 4, pp. 1–17, 2015, ISSN: 21603308. DOI: [10.1103/PhysRevX.5.041038](https://doi.org/10.1103/PhysRevX.5.041038). arXiv: [1504.01724](https://arxiv.org/abs/1504.01724).
- [66] A. Murphy and A. Bezryadin, “Asymmetric nanowire SQUID: Linear current-phase relation, stochastic switching, and symmetries,” *Physical Review B*, vol. 96, no. 9, pp. 1–11, 2017, ISSN: 24699969. DOI: [10.1103/PhysRevB.96.094507](https://doi.org/10.1103/PhysRevB.96.094507). arXiv: [1609.03877](https://arxiv.org/abs/1609.03877).
- [67] A. A. Burlakov, V. L. Gurtovoi, A. I. Il’in, A. V. Nikulov, and V. A. Tulin, “Superconducting quantum interference device without Josephson junctions,” *JETP Lett.*, vol. 99, no. 3, pp. 169–173, 2014, ISSN: 10906487. DOI: [10.1134/S0021364014030059](https://doi.org/10.1134/S0021364014030059). [Online]. Available: <https://doi.org/10.1134/S0021364014030059>.
- [68] A. Sundaresh, J. I. Vayrynen, Y. Lyanda-Geller, and L. P. Rokhinson, “Diamagnetic mechanism of critical current non-reciprocity in multilayered superconductors,” *Nature*, vol. 14, no. 1628, 2022, ISSN: 20411723. DOI: [10.1038/s41467-023-36786-5](https://doi.org/10.1038/s41467-023-36786-5). arXiv: [2207.03633](https://arxiv.org/abs/2207.03633). [Online]. Available: <https://doi.org/10.1038/s41467-023-36786-5>.
- [69] J. Bardeen, “Critical Fields and Currents in Superconductors,” *Rev. Mod. Phys.*, vol. 34, no. 4, pp. 667–681, Oct. 1962, ISSN: 0034-6861. DOI: [10.1103/RevModPhys.34.667](https://doi.org/10.1103/RevModPhys.34.667). [Online]. Available: <https://link.aps.org/doi/10.1103/RevModPhys.34.667>.

- [70] F. Ando, Y. Miyasaka, T. Li, *et al.*, “Observation of superconducting diode effect,” *Nature*, vol. 584, no. 7821, pp. 373–376, Aug. 2020, ISSN: 0028-0836. DOI: [10.1038/s41586-020-2590-4](https://doi.org/10.1038/s41586-020-2590-4). [Online]. Available: <http://www.nature.com/articles/s41586-020-2590-4>.
- [71] H. Narita, J. Ishizuka, R. Kawarazaki, *et al.*, “Field-free superconducting diode effect in noncentrosymmetric superconductor/ferromagnet multilayers,” *Nature Nanotechnology*, vol. 17, no. 8, pp. 823–828, Jun. 2022. DOI: [10.1038/s41565-022-01159-4](https://doi.org/10.1038/s41565-022-01159-4).
- [72] L. Bauriedl, C. Bäuml, L. Fuchs, *et al.*, “Supercurrent diode effect and magnetochiral anisotropy in few-layer NbSe₂,” *Nature Communications*, 2022. DOI: [10.1038/s41467-022-31954-5](https://doi.org/10.1038/s41467-022-31954-5). [Online]. Available: <https://doi.org/10.1038/s41467-022-31954-5>.
- [73] J.-x. Lin, P. Siriviboon, H. D. Scammell, *et al.*, “Zero-field superconducting diode effect in small-twist-angle trilayer graphene,” *Nature Physics*, 2022. DOI: [10.1038/s41567-022-01700-1](https://doi.org/10.1038/s41567-022-01700-1). [Online]. Available: <https://doi.org/10.1038/s41567-022-01700-1>.
- [74] Y.-Y. Lyu, J. Jiang, Y.-L. Wang, *et al.*, “Superconducting diode effect via conformal-mapped nanoholes,” *Nat. Commun.*, vol. 12, no. 1, p. 2703, Dec. 2021, ISSN: 2041-1723. DOI: [10.1038/s41467-021-23077-0](https://doi.org/10.1038/s41467-021-23077-0). [Online]. Available: <https://doi.org/10.1038/s41467-021-23077-0><http://www.nature.com/articles/s41467-021-23077-0>.
- [75] D. Suri, A. Kamra, T. N. Meier, *et al.*, “Non-reciprocity of vortex-limited critical current in conventional superconducting micro-bridges,” *Applied Physics Letters*, vol. 121, no. 10, 2022, ISSN: 00036951. DOI: [10.1063/5.0109753](https://doi.org/10.1063/5.0109753). [Online]. Available: <https://doi.org/10.1063/5.0109753>.
- [76] S. S. Ustavshikov, M. Y. Levichev, I. Y. Pashenkin, N. S. Gusev, S. A. Gusev, and D. Y. Vodolazov, “Diode Effect in a Superconducting Hybrid Cu/MoN Strip with a Lateral Cut,” *Journal of Experimental and Theoretical Physics*, vol. 135, no. 2, pp. 226–230, 2022, ISSN: 10906509. DOI: [10.1134/S1063776122080064](https://doi.org/10.1134/S1063776122080064). [Online]. Available: <https://doi.org/10.1134/S1063776122080064>.
- [77] Y. Hou, F. Nichele, H. Chi, *et al.*, “Ubiquitous Superconducting Diode Effect in Superconductor Thin Films,” 2022. arXiv: [2205.09276](https://arxiv.org/abs/2205.09276). [Online]. Available: <http://arxiv.org/abs/2205.09276>.
- [78] J. Diez-Merida, A. Diez-Carlon, S. Y. Yang, *et al.*, “Magnetic Josephson Junctions and Superconducting Diodes in Magic Angle Twisted Bilayer Graphene,” Oct. 2021. DOI: [10.48550/arxiv.2110.01067](https://doi.org/10.48550/arxiv.2110.01067). arXiv: [2110.01067](https://arxiv.org/abs/2110.01067). [Online]. Available: <https://arxiv.org/abs/2110.01067v1>.
- [79] B. Pal, A. Chakraborty, P. K. Sivakumar, *et al.*, “Josephson diode effect from cooper pair momentum in a topological semimetal,” *Nature Physics*, 2022. DOI: [10.1038/s41567-022-01699-5](https://doi.org/10.1038/s41567-022-01699-5). [Online]. Available: <https://doi.org/10.1038/s41567-022-01699-5>.

- [80] K. R. Jeon, J. K. Kim, J. Yoon, *et al.*, “Zero-field polarity-reversible Josephson supercurrent diodes enabled by a proximity-magnetized Pt barrier,” *Nature Materials*, vol. 21, no. September, 2022, ISSN: 14764660. DOI: [10.1038/s41563-022-01300-7](https://doi.org/10.1038/s41563-022-01300-7). [Online]. Available: <https://doi.org/10.1038/s41563-022-01300-7>.
- [81] M. Gupta, G. V. Graziano, M. Pendharkar, *et al.*, “Superconducting Diode Effect in a Three-terminal Josephson Device,” 2022. [Online]. Available: <http://arxiv.org/abs/2206.08471>.
- [82] T. Golod and V. M. Krasnov, “Demonstration of a superconducting diode-with-memory, operational at zero magnetic field with switchable nonreciprocity,” *Nature Communications*, vol. 13, no. 1, pp. 1–8, 2022, ISSN: 20411723. DOI: [10.1038/s41467-022-31256-w](https://doi.org/10.1038/s41467-022-31256-w). [Online]. Available: <https://doi.org/10.1038/s41467-022-31256-w>.
- [83] H. Wu, Y. Wang, Y. Xu, *et al.*, “The field-free Josephson diode in a van der Waals heterostructure,” *Nature*, vol. 604, no. 7907, pp. 653–656, 2022, ISSN: 14764687. DOI: [10.1038/s41586-022-04504-8](https://doi.org/10.1038/s41586-022-04504-8). [Online]. Available: <https://doi.org/10.1038/s41586-022-04504-8>.
- [84] J. Chiles, E. G. Arnault, C.-C. Chen, *et al.*, “Non-Reciprocal Supercurrents in a Field-Free Graphene Josephson Triode,” 2022. arXiv: [2210.02644](https://arxiv.org/abs/2210.02644). [Online]. Available: <http://arxiv.org/abs/2210.02644>.
- [85] B. Turini, S. Salimian, M. Carrega, *et al.*, “Josephson Diode Effect in High Mobility InSb Nanoflags,” *Nano Letters*, 2022. DOI: [10.1021/acs.nanolett.2c02899](https://doi.org/10.1021/acs.nanolett.2c02899). [Online]. Available: <https://doi.org/10.1021/acs.nanolett.2c02899>.
- [86] G. D. Simoni, F. Paolucci, P. Solinas, E. Strambini, and F. Giazotto, “Metallic supercurrent field-effect transistor,” *Nature Nanotechnology*, vol. 13, no. 9, pp. 802–805, Jul. 2018. DOI: [10.1038/s41565-018-0190-3](https://doi.org/10.1038/s41565-018-0190-3). [Online]. Available: <https://doi.org/10.1038/s41565-018-0190-3>.
- [87] I. Golokolenov, A. Guthrie, S. Kafanov, Y. Pashkin, and V. Tsepelin, “On the origin of the controversial electrostatic field effect in superconductors,” *Nature Communications*, vol. 12, p. 2747, May 2021. DOI: [10.1038/s41467-021-22998-0](https://doi.org/10.1038/s41467-021-22998-0). [Online]. Available: <https://doi.org/10.1038/s41467-021-22998-0>.
- [88] A. Daido, Y. Ikeda, and Y. Yanase, “Intrinsic Superconducting Diode Effect,” *Phys. Rev. Lett.*, vol. 128, no. 3, p. 037 001, Jan. 2022, ISSN: 0031-9007. DOI: [10.1103/PhysRevLett.128.037001](https://link.aps.org/doi/10.1103/PhysRevLett.128.037001). [Online]. Available: <https://link.aps.org/doi/10.1103/PhysRevLett.128.037001>.
- [89] S. Ili and F. S. Bergeret, “Theory of the supercurrent diode effect in Rashba superconductors with arbitrary disorder,” *Physical Review Letters*, vol. 128, no. 17, p. 177 001, Apr. 2022. DOI: [10.1103/PhysRevLett.128.177001](https://doi.org/10.1103/PhysRevLett.128.177001).
- [90] Y. Lyanda-Geller, J. I. Väyrynen, A. Sundaresh, and L. P. Rokhinson, to be published.
- [91] G. W. Winkler, A. E. Antipov, B. van Heck, *et al.*, “Unified numerical approach to topological semiconductor-superconductor heterostructures,” *Physical Review B*, vol. 99, no. 24, p. 245 408, Jun. 2019. DOI: [10.1103/PhysRevB.99.245408](https://doi.org/10.1103/PhysRevB.99.245408).

- [92] S. Giglberger, L. E. Golub, V. V. Bel'kov, *et al.*, “Rashba and dresselhaus spin splittings in semiconductor quantum wells measured by spin photocurrents,” *Physical Review B*, vol. 75, no. 3, p. 035327, Jan. 2007. DOI: [10.1103/PhysRevB.75.035327](https://doi.org/10.1103/PhysRevB.75.035327).
- [93] S. M. Farzaneh, M. Hatefipour, W. F. Schiela, *et al.*, “Magneto-anisotropic weak antilocalization in near-surface quantum wells,” 2022. DOI: [10.48550/arXiv.2208.06050](https://doi.org/10.48550/arXiv.2208.06050). eprint: [Search...](#)
- [94] C. Baumgartner, L. Fuchs, A. Costa, *et al.*, “Effect of rashba and dresselhaus spin-orbit coupling on supercurrent rectification and magnetochiral anisotropy of ballistic josephson junctions,” *Journal of Physics: Condensed Matter*, vol. 34, no. 15, p. 154005, Feb. 2022. DOI: [10.1088/1361-648X/ac4d5e](https://doi.org/10.1088/1361-648X/ac4d5e).
- [95] A. K. Geim, I. V. Grigorieva, S. V. Dubonos, *et al.*, “Phase transitions in individual sub-micrometre superconductors,” *Nature*, vol. 390, no. 6657, pp. 259–262, Nov. 1997, ISSN: 0028-0836. DOI: [10.1038/36797](https://doi.org/10.1038/36797). [Online]. Available: <http://www.nature.com/articles/36797>.
- [96] T.-C. Wei, D. Pekker, A. Rogachev, A. Bezryadin, and P. M. Goldbart, “Enhancing superconductivity: Magnetic impurities and their quenching by magnetic fields,” *Europhys. Lett.*, vol. 75, no. 6, pp. 943–949, 2006. DOI: [10.1209/epl/i2006-10218-2](https://doi.org/10.1209/epl/i2006-10218-2). eprint: [0510476](https://arxiv.org/abs/0510476). [Online]. Available: <https://iopscience.iop.org/article/10.1209/epl/i2006-10218-2>.
- [97] K. A. Matveev, A. I. Larkin, and L. I. Glazman, “Persistent current in superconducting nanorings,” *Phys. Rev. Lett.*, vol. 89, p. 096802, 9 Aug. 2002. DOI: [10.1103/PhysRevLett.89.096802](https://doi.org/10.1103/PhysRevLett.89.096802). [Online]. Available: <https://link.aps.org/doi/10.1103/PhysRevLett.89.096802>.